An Investigation of The Pressure Loss Characteristics for Highly Viscous Fluid Flow Through Narrow Slots

by

MD ASHKER RASHID

A thesis submitted in partial fulfillment of the requirements for the degree of

Master of Science

Department of Mechanical Engineering
University of Alberta

Abstract

An investigation was conducted to study the pressure loss characteristics of a highly viscous fluid flow across a sudden contraction. The objective of this work was to have a better understanding about the fluid flow phenomena across a narrow slot, which resembles the produced oil flow through the slotted liner during the SAGD operation. An extensive experimental work was undertaken along with the theoretical modelling for this research work. The pressure loss, the flow rate and the fluid viscosity were measured for different geometrical configuration of slots using an experimental setup. For a sudden contraction; slot width, aspect ratio, thickness to diameter ratio, diameter ratio and slot shape were varied over an appropriate range to encompass their effects on the pressure loss. The viscosity of the fluid was varied by varying the temperature within the range of $50\ °\mathrm{C} \leq T \leq 75\ °\mathrm{C}$. The Pressure loss was normalized using kinetic energy and characteristics were observed for the operating range of Reynolds number ($Re \leq 30$). The results show that for this low region of Reynolds number, the pressure loss decreases with increasing Reynolds number. The theoretical model also predicts the same trend of pressure loss. Within the operating range of viscosity ($40\ \mathrm{cP} < \mu < 300\ \mathrm{cP}$) the results show that the pressure loss decreases with decreasing viscosity. The Aspect ratio was varied within the range of 1 – 100 and general trend shows an increase in pressure loss with increasing aspect ratio. The Diameter ratio was another dominant factor for pressure loss across the sudden contraction. The results represent that pressure loss will increase with decreasing diameter ratio.

I dedicate this work to my parents.

Acknowledgements

First and foremost I would like to express my gratitude to my supervisors Dr. David S. Nobes and Dr. Brian Fleck. I would also like to thank RGL Reservoir management Inc. for donating the experimental setup to conduct this research work.

I am very much grateful to Dr. David S. Nobes for guiding me to the right path to conduct this research work. He helped me a lot learning about the experimental work and evaluating the results in a proper way. A discussion with him was the first step whenever I found an obstacle completing the experiment. His door was always open for me to discuss the progress of my work. I am also very glad to have Dr. Brian Fleck as my supervisor. He also helped me pointing out the key parameters for this work. Despite being very busy as a departmental chair, he also spent time with me as much as I needed. Whether the problem was related to my research work or not whenever I turned to him, he supported me with his help.

I am also grateful to my group mates Yishak Abdullah, Aidan Keaveny, Vineet Tailor for helping me with the experiments and preparing the experimental setup. I would also like to thank my wife Najratun Nayem Pinky for her support during the course of this work. I am also grateful to all my friends for making my life cheerful.

Contents

List of Tables

List of Figures

Nomenclature

Symbol	Description	Unit
a	Slot length	mm
A	Cross sectional area of the contraction	mm^2
AR_j	Aspect ratio	
b	Slot width	mm
C_c	Contraction coefficient	
C_d	Coefficient of discharge	
C_p	Velocity profile coefficient	
C_v	Viscosity coefficient	
d	Diameter of circular slot	mm
D	Flow channel/pipe diameter	mm
D_h	Hydraulic diameter	mm
Eu	Euler number	
f	Darcy friction factor	
g	Gravitational constant	$\mathrm{m/s^2}$
Δh	Total head loss	m
K	Hagenbach correction factor	
K'	Coquette correction factor	
k_l	Empirical factor	
K_l	Pressure loss coefficient	
l	Slot thickness	mm
L	Length of flow channel/pipe	m
L_1	Inlet length for streamlined slot	mm
L_2	Exit length for streamlined slot	mm
m	Consistency index of non-Newtonian fluid	
n	Power law index for non-Newtonian fluid	
P^*	Non-dimensional pressure loss	
ΔP	Pressure drop	Pa

Q	Flow rate	Kg/min
r	Radius of circular slot	
Re	Reynolds number	
t	Time	sec
T	Temperature	° C
TD	Thickness to diameter ratio	
u	Flow velocity across the contraction	m/s
U	Flow velocity across Flow channel/pipe	m/s

Greek letter	Description	unit
α	Error function parameter	
β	Diameter ratio	
γ	Strain rate	1/s
Δ	Difference	
ε	Pipe roughness factor	m
μ	Dynamic viscosity	Pa.s
ν	Kinematic viscosity	m^2/s
ρ	Density	Kg/m^3
τ	Shear stress	Pa
ϕ	Proportional factor	

Chapter 1: Introduction

1.1 Background

The effect of viscosity on pressure drop might be very prominent for highly viscous fluid flow though valves, pipes and filters. In most cases the viscosity effect is ignored because the system runs at low operating pressure. However, scenarios such as in-situ oil extraction processes, sub sea oil extraction processes and in the food processing industry/chemical industry, effects of highly viscous fluid flow at high pressure drop are significant. A steam assisted gravity drainage (SAGD) [1] system is one of the in-situ oil extraction processes where this problem plays a major role in oil production.

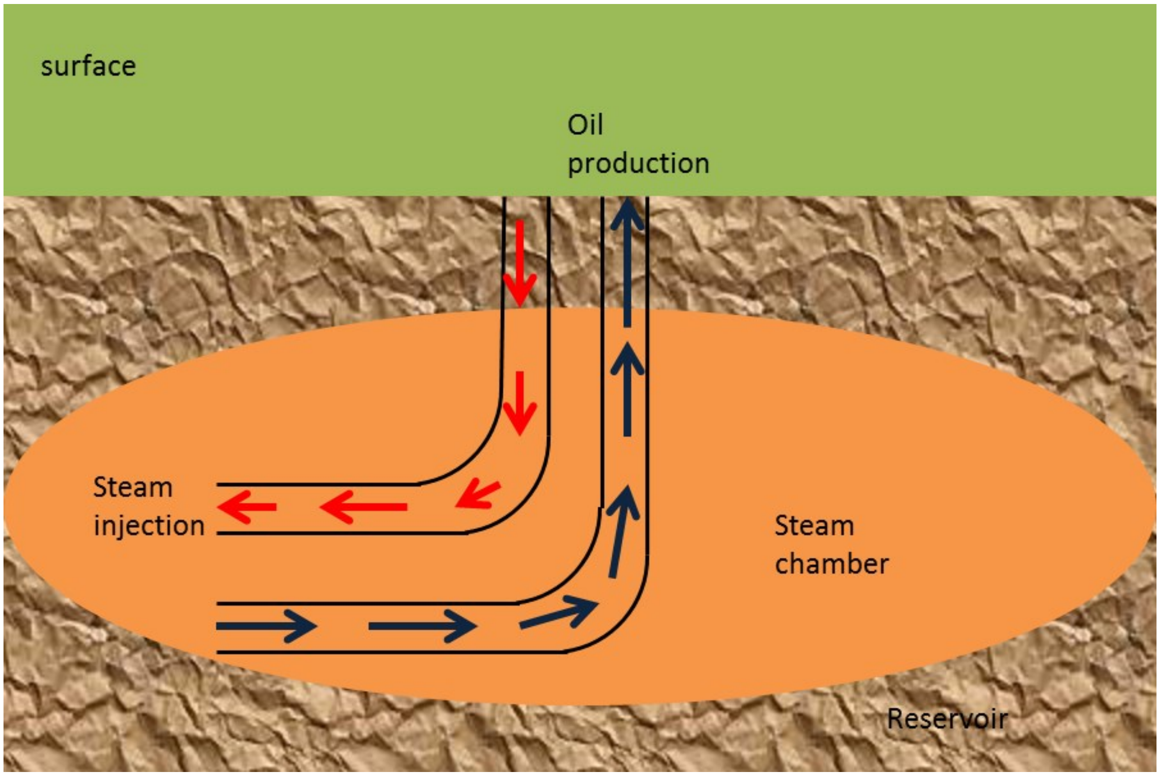

Figure 1.1 Graphical representation of SAGD process

SAGD is an enhanced oil recovery process for oil sands and heavy oil reservoirs. The method was first invented by Butler [1]. The basic principle is shown in Figure 1.1. A pair of horizontal wells is drilled into the deep oil reservoir with at least a 5 m gap in between the wells. High pressure steam is injected through the injection well to heat the reservoir thereby lowering the viscosity of bitumen. Due to lower viscosity, added water and gravitational force, the bitumen drains into the lower production well, from where it can be pumped out to the surface.

According to a recent (2013) report by Alberta Energy [2] about 80 % of the oil sands reserves (135 billion barrels) is located $>$ 70 m below the surface. Oil reservoirs below 200 m from the surface are suitable for SAGD operation [1]. In northern Alberta, bitumen has an API gravity around 8.5, with a strong dependency of viscosity and density on temperature [3]. It has the consistency of a solid at 0 °C and a fluid at $>$ 40 °C [3]. So this highly viscous fluid is difficult to flow in the reservoir condition [1]. The use of SAGD in oil extraction has advantages of reduced water consumption, less impact on the surface environment and less land reclamation efforts required compared to surface mining.

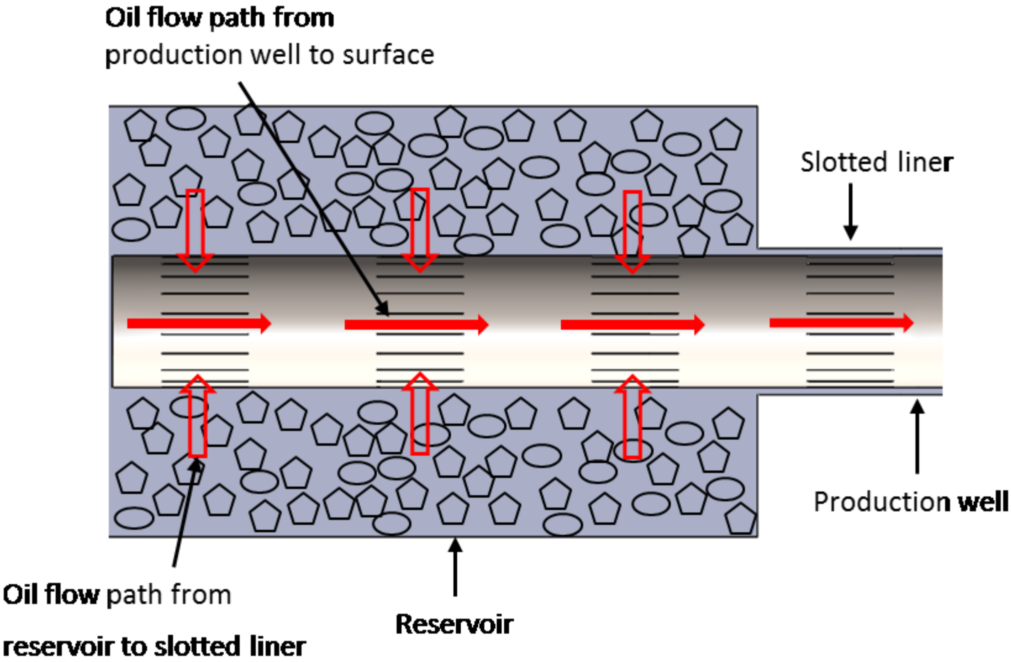

Figure 1.2 Schematic diagram of different flow domain of the oil in SAGD process

Figure 1.2 shows the flow paths of produced oil during SAGD process into the production well. Due to its low viscosity, produced oil drains into the production well. The flow through the porous structure of the reservoir is due to the combination of capillary force and gravitational force of the produced oil [4]. Then, from the reservoir the oil flows through a sand control device such as a slotted liner as shown in the Figure 1.2. In fact in SAGD operation different kinds of mechanical sand control methods are used [5]. Mainly these are [5]

- Gravel pack method
- Screens with or without gravel packing
- Slotted liner

Due to strong mechanical integrity [6] and low cost [5] slotted liner is the most common method. Slot geometry is defined by slot width and length. Generally the slot width is within the range of 0.30 mm - 0.46 mm (0.012 in - 0.018 in) and its length is in between 50 mm - 70 mm (2 in- 2.75 in) [7]. Choice of slot width is based on the reservoir sand particle size distribution in the well location, so that the slot prevent sand flow into the production well [7].

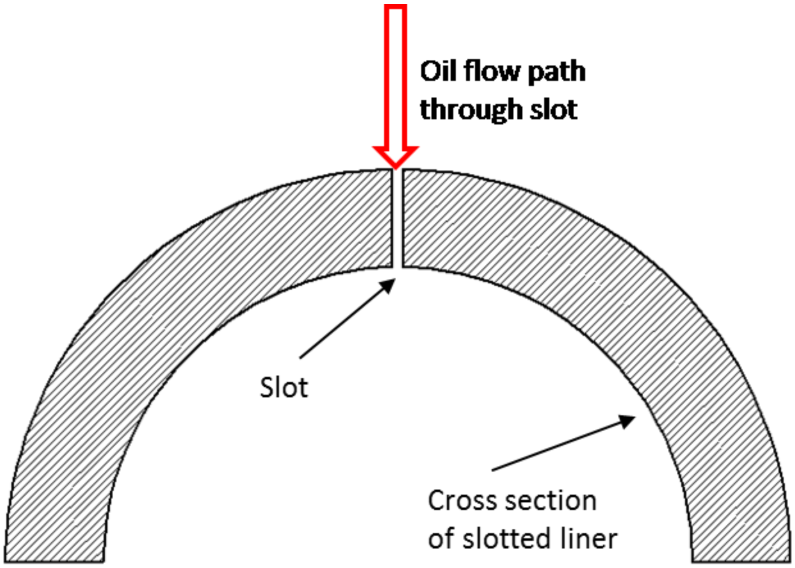

Figure 1.3 Expanded view of oil flow through slot

Figure 1.3 shows the flow domain to be investigated in this work. While working as a sand control device, this slot also creates a flow restriction for the oil. The associated pressure drop for highly viscous oil flow through these narrow slots affects both the production rate and the performance of the sand control system. The amount of artificial lift necessary for the recovery pump also depends on the pressure loss.

As the pressure loss - flow rate relationship across the slot is a dominant factor for SAGD operation in the slotted liner region, a better understanding is necessary to optimize the process. This work will investigate the highly viscous fluid flow through narrow slots and develop a pressure loss model for this type of fluid flow phenomena

1.2 Problem statement and geometry of the flow field

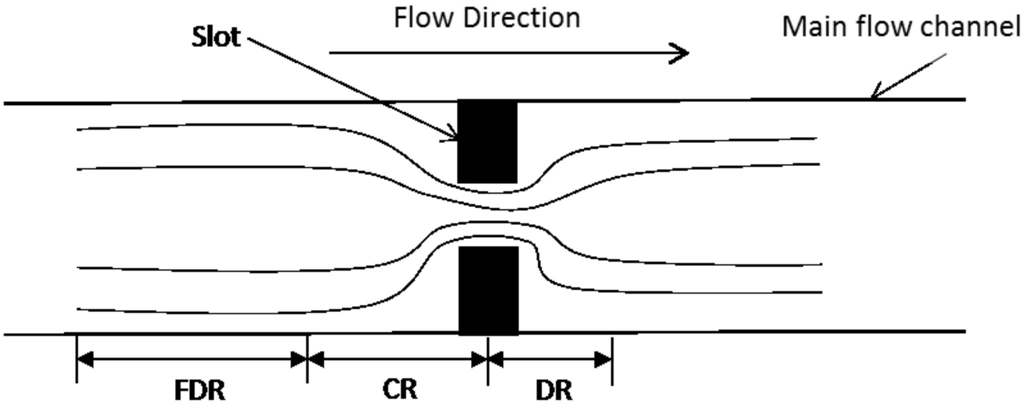

Figure 1.4 Schematic diagram of the simplified flow domain

A simplified flow model is derived to analyze the pressure loss characteristics for highly viscous fluid through a contraction region. Figure 1.4 shows the simplified model of the flow domain to be investigated. This figure shows that highly viscous fluid flows through the main flow channel and the slot acts as a sudden contraction. During oil production in the SAGD process, the fluid domain to be investigated is in the near-field of the slot. Certain scales of diameter ratio ($\beta = \frac{D_h}{D}$) are created due to the presence of porous media at the inlet of the slot. To capture the effect of that diameter ratio and effect of sudden contraction the simplified flow domain shown in Figure 1.4 is developed. This domain consists of three different sections. The first section is defined as fully developed region (FDR) where there is no change in the velocity field in the flow direction. From the FDR the flow experiences a contraction zone where the flow converges due to the change in geometry. From this point up to the middle plane of the slot is defined as the convergence region (CR). From the exit plane of the slot the flow starts to diverge due to the expansion of the geometry and this is defined as the divergence region (DR). Here, the slot will act as a flow obstruction to change the velocity and pressure field of the flow.

This change will depend on the geometry of the slot as well as fluid properties (density, ρ; dynamic viscosity, μ) and flow regime (laminar, turbulent). For this work pressure drop or pressure loss is defined as the pressure difference between the starting point of the convergence region and end point of the divergence region. The research scope will investigate the effect of fluid property (viscosity) and slot geometry (shape, aspect ratio, diameter ratio) on pressure loss for flows in the laminar region.

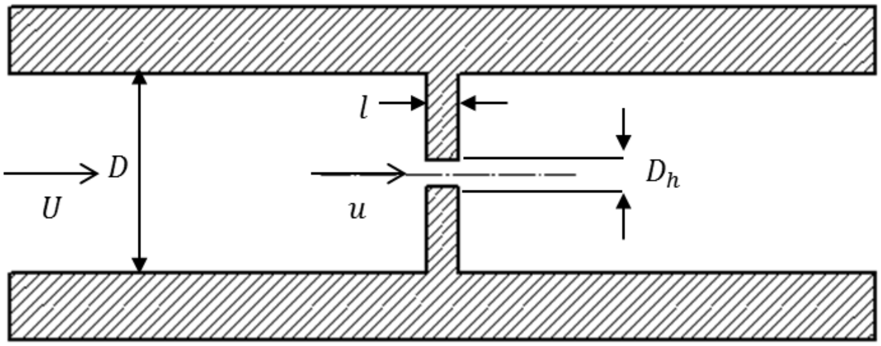

Figure 1.5 A schematic of the geometry of flow domain and contraction

A specific set of variables are used in this work to define different parameters. Figure 1.5 shows the geometry of the flow domain and the contraction where D is the diameter of the main flow channel, D_h is the hydraulic diameter of the contraction (rectangular slot), l is the thickness of the contraction (slot), U is the average centerline velocity for the main flow channel and u is average centerline velocity across the slot. For this geometry a Reynolds number (Re) can be defined as:

$$Re = \frac{\rho u D_h}{\mu} \tag{1.1}$$

where ρ is fluid's density, μ is fluid's dynamic viscosity. The diameter ratio (β) for characterizing the contraction can be defined as:

$$\beta = \frac{D_h}{D} \tag{1.2}$$

The aspect ratio of the slot is defined as:

$$AR_j = \frac{a}{b} \tag{1.3}$$

where a and b are the length and width of rectangular slot respectively. The thickness of the slot is normalized with hydraulic diameter and thickness to diameter ratio is defined as:

$$TD = \frac{l}{D_h} \tag{1.4}$$

Pressure drop (ΔP) across the slot is normalized as [8], [9]:

$$P^* = \frac{\Delta P}{\frac{1}{2}\rho u^2} \tag{1.5}$$

where P^* is the non-dimensional pressure loss across the slot. The Coefficient of discharge (C_d) is another important factor for flow across any contraction. It is defined as:

$$C_d = \frac{Q_{actual}}{Q_{theoretical}} \tag{1.6}$$

where Q_{actual} is the measured flow rate across the contraction and $Q_{theoretical}$ is the calculated flow rate across the contraction neglecting any losses as:

$$Q_{theoretical} = \frac{\pi D_h^2}{4}\sqrt{\frac{2\Delta P}{\rho(1-\beta^4)}} \tag{1.7}$$

Viscous dissipation is represented using a non-dimensional parameter, the Eckert number. It is defined as:

$$Ec = \frac{u^2}{c_p\,\Delta T}$$

where c_p is the constant pressure local specific heat and ΔT is the temperature change during fluid flow. The very low expected fluid velocity ranges in this problem would not give a significant result in the form of an Eckert number. That is why for further analysis in this problem, effect of viscous dissipation is neglected.

A review of the literature is needed focusing on these parameters to get an understanding of the defined problem. The review will also give a better understanding about the experimental variables and their range applicable for this work.

1.3 Literature review

1.3.1 General pressure loss analysis

The total pressure change between an upstream and downstream location in a fluid flow is defined as the pressure loss, ΔP. In pipe flow this occurs due to the dissipation of energy by the fluid [10]. Frictional resistance is caused by fluid viscosity. For axisymmetric incompressible Newtonian fluid flow in uniform diameter pipe this pressure loss can be expressed by the well-known Darcy-Weisbach [11] equation as :

$$f = \frac{L}{D}\frac{U^2}{2g} \qquad 1.8$$

where f is the Darcy frictional factor, L is the pipe length, D is the diameter of the pipe, U is the average centerline velocity of pipe and ΔP is pressure difference between the upstream and downstream locations. From this equation it is evident that pressure loss is a function of pipe geometry and average fluid velocity. This is a phenomenological equation where f is the Darcy frictional factor [12]. This factor depends on Reynolds number (Re), flow regime (laminar, turbulent) and pipe roughness. The value of this factor is measured from experimental data for different flow conditions. For laminar flow, this factor can be derived theoretically as [12]:

$$f = \frac{64}{Re} \qquad 1.9$$

As turbulent flow is very complex, it is very difficult to predict the friction factor through an analytical model. For turbulent flow a well-known empirical equation has been developed by Colebrook to estimate the friction factor [13]. This is expressed as:

$$\frac{1}{\sqrt{f}} = -2\,log_{10}\left(\frac{\varepsilon}{3.7D_h} + \frac{2.51}{Re\sqrt{f}}\right) \qquad 1.10$$

where ε is the roughness factor of the pipe. This is an implicit type equation which includes experimental result for both smooth and rough pipes. Equation 1.10 is defined for $Re \geq 4000$.

In addition to frictional pressure loss, losses also incur due to rapid changes in fluid velocity [10]. This type of pressure loss is observed for changes in the flow geometry such as a flow contraction, expansion or any other obstruction in the flow path. Viscous dissipation is also another part of this type of pressure loss which adds more complexity to the problem [14].

1.3.2 Fluid flow analysis for sudden contraction

Investigation of flow through a sudden contraction in the flow geometry at a high Reynolds numbers had started as early as 1929. Johansen et al. [15] studied flow through a contraction using a flow visualization experiment with water ($\nu = 1 \times 10^{-3}$ m^2/s), castor oil ($\nu = 1.293 \times 10^{-3}$ m^2/s) and mineral oil ($\nu = 1.14 \times 10^{-3}$ m^2/s at 18 °C) as the working fluids for sharp edge orifices with different diameter ratios ($\beta =$ 0.794, 0.595, 0.401, 0.209, 0.090). The main objective was to determine the coefficient of discharge (C_d) over a wide range of Reynolds number ($Re =$ 1 - 25,000). It was observed that steady symmetric flow across the orifice plane occurred for Reynolds number (based on length scale as orifice diameter) less than 10. With an increase of Reynolds number (~30) a rapidly divergent jet was reported to be shown. The flow was reported to be attached with the wall again at half of the pipe diameter distance $\left(\frac{D}{2}\right)$ downstream of the orifice. Within the range of Reynolds number (100 - 250) a less divergent jet was observed with increased distance between orifice plane and attachment point with the wall downstream of the flow. Also a small return flow from the pipe wall back to the orifice was reported with increasing Reynolds number. Turbulent flow was visible downstream of the orifice for $Re \geq 250$. Even with the turbulence region in the downstream, the coefficient of discharge was reported not to change for a constant pressure drop. With turbulent flow the jet became shorter in length with increased divergence [15]. In the turbulence region vortices were reported to show with scale dependent on Reynolds number. Johansen et al. [15] also reported that the transition from laminar to turbulence region increases with increased diameter ratio.

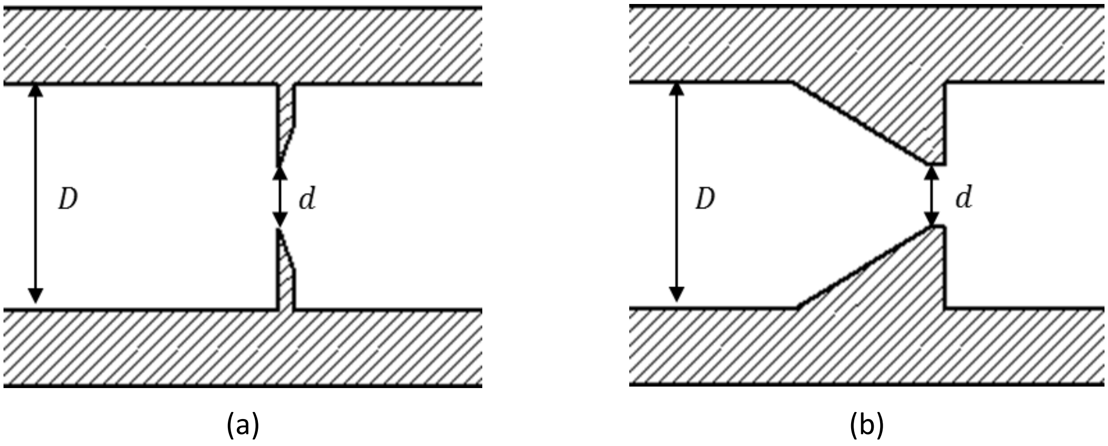

(a)

(b)

Figure 1.6 Geometry of (a) Sharp edge orifice and (b) Quadrant edge orifice (*after* [16])

Alvi et al. [17] undertook experimental work to compare the flow characteristics between a sharp and quadrant edge orifices with nozzles. The geometry of these are shown in Figure 1.6. The work also divided the flow region into four different regimes, namely fully laminar regime, critical Reynolds number regime, relaminarising regime and turbulent regime. Pressure loss coefficient was analyzed based on these regimes. Their experimental work was within the Reynolds number (based on length scale as pipe diameter) range of 1 - 10,000 with diameter ratio $\beta = 0.2$, 0.4, 0.6, 0.8. Four types of fluid were used to cover the whole range of Reynolds number [17] investigated. It has been reported that in the lower region of Reynolds number, the pressure loss coefficient decreases with increasing Reynolds number. The limit of this low Reynolds number region however depends on diameter ratio (β). At high Reynolds number ($Re > 2000$) for all tested diameter ratios, the pressure loss coefficient maintained a constant value. For all the orifices and nozzles at low ($0.2 \leq \beta \leq 0.4$) diameter ratio (β) pressure loss coefficient changes smoothly from laminar to turbulent region. But for high β, a deviation in pressure loss coefficient was reported when flow changed from laminar to turbulent [17]. A local drop in pressure loss coefficient was also reported at $Re = 2000$ for high diameter ratio (β). This local drop was associated with the initialization of turbulence in the upstream of the orifice [17]. It was also reported that for the laminar region the nozzle pressure loss was highest while in the turbulent region it was lowest. The sharp edge orifice was reported to have the maximum amount of pressure loss for moderate to high Reynolds number due to the larger contraction and eddy losses [17].

Dagan et al. [18] presented an infinite series solution using a numerical method for creeping viscous fluid flow through low thickness to diameter ratio ($TD =$ 0 - 2) pores. They constrained their fluid domain within the pore and an infinite half space after the exit plane of the pore. Streamlines showing axial and radial velocity were calculated analytically at the pore entrance and exit. They reported that the velocity profile reaches within 98.5 % of Poiseuille profile after half of the pore radius from the entrance. Pressure drop within this flow domain was reported to have a linear dependence with thickness to diameter ratio $\left(TD = \frac{l}{d}\right)$. They assumed Poiseuille flow through the pore and Sampson's [19] solution outside the pore domain and gave an algebraic equation for pressure drop across the pore as:

$$\Delta P = \frac{Q\mu}{r^3}\left\{\frac{16\left(\frac{l}{d}\right)}{\pi} + 3\right\} \qquad 1.11$$

They also reported that this pressure drop does not account for the upstream influence on the pore opening and entrance effects are only prominent near the pore opening.

Grose [20] first considered viscosity as a factor for flow through contraction (orifice) using an analytical method to solve the Navier-Stokes equation for orifice flow and proposed a viscosity coefficient. According to this work, the coefficient of discharge (C_d) is a product of the contraction coefficient (C_c), the velocity profile coefficient (C_p) and the viscosity coefficient (C_v). So that:

$$C_d = C_c C_p C_v \qquad 1.12$$

At low Reynolds number, the contraction coefficient and the velocity profile coefficient tend to unity, resulting in coefficient of discharge only dependent on the viscosity coefficient [20], [16]. Values are reported for $Re < 16$ where C_d is in good agreement with C_v. It shows that for the low Reynolds number, the hypothesis of this work is correct. At high Reynolds number (by increasing orifice diameter) the contraction coefficient, C_c changes from the value of unity. So at high Reynolds number this theoretical model does not coincide with experimental work.

Sahin et al. [9] presented a numerical solution of the two dimensional Navier-Stokes equation for an incompressible viscous fluid flow through a square edged orifice. They reported the effects of Reynolds number (based on length scale as orifice diameter) and orifice thickness on flow characteristics and also compared the numerical result with their experimental findings. For their experiment they used oil as the working fluid within the range of 30 °C - 50 °C. Due to its high dependency of viscosity on temperature, they recorded the flow rate continuously and adjusted the flow rate using a valve for different viscosity. They also computed the pressure distribution across the orifice using a stream function and vorticity values. They proposed an equation for the coefficient of discharge (C_d) as:

$$C_d = \frac{1}{2\sqrt{2}}\left(\frac{1}{\beta}\right)^2 (1-\beta^4)^{\frac{1}{2}} \frac{1}{\sqrt{P^*}} \qquad 1.13$$

and

$$P^* = \frac{\Delta P}{\rho u^2}$$

where P^* is the non-dimensional pressure loss; ΔP is the static pressure loss across the orifice; and u is the maximum or centerline velocity through orifice. Their numerical result reported that for creeping flow, symmetric eddies were formed upstream and downstream of the orifice. From the experimental result they also showed that with increasing Reynolds number, the length of the downstream eddies increases while that of upstream decreases. With changes in orifice thickness, any considerable change in the length of flow separation zone was not observed for the same Reynolds number.

Hasegawa et al. [8] defined the pressure loss due to the contraction as an excess pressure loss. They reported this excess pressure loss for small orifices (orifice diameter within the range of 10 µm - 1 mm) and with working fluids of water ($\nu = 1 \times 10^{-6}$ m^2/s), silicon oils

($\nu = 1.10 \times 10^{-6}$ m^2/s, 2.22×10^{-6} m^2/s and 5.13×10^{-6} m^2/s) and glycerin solutions ($\nu = 1.69 \times 10^{-6}$ m^2/s, 2.39×10^{-6} m^2/s, 3.44×10^{-6} m^2/s and 5.28×10^{-6} m^2/s). They represented this excess pressure drop as:

$$\frac{2\Delta P}{\rho u^2} = K + \frac{K'}{Re} \qquad 1.14$$

where K and K' are coefficients which depend on Reynolds number and the orifice geometry. They reported that the flow through the contraction has an elongation characteristic and it increases with decreased orifice diameter. They normalized the pressure drop or pressure difference across the orifice with kinetic energy and observed a variation with different kinematic viscosities (ν) and different thickness to diameter ratios $\left(TD = \frac{l}{d}\right)$. They also compared these experimental results with their numerical results and theoretical analysis of creeping flow. They reported that with increasing thickness to diameter ratio $\left(TD = \frac{l}{d}\right)$ the pressure loss decreases and at low Reynolds number the pressure loss calculated from creeping flow analysis coincides with that one calculated from numerical analysis. For orifice diameters larger than 65 µm, the pressure loss data from experiments is in good agreement with the numerical result. They also investigated the effect of orifice material, burring during manufacturing and boundary layer thickness on pressure loss but did not find any significant result to report.

Zhang et al. [21] modeled local pressure drop due to a contraction as an orifice flow and compared between sharp edged orifices and streamlined orifices. They developed an experimental setup with an orifice of diameter ratio (β) within the range of 0.5 - 0.8 and the range of Reynolds number was 10,400 – 20,000 (based on length scale and velocity scale of the pipe). They reported that an optimization for contraction ratio and abruptness minimize the local pressure drop. They normalized the head loss coefficient as:

$$\Delta h = \frac{U^2}{2g} \qquad 1.15$$

where Δh is the head loss across the orifice. They suggested two ways to minimize this local pressure loss, either by increasing the abruptness transition or by reducing the diameter ratio (β).

Morris et al. [22] analyzed normally impinging confined liquid jets numerically. They modeled their contraction domain as an orifice plate of diameter 3.18 mm and 6.35 mm for Reynolds numbers (based on length scale and velocity scale of orifice) of 8,500 - 23,000. They reported that their predicted pressure drop across the orifice was within 95% of published experimental data. However, their numerical model failed to predict the secondary recirculation zone observed in their experiments. They reported that the recirculation length for both $Re = 8{,}500$ and $Re = 23{,}000$ are in good agreement with the data from Ward-smith [23]. It was proposed that in the fully turbulent region, the length of the recirculation zone does not depend on Reynolds number. They showed that for $\frac{l}{d} < 4$ the exit velocity profile is not uniform and for $\frac{l}{d} > 4$ the exit velocity profile is fully developed. Pressure drop across the orifice was expressed in a non-dimensional form of coefficient of discharge as:

$$C_d = \left\{u^2(1-\beta^2)\frac{\rho}{2\Delta P}\right\}^{\frac{1}{2}} \qquad 1.16$$

They modified the empirical correlations proposed by Ward-smith [23] employing an adaptive combination of the Gauss-Newton and Levenverg-Marquardt algorithms. The correlations for the contraction coefficient were:

For:

$0 < \frac{l}{d} < 0.9;$

$$C_d = 0.255\left\{1 + \left(\frac{l}{d}\right)^{2.195}\right\} + \frac{0.356}{\left(1 + \frac{l}{d}\right)^{0.140}} \tag{1.17}$$

For:

$0.9 < \frac{l}{d} < 2.5;$

$$C_d = 0.876 - 0.139\left(\frac{l}{d}\right) - \frac{0.084}{\frac{l}{d}} \tag{1.18}$$

For:

$2.5 < \frac{l}{d} < 9.5;$

$$C_d = 0.292\left\{1 + \left(\frac{l}{d}\right)^{-0.069}\right\} + \frac{0.292}{\left(1 + \frac{l}{d}\right)^{0.150}} \tag{1.19}$$

They proposed that these correlations are valid for $0 < \beta < 0.0635$. According to this result, for diameter ratio (β) within this range and thickness to diameter ratios $\left(TD = \frac{l}{d}\right)$ within the range of $0 < \frac{l}{d} \leq 9.5$ the pressure loss can be predicted.

Gan et al. [24] experimentally studied the pressure loss characteristics for a square edged orifice and a perforated plate having the same cross sectional area. Air was used as the working fluid and the Reynolds number was within the range of 160,000 - 370,000. It was proposed that for the thick orifice, the pressure loss included not only losses due to the sudden contraction and sudden expansion but also frictional loss within the orifice. They defined pressure loss coefficient, K_l as:

$$K_l = \frac{\Delta P}{\frac{1}{2}\rho U^2} \tag{1.20}$$

where U is the average velocity in the pipe. They proposed that for an orifice which has an axis coincident with the pipe, the pressure loss coefficient is mainly dependent on the free area ratio (defined as the ratio of cross sectional area of orifice to that of duct or pipe), thickness to diameter ratio $\left(TD = \frac{l}{d}\right)$ and Reynolds number. They suggested that the variation of their result from Miller [25] is due to less minimum distance between the orifice edge and the edge of the duct. They deducted that if the duct was circular in cross section, that the distance would have been doubled and would cause more blockage at higher velocity. So, they implied that the velocity distribution is one more factor that dictates pressure loss characteristics. They found that for same free area ratio, the pressure loss coefficient is higher for the perforated hole than for the orifice plate. They also developed a numerical model to predict pressure loss coefficient and to show the effect of thickness to diameter ratio $\left(TD = \frac{l}{d}\right)$ on it. This showed that the pressure loss coefficient decreases with increasing thickness to diameter ratio $\left(TD = \frac{l}{d}\right)$ up to 1.5 and after that it again increases with that ratio $\left(TD = \frac{l}{d}\right)$.

Astrita et al. [26] experimentally investigated the sudden pressure loss factor for laminar flow. By comparing with a theoretical model, they showed that pressure loss for laminar flow through a sudden contraction is much higher than theoretically presumed. They defined pressure loss as:

$$\Delta P = \left(K + \frac{K'}{Re}\right)\frac{\rho u^2}{2} \qquad 1.21$$

where K and K' are the Couette and Hagenbach correction factors respectively. They used water and two other aqueous glycerin solutions (0.95 cP - 10 cP) which covered the range of Reynolds number from 10 - 2,000. They also reported a critical Reynolds number ($Re = 146$) before which the pressure loss is dominated by Hagenbach correction factor and after which it is dominated by Couette correction factor. Their correlations are:

For $\mathrm{Re} < 146$;

$$\Delta P = \frac{795}{Re}\frac{\rho u^2}{2} \qquad 1.22$$

For $\mathrm{Re} > 146$;

$$\Delta P = 5.48\frac{\rho u^2}{2} \qquad 1.23$$

However, they suggested that these factors are not general and might be dependent on the geometry of the contraction.

According to Finlayson et al. [27], pressure loss can be divided into two sections. Part of the pressure loss at a contraction is due to a change of momentum and the rest is due to viscous dissipation. An empirical equation was proposed for this. They conducted simulation work for different diameter ratios (β) for a low range of Reynolds number. According to Finlayson et al. [27].

$$\Delta P = \rho u^2(1-\beta^2) + k_l \frac{\mu u}{D_h} \qquad 1.24$$

where k_l is an empirical factor. Simulation results were used to calculate k_l for different Reynolds number.

Bhora et al. [16] analyzed pressure drop characteristics through small circular orifices for highly viscous fluids. They normalized the pressure loss as the Euler number (Eu). Euler number was reported to have a strong dependence on Reynolds number and also increased with thickness to diameter ratio $\left(TD = \frac{l}{d}\right)$. An empirical model was developed showing that Euler number is a function of diameter ratio (β), thickness to diameter ratio $\left(TD = \frac{l}{d}\right)$, viscosity ($\mu$) and Reynolds number ($Re$). These relationships are:

For $Re < 6$;

$$Eu = \left(\frac{1}{Re^{1.203}}\right)\left\{64 \times \left(\frac{l}{d}\right)^{1.502} \mu^{-0.47} + 36 \times \pi\right\} \qquad 1.25$$

where Eu = Euler number, Re = Reynolds number, μ = dynamic viscosity.

For $Re > 6$;

$$Eu = \left[\left\{ \left(\frac{1}{Re^{0.882}} \right) \left(64 \times \left(\frac{l}{d} \right)^{1.159} \mu^{-0.470} \beta^{0.075} + 17.16 \times \pi \right) \right\}^{3} + \left\{ \frac{1 - \beta^{4}}{C_d^{2}} \right\}^{3} \right]^{\frac{1}{3}} \qquad 1.26$$

where C_d = coefficient of discharge. They proposed that these correlations are valid for $0.32 < \frac{l}{d} < 5.72$, $0.02 < \beta < 0.137$ and $0.085 < Re < 9677$.

Jain et al. [28] investigated the pressure loss flow rate relationship for high thickness to diameter ratios $\left(TD = \frac{l}{d} \right)$ and low Reynolds numbers. They also compared experimental data with simulation model results. They covered a wide range of viscosity (1 cP - 3000 cP). One of their main objectives was to investigate the effect of sand particles on the fluid's viscosity and hence pressure loss. They normalized pressure drop as the Euler number (Eu). They reported a lower pressure drop than that reported by Bhora et al. [16]. They argued that the scale was different due to the difference in geometry. They also reported that for same flow rate, highly viscous fluid exhibits high pressure loss.

1.3.3 Axis switching of flows (jet) through rectangular slots

The literature contains several works that have investigated jet flows exiting from rectangular slots. While the reported research area has not focused on the flow through the slot there are similarities with the same fluid flow phenomena as current study. Flow through a rectangular slot with no side wall is defined as rectangular jet although rectangular shape is only assumed at the exit plane [29]. Despite the presence of many variables of this type of flow, the main objective of this section is to review the jet flow phenomenon including axis switching, jet instability and slot aspect ratio (AR_j).

Marsters et al. [30] undertook experimental work to analyze flow through a rectangular slot to determine the effect of aspect ratio (AR_j). Air was used as the working fluid with slots of four aspect ratios (AR_j = 3.39, 6.44, 9.07, 11.88) of variable cross section. A wide range of Reynolds number (33,000 – 57,700) was covered with this experiment. It was reported that with increasing aspect ratio (AR_j) a pronounced peak in the span wise total pressure distribution occurs and persists for some length downstream from the slot [30]. They proposed that this type of saddle backed behaviour is normal in orifice plate nozzles.

Quinn [31] investigated the effect of aspect ratio (AR_j) on turbulent free jets for four aspect ratios (AR_j= 2, 5, 10, 20) with a sharp edged orifice nozzle. It was observed that with increasing aspect ratio, the speed of flow mixing (the rate of momentum transport) in the near field also increases [31]. Based on jet geometry, the major and minor axes of a jet could rotate downstream of the flow, which is defined as axis switching [32]. Gutmark et al. [33] suggested that the basic mechanism for axis switching is because of the Biot-Savart deformation of vortex rings due to non-uniform azimuthal curvature and the interaction between azimuthal and streamwise vorticities [32].

Yu et al. [32] used numerical analysis to investigate the effect of aspect ratio (AR_j) on axis switching and orientation of switching. Slots of five different aspect ratios (AR_j= 1, 1.5, 2, 2.5, 3) were experimented with the range of Reynolds number from 100 to 250. It was reported that 45° switching occurs at the same downstream location (at a distance around 2.5a where a

is the length of the slot) of the jet but the shape of the jet deforms along the aspect ratio (AR_j). It was also suggested that the axis switching effect is due to a change in aspect ratio and corner effects. A 90° axis switching was observed closer to the jet inlet for small AR_j rather than large AR_j.

Yu et al. [34] also used the Lattice Boltzmann method to analyze axis switching for rectangular slots with different aspect ratios (AR_j = 1, 1.5, 2) within the range of Reynolds number (length scale based on slot width) from 10 to 200. No axis switching was observed for this configuration of setup. It was reported that at low Reynolds number ($Re < 100$), rectangular jets tend to become circular and axis switching was present for all three AR_j ratios only for high Reynolds numbers. The change of orientation was dependent on aspect ratio for all slot configurations.

One other jet parameter investigated in the literature is jet instability. Yu et al. [34] reported that at low Reynolds number ($Re < 100$) the laminar jet was stable for all slot geometries. At $\mathrm{Re} = 150$, the square jet exhibited unstable jet behaviour. It was observed that unstable behaviour started from the exit plane of the slot and propagated downstream making the whole jet unstable.

Sato et al. [35] analyzed the stability of a rectangular jet experimentally. The flow regimes were characterized according to Reynolds number (based on slot width). It was proposed that for $Re < 10$, the jet is laminar and for $10 < Re < 50$ the jet is in the transition zone. Two rectangular slots of variable cross section with aspect ratio AR_j = 90 and 150 were used with the range of Reynolds number from 12 to 1,200. It was reported that at low Reynolds number velocity fluctuation was observed in a small region and it propagated in a boarder range with higher Reynolds number.

1.4 Conclusion

This literature review gives an understanding of different flow characteristics and pressure loss phenomena for viscous flow through sudden contraction. Most of the work reviewed gives an indication that pressure loss across a contraction is a function of geometry. Less work has been under taken to emphasize the effect of fluid property (viscosity) on pressure loss for lower range of the Reynolds number. General characteristics (effect of diameter ratio) of pressure loss over a wide range of Reynolds number were analyzed.

1.5 Objective of this work

From the discussion of the literature it is evident that a considerable amount of work has been done to analyze the flow characteristics for flow through narrow slots. Still there are some gaps within the range of variables that need to be addressed. Most of the research work did not take account for the effect of the viscosity factor on pressure loss calculation. Although they have used different fluids, they have done it to cover the range of Reynolds number of their interest rather than investigate the effects of viscosity. In most of the cases the thickness to diameter ratio $\left(TD = \frac{l}{D_h}\right)$ was < 5. At low Reynolds number the flow characteristics were not analyzed for low diameter ratio (β). The lowest diameter ratio experimented was with the range of $0.2 < \beta < 0.8$. This work will emphasize to see the effect of pressure loss at low Reynolds number ($Re \leq 30$) with low diameter ratio ($\beta < 0.1$) and wider range of thickness to diameter ratio ($1 < \frac{l}{D_h} < 10$). Another question that needs to be answered is the effect of slot shape and change of aspect ratio of the slot. For this aspect ratio of slot (AR_j) is varied from 1 - 100 and slot shape is changed from streamlined, rectangular to circular keeping the cross sectional area the same.

The operating range of variables (diameter ratio, thickness to diameter ratio, aspect ratio, slot shape and Reynolds number) are selected with an intention to get an overview of the pressure loss characteristic observed across the slot in a slotted liner during oil production in the SAGD operation. This work also aims to determine the dominating variables for the pressure loss across the slot in a slotted liner.

1.6 Thesis Organization

This thesis is organized into several chapters. The chapters are outlined as-

- Chapter 1: A general overview of the problem and objective are explained. Necessary background is also explained here in literature review section.
- Chapter 2: Development of the theoretical model is discussed. Theoretical models for non-Newtonian fully developed velocity profile and pressure loss coefficient for narrow slot are derived.
- Chapter 3: The test facility is introduced along with all the equipment and testing procedures.

- Chapter 4: Experimental results are discussed for the effect of viscosity and slot shape. Effect of different shapes (circular, rectangular, streamlined) slot width and fluid viscosity is discussed.
- Chapter 5: Experimental results for thickness to diameter ratio $\left(TD = \frac{l}{D_h}\right)$ are discussed. Pressure loss characteristics for rectangular slot for a range (1-100) of aspect ratio (AR_j) are also discussed in this chapter.
- Chapter 6: Gives a conclusion about the findings and future recommendation.

Chapter 2: Development of the analytical model for flow in a slot

The theoretical model for a non-Newtonian fully developed velocity profile and pressure drop across a sudden contraction is developed here. For describing any fluid dynamic problem, there are different theoretical approaches. In this chapter these approaches will be introduced briefly followed by the derivation of the theoretical models based on one of the approaches.

One of the eminent approaches for model development is the conservation of momentum for any arbitrary control volume of a fluid. Here, one major assumption is that momentum for that control volume is conserved. Also, based on the fluid flow scenario, different forces (electrostatic force, magnetic force etc.) are neglected. This approach can be used for both steady, unsteady, viscous, inviscid, Newtonian, non-Newtonian flow [36]. Based on Newton's second law, conservation of momentum can also be referred to as Navier-Stokes equation [36].

Another approach is the Euler's approach [37]. Based on the Navier-Stokes equation this approach assumes only inviscid and steady state flow. Euler's equation addresses fluid flow parameters (velocity, pressure drop) as a vector field while Bernoulli's equation [37] assumes the flow as unidirectional or average parameters are used. Bernoulli's approach also neglects viscous terms in the energy balance.

Sometimes a mechanical energy balance is also used to describe a fluid flow [36]. It is common practice for mechanical energy to refer to as the summation of kinetic energy, potential energy and energy associated with pressure difference. Bernoulli's equation can also be derived from an energy balance of the flow system. This approach will depend on how different terms in the energy balance are defined.

Conservation of momentum is the only approach which describes fluid flow phenomena in a more general way than any other approach and it also takes viscous forces into consideration. As the main objective of this work is to confirm whether viscosity has any effect on pressure drop, the conservation of momentum approach is chosen for developing the theoretical model.

2.1 Velocity profile of Newtonian and non-Newtonian fluid

It has been well established [11] that Newtonian fluid show a parabolic shape velocity profile once the fully developed condition is reached for laminar flows. As a non-Newtonian fluid is being used in a practical scenario (chemical industry, food processing industry, bio-fluid etc.), a more detailed view is necessary for fully developed flow for this type of fluid.

A Newtonian fluid is defined as a type of fluid which has linear relationship between shear stress (τ) and strain rate $\left(\frac{\partial u}{\partial y}\right)$. A non-Newtonian fluid is defined as the type of fluid which has non-linear relationship between shear stress (τ) and strain rate$\left(\frac{\partial u}{\partial y}\right)$. These can be further categorised as:

- Shear thickening fluid
- Shear thinning fluid
- Bingham plastic
- Time dependent non-Newtonian fluid
- Time independent non-Newtonian fluid

The response for some of these different types of fluids are shown graphically in Figure 2.1 highlighting the change shear stress (τ) with increasing strain rate $\left(\frac{\partial u}{\partial y}\right)$ [38]. From this a fundamental definition for viscosity for a Newtonian fluid can be defined as:

$$\tau = \mu\left(\frac{\partial u}{\partial y}\right) \tag{2.1}$$

where μ is the viscosity, u is the velocity along x direction.

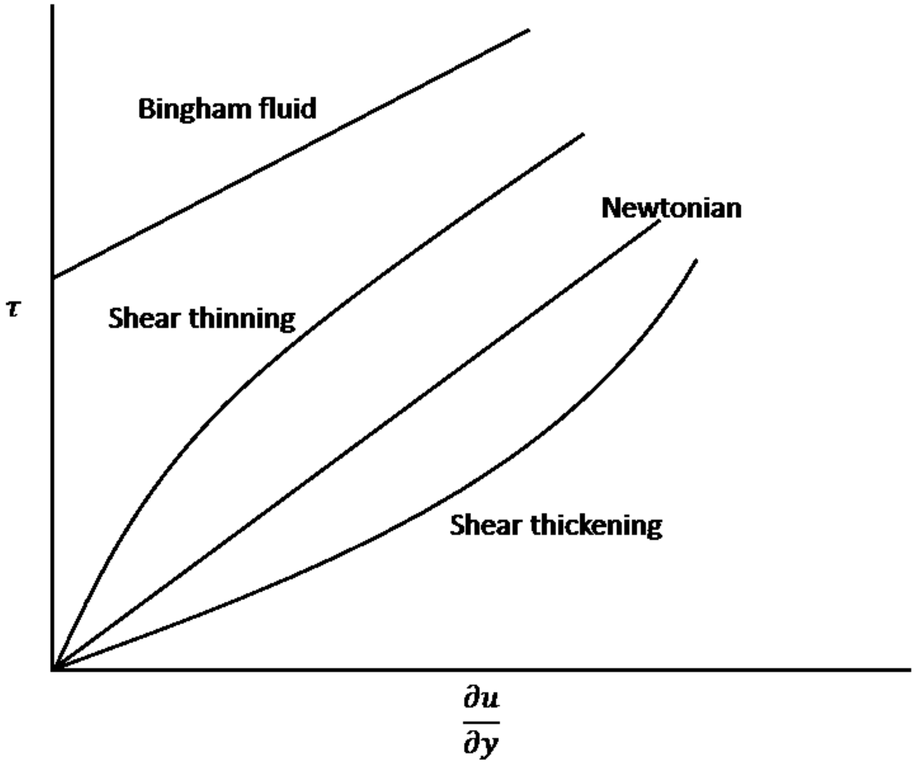

Figure 2.1 Shear stress and strain rate relationship for different fluids(*after* [38])

There are different models to represent a non-Newtonian fluid, but a power law model [38] will be used in the approach developed here. The fully developed velocity profile for shear thickening and shear thinning will be developed and compared with a Newtonian fluid. Figure 2.2 shows the flow domain for analyzing the fully developed velocity profile for non-Newtonian fluid. At the inlet of a channel with depth of $2H$, fluid is assumed to flow at uniform velocity ($u = U$) in the x direction. After some length it attained fully developed velocity profile having maximum velocity (u_{max}) along the channel mid plane and a no slip condition (u = 0) at the wall is prescribed.

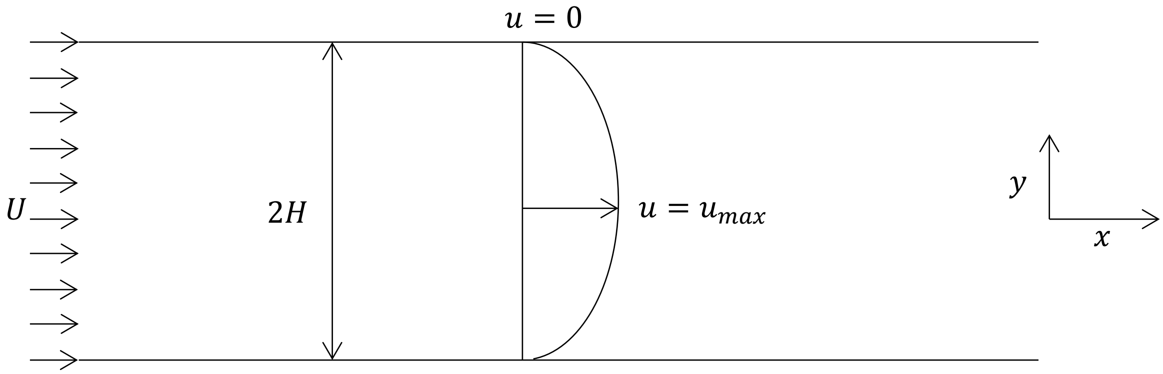

Figure 2.2 Schematic diagram of flow domain for the theoretical modelling

According to power law model or Ostwald de Waele equation [38]

$$\tau_{xy} = m\left(\frac{\partial u}{\partial y}\right)^{n}$$

$$\mu_{eff} = m\left(\frac{\partial u}{\partial y}\right)^{n-1}$$

where m is the consistency index , n is the power law index and μ_{eff} represents the effective viscosity for the non-Newtonian fluid. The power law index (n) dictates the behaviour of non-Newtonian fluid. For $n > 1$, the fluid is defined as shear thickening and for $n < 1$, it is defined as a shear thinning fluid.

General conservation of momentum can be expressed as:

$$\rho \frac{D\vec{u}}{Dt} = -\nabla P + \nabla . \vec{\tau} + \vec{g} \qquad 2.2$$

General conservation of momentum along x direction can be expressed as:

$$\rho\left(\frac{\partial u}{\partial t} + u\frac{\partial u}{\partial x} + v\frac{\partial u}{\partial y} + w\frac{\partial u}{\partial z}\right) = -\frac{dp}{dx} + \frac{\partial}{\partial x}(\tau_{xx}) + \frac{\partial}{\partial y}(\tau_{xy}) + \frac{\partial}{\partial z}(\tau_{xz}) + g_c \qquad 2.3$$

where ρ is the density and u, v, w are fluid velocities along x, y, z direction respectively. $\tau_{xx}, \tau_{xy}, \tau_{xz}$ are stresses along x, y, z direction. dp is the pressure differential between upstream and downstream, t is time and g_c is defined as the body force for an arbitrary fluid volume.

Assumptions for this flow domain are:

- Compressible flow
- Flow only in the x direction. So $v, w = 0$
- Steady state flow. $\frac{\partial u}{\partial t} = 0$
- Fully developed flow. $\frac{\partial(variable)}{\partial x} = 0$

For a power law fluid [39]

$$\tau_{xx} = \mu_{eff}\left(\frac{\partial u}{\partial x} + \frac{\partial u}{\partial x}\right)$$

$$\tau_{xy} = \mu_{eff}\left(\frac{\partial u}{\partial y} + \frac{\partial v}{\partial x}\right)$$

Since it is assumed that the flow is fully developed, so $\tau_{xx} = 0$ and $\tau_{xy} = \mu_{eff}\frac{\partial u}{\partial y}$. From this, equation 2.3 becomes:

$$-\frac{dp}{dx}+\frac{\partial}{\partial y}\left(\mu_{eff}\frac{\partial u}{\partial y}\right)=0 \tag{2.4}$$

The fully developed velocity profile can be derived by solving this differential equation.

Starting with equation 2.4, this equation can be manipulated as follows with the aim to isolate the velocity gradient, a representation of the velocity profile shape, as:

$$-\frac{dp}{dx}+\frac{\partial}{\partial y}\left(\mu_{eff}\frac{\partial u}{\partial y}\right)=0$$

$$-\frac{dp}{dx}+\frac{\partial}{\partial y}\left(m\left(\frac{\partial u}{\partial y}\right)^{n}\right)=0$$

$$\frac{\partial}{\partial y}\left(m\left(\frac{\partial u}{\partial y}\right)^{n}\right)=\frac{dp}{dx} \tag{2.5}$$

Integrating equation 2.7 along the channel width with respect to the cross stream axis to define a velocity gradient as:

$$\int\frac{d}{dy}\left(m\left(\frac{\partial u}{\partial y}\right)^{n}\right)dy=\int\frac{dp}{dx}dy$$

$$m\left(\frac{du}{dy}\right)^{n}=y\frac{dp}{dx}+c_1$$

$$\frac{du}{dy}=\left(\frac{y}{m}\frac{dp}{dx}+c_1^{e}\right)^{\frac{1}{n}} \tag{2.6}$$

This equation can now be integrated with respect to the cross stream axis to define a velocity profile such that:

$$\int \frac{du}{dy} dy = \int \left(\frac{y}{m}\frac{dp}{dx} + c_1^e\right)^{\frac{1}{n}} dy$$

$$u(y) = \frac{\left(\frac{y}{m}\frac{dp}{dx} + c_1^e\right)^{\frac{1}{n}+1}}{\frac{1}{m}\frac{dp}{dx}\left(\frac{1}{n}+1\right)} + c_2 \qquad 2.7$$

Since at $y = 0$,$\frac{du}{dy} = 0$ so from equation 2.6:

$$0 = (0 + c_1^e)^{\frac{1}{n}}$$

$$c_1^e = 0$$

Also since at $y = H$, $u = 0$, so from equation 2.7:

$$0 = \frac{\left(\frac{H}{m}\frac{dp}{dx} + c_1^e\right)^{\frac{1}{n}+1}}{\frac{1}{m}\frac{dp}{dx}\left(\frac{1}{n}+1\right)} + c_2$$

$$c_2 = -\frac{\left(\frac{y}{m}\frac{dp}{dx} + c_1^e\right)^{\frac{1}{n}+1}}{\frac{1}{m}\frac{dp}{dx}\left(\frac{1}{n}+1\right)}$$

Replacing the values of c_1^e and c_2 into equation 2.11 gives:

$$u(y) = \frac{\left(\frac{y}{m}\frac{dp}{dx} + c_1^e\right)^{\frac{1}{n}+1}}{\frac{1}{m}\frac{dp}{dx}\left(\frac{1}{n}+1\right)} - \frac{\left(\frac{H}{m}\frac{dp}{dx} + c_1^e\right)^{\frac{1}{n}+1}}{\frac{1}{m}\frac{dp}{dx}\left(\frac{1}{n}+1\right)} \qquad 2.8$$

After simplification of equation 2.8 the equation for fully developed velocity profile can be written as:

$$u(y) = \frac{n}{n+1}\left(\frac{1}{m}\frac{dp}{dx}\right)^{\frac{1}{n}}\left(y^{\frac{n+1}{n}} - H^{\frac{n+1}{n}}\right) \qquad 2.9$$

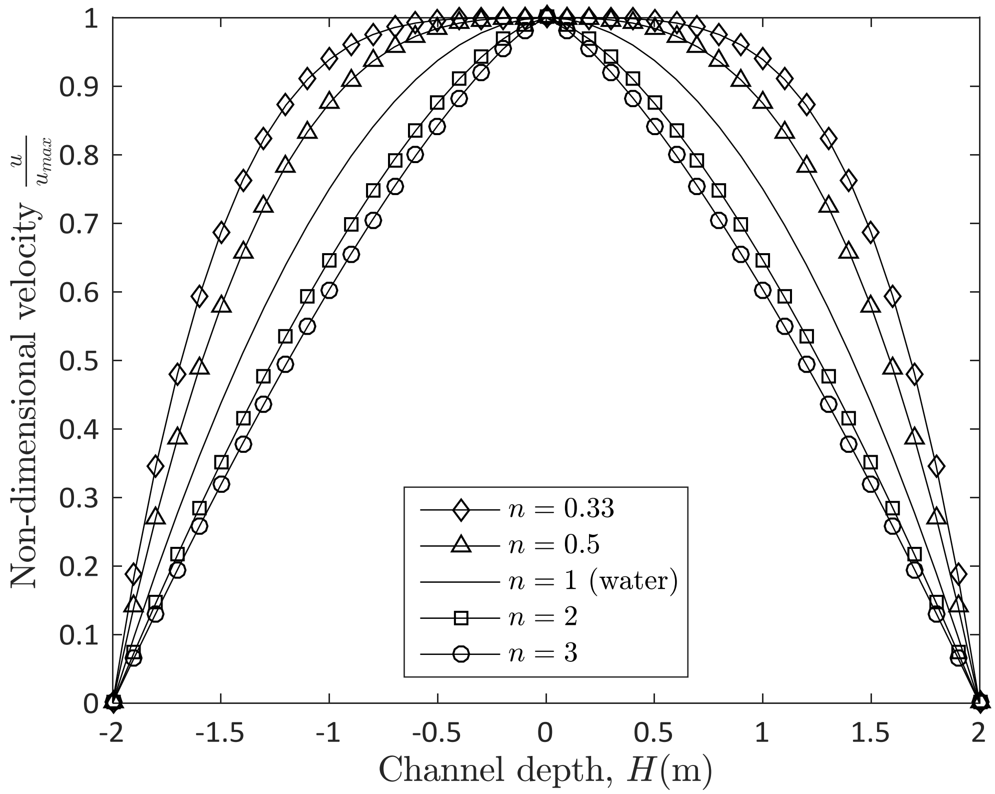

Figure 2.3 Fully developed velocity profile for different non-Newtonian fluid

The theoretically modeled velocity profile in a channel defined by equation 2.9 is plotted in Figure 2.3 for different values of the power law index (n). The figure shows the fully developed velocity profile for shear thickening ($n > 1$) and shear thinning ($n < 1$) fluids and is compared with a Newtonian fluid, such as water for which $n = 1$. For a shear thinning fluid with decreasing power law index, n the velocity profile becomes broader at the center of the channel and obtains a constant velocity for a wider range of channel width. With increasing strain, viscosity decreases for this type of fluid. So, shear strain induced from the channel wall decreases the viscosity of the fluid layers. For a shear thinning fluid, velocity increases in a faster way from the wall to center of the channel and a flatter portion of velocity profile is visible for this type of fluid. But for the case of a Newtonian fluid, viscosity remains constant at every position and a parabolic profile is developed. For shear thickening fluid it is the complete opposite. This is because with applied shear strain it’s viscosity decreases. That is why for shear thickening fluid a sharp velocity profile is observed from this theoretical model.

2.2 Non-dimensional pressure loss for a sudden contraction

In this section a theoretical model of a non-dimensional pressure loss for a sudden contraction will be derived. The main objective of this modelling is to confirm whether viscosity affects the pressure loss for flow through sudden contraction.

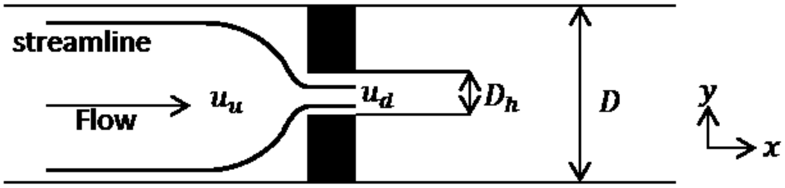

Figure 2.4 Schematic diagram for theoretical modelling of non-dimensional pressure loss

The flow domain for which theoretical modelling is shown in Figure 2.4, where u_u and u_d is upstream and downstream velocity respectively. D_h is the hydraulic diameter of the contraction and D is the diameter of the pipe. For this modelling, conservation of momentum is used. General conservation of momentum can be expressed as:

$$\rho \frac{D\vec{u}}{Dt} = -\nabla P + \mu \nabla^2 \vec{u} + \vec{g} \qquad 2.10$$

Simplified conservation of momentum or Navier-Stokes equation for incompressible flow along x direction can be given as:

$$\frac{\partial u}{\partial t} + u\frac{\partial u}{\partial x} + v\frac{\partial u}{\partial x} + w\frac{\partial u}{\partial x} = -\frac{1}{\rho}\frac{dp}{dx} + v\left(\frac{\partial^2 u}{\partial x^2} + \frac{\partial^2 u}{\partial y^2}\right) + g_c \qquad 2.11$$

where u, v, w are the velocities along x, y and z direction respectively. ρ and ν are density and kinematic viscosity respectively and g_c represents body force of the fluid. dp is the pressure differential. This model can be further simplified using the following assumptions:

1. Flow only along x direction. So $v, w = 0$
2. No gravitational force. g_c=0
3. Steady state flow. $\frac{\partial(variable)}{\partial t}$=0
4. u is changing only along x direction.

So equation 2.11 becomes

$$u\frac{\partial u}{\partial x} = -\frac{1}{\rho}\frac{dp}{dx} + \nu\frac{\partial^2 u}{\partial x^2}$$

$$udu = -\frac{1}{\rho}dp + \nu\frac{\partial^2 u}{\partial x^2}dx \tag{2.12}$$

Grose [20] used the same approach to derive coefficient of discharge (C_d). According to their work [20], velocity is changing from one constant value (from fully developed region) to another one, so they proposed a smooth transition. Their approach represented u as a function of length along flow direction as:

$$u = u_u + u_i erf(\alpha) \tag{2.13}$$

where u_u is the upstream velocity, u_i is instantaneous velocity between upstream and downstream and erf represents the error function. The parameter α is defined as:

$$\alpha = \frac{\phi x}{D_h} \tag{2.14}$$

where ϕ is a proportional factor and D_h is the diameter of the contraction. From equation 2.13 and equation 2.14:

$$\frac{du}{dx} = \frac{2u_i\phi}{\sqrt{\pi}D_h}e^{\left(\frac{-\phi x}{D_h}\right)^2} \tag{2.15}$$

A length l_e can be assumed between the upstream and downstream velocity locations. The upstream velocity and static pressure are defined as u_u and p_u and the downstream velocity and static pressure are defined as u_d and p_d. These upstream and downstream velocities are taken as average velocity of the cross sectional area to allow the application of the following boundary conditions:

1. At $x = 0, \frac{du}{dx} = \frac{2u_i\phi}{\sqrt{\pi}D_h}$
2. At $x = l_e, \frac{du}{dx} = 0$

Integrating equation 2.12 between upstream and downstream locations gives:

$$\int_{u_u}^{u_d} udu = -\frac{1}{\rho}\int_{p_u}^{p_d} dp + \nu \int_{\frac{2u_i\phi}{\sqrt{\pi}D_h}}^{0} \frac{\partial^2 u}{\partial x^2}dx$$

Solving the integration gives:

$$\frac{u_d^2 - u_u^2}{2} = -\frac{1}{\rho}(p_d - p_u) + \nu\left(0 - \frac{2u_i\phi}{\sqrt{\pi}D_h}\right)$$

$$u_d^2 - u_u^2 - \frac{2}{\rho}(p_d - p_u) + \frac{4\phi\nu u_i}{\sqrt{\pi}D_h} = 0 \tag{2.16}$$

From the conservation of mass:

$$\rho u_u A_u = \rho u_d A_d$$

$$u_u = \frac{A_d}{A_u} u_d$$

$$u_u = \beta^2 u_d \tag{2.17}$$

where A_u= cross sectional area in the upstream section (area of the flow channel), A_d= cross sectional area in the downstream section (cross sectional area of the contraction region) $\beta = \frac{D_h}{D}$, is the diameter ratio between contraction and flow channel. Also at $x = l_e$, $u = u_d$. So, from equation 2.13 and equation 2.14:

$$\begin{aligned}
u_d &= u_u + u_i \\
u_i &= u_d - u_u \\
u_i &= u_d - \beta^2 u_d \\
&= u_d(1-\beta^2)
\end{aligned} \tag{2.18}$$

Defining $p_d - p_u = \Delta P$ and using the value of u_u from equation 2.17 and u_i from equation 2.18 into equation 2.16:

$$\begin{aligned}
u_d^2 - (\beta^2 u_d)^2 - \frac{2}{\rho}\Delta P + \frac{4\phi\nu u_d(1-\beta^2)}{D_h\sqrt{\pi}} &= 0 \\
u_d^2 - \beta^4 u_d^2 - \frac{2}{\rho}\Delta P + \frac{4\phi\nu u_d(1-\beta^2)u_d}{D_h u_d\sqrt{\pi}} &= 0 \\
u_d^2(1-\beta^4) - \frac{2}{\rho}\Delta P + \frac{4\phi\nu u_d^2(1-\beta^2)}{D_h u_d\sqrt{\pi}} &= 0 \\
u_d^2(1-\beta^4) + \frac{4\phi u_d^2(1-\beta^2)}{\frac{D_h u_d}{\nu}\sqrt{\pi}} - \frac{2}{\rho}\Delta P &= 0
\end{aligned} \tag{2.19}$$

A Reynolds number can be defined as $Re = \frac{D_h u_d}{\nu}$. Substituting into equation 2.18 this becomes:

$$u_d^2(1-\beta^4)+\frac{4\phi u_d^2(1-\beta^2)}{Re\sqrt{\pi}}-\frac{2}{\rho}\Delta P=0$$
$$u_d^2\left\{(1-\beta^4)+\frac{4\phi(1-\beta^2)}{Re\sqrt{\pi}}\right\}-\frac{2}{\rho}\Delta P=0$$
$$\Delta P=\frac{1}{2}\rho u_d^2\left\{(1-\beta^4)+\frac{4\phi(1-\beta^2)}{Re\sqrt{\pi}}\right\} \tag{2.20}$$

Normalized pressure loss can be defined as [19], [24]:

$$P^*=\frac{\Delta P}{\frac{1}{2}\rho u_d^2} \tag{2.21}$$

so that equation 2.20 can be represented as:

$$P^*=(1-\beta^4)+\frac{4\phi(1-\beta^2)}{Re\sqrt{\pi}} \tag{2.22}$$

where ϕ is an empirical factor and depends on geometry of the contraction.

Pressure loss in a non-dimensional form in equation 2.22 shows that it is a function of Reynolds number (Re) and diameter ratio (β). Viscous energy is normalized as Reynolds number. This equation shows that with higher Reynolds number pressure loss decreases. This relation is valid for lower range of Reynolds number where viscous energy is comparable to momentum energy. Figure 2.5 and Figure 2.6 also confirms this statement where the theoretical model is compared with data from Astrita et al.[26]. These figures show that the theoretical model is in good agreement with experimental data for lower range of Reynolds number. One of the assumptions for the theoretical modelling was that streamlines converge smoothly from the main flow channel to the contraction. This assumption is only valid for low range of Reynolds numbers where viscosity is very high or the velocity is very low. That is why theoretical model is in good agreement with experimental data for low range of Reynolds number. For Curve fitting of theoretical model with the experimental data from Astrita et al. [26] non-linear least square method (Matlab 2015a, Mathworks Inc.)was used. Diameter ratio (β) is a geometry factor which also contributes to pressure loss. The theoretical model of equation 2.22 also predicts that a lower diameter ratio would give high pressure loss.

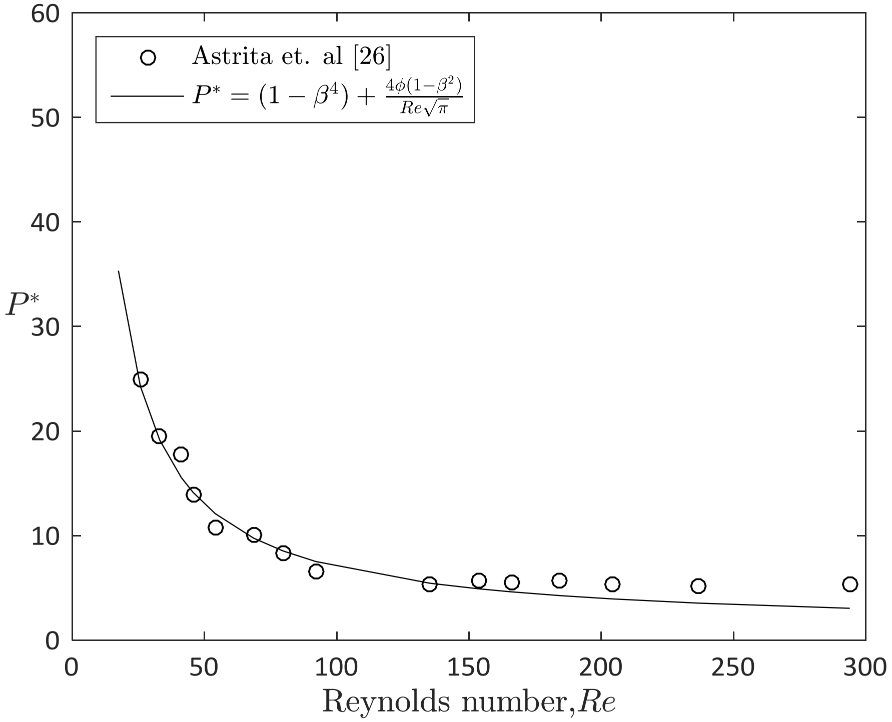

Figure 2.5 Comparing theoretical model with data from Astrita et al. [26] for P^*

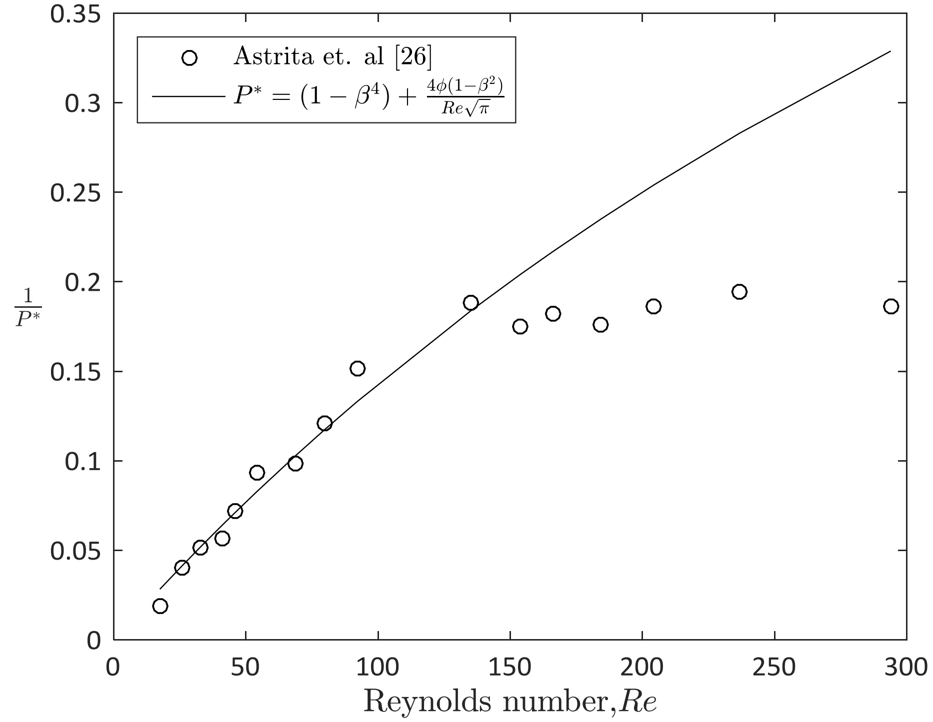

Figure 2.6 Comparing theoretical model with data from Astrita et al. [26] for $\frac{1}{P^*}$

2.3 Conclusion

Conservation of momentum was used as a basic approach to develop theoretical modelling for both fully developed velocity profile of non-Newtonian fluid and non-dimensional pressure loss for sudden contraction. The predicted velocity profiles for non-Newtonian fluid show the impact of the power law index (n) in defining the characteristics of different non-Newtonian fluid. By comparing that velocity profile with basic Newtonian fluid (water) also gives an overview about the behaviour of non-Newtonian fluid. A derived theoretical model for the non-dimensional pressure loss shows the factors (Re, β) dominating that model. For flow through a sudden contraction, pressure loss would decrease with increasing Reynolds number. Also, contractions with smaller diameters (low diameter ratio, β) would create highest pressure loss.

Chapter 3: Experimental setup and procedure

This chapter describes the experimental setup and components within it. The whole setup was designed and developed by RGL Reservoir Management Inc. and was donated to allow this research to be conducted. Their main objective was to measure the effectiveness of different coatings of material on slotted liner plate. Their approach was to evaluate whether different coatings on a slotted liner affects the flow rate through it. To this end, they designed the system to operate at a constant pressure difference ($\Delta P = 4$ psi) across the slot, allowing the flow rate to vary depending on fluid viscosity using an active flow control methodology. This setup is used here in its original configuration to measure pressure drop across different contraction geometries inside a pipe flow. Here, the overall experimental setup is described followed by a discussion about specific components, test section and experimental procedure.

3.1 Description of test facility

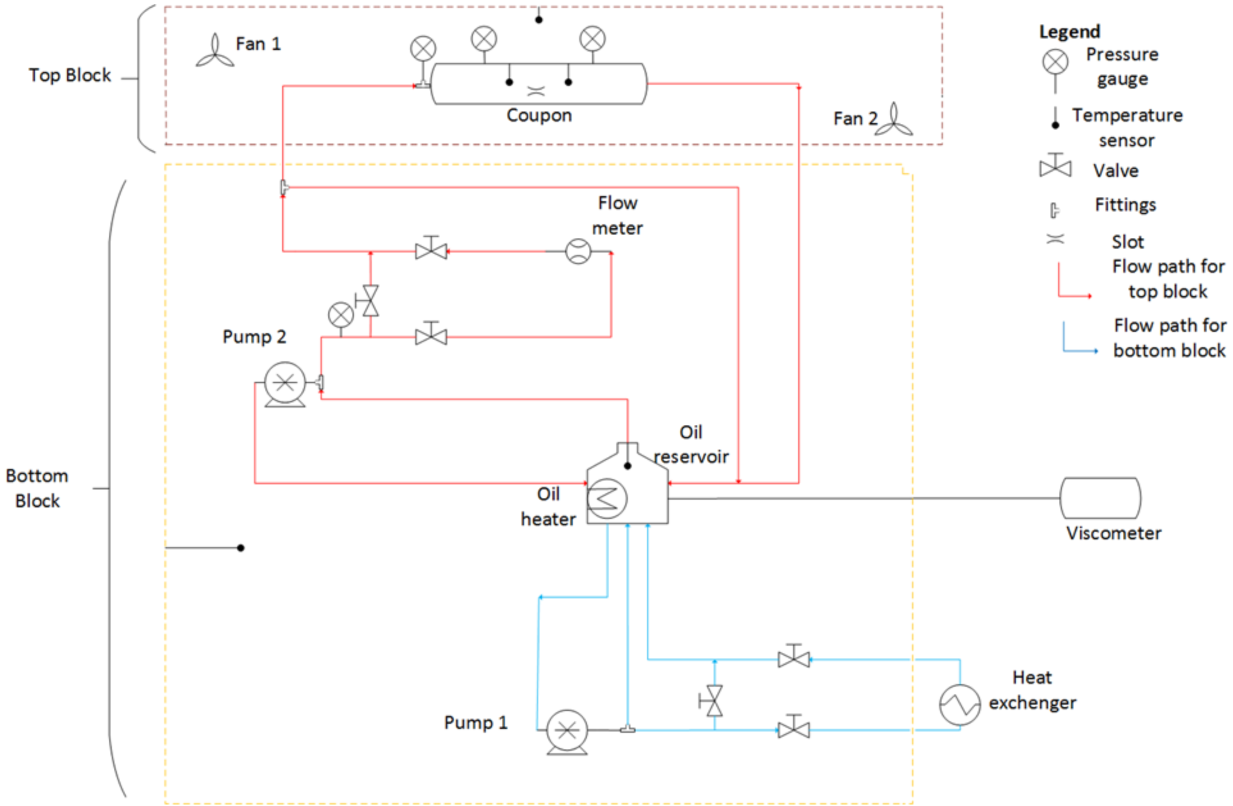

Figure 3.1 Schematic diagram of the experimental setup

Figure 3.1 shows a schematic diagram of test setup. There are two flow loops in the experimental cycle. One loop re-circulates test fluid from reservoir through the recirculation pipe and back to reservoir using pump 1 (large pump). The main purpose of this cycle was to heat up the test fluid in the reservoir uniformly and reduce the chance of having any stratification layer of the test fluid in the reservoir. Pump 2 (small pump) was used to run the second, flow loop. This loop circulates test fluid from reservoir through the test section and back to reservoir and this is the main experimental flow loop.

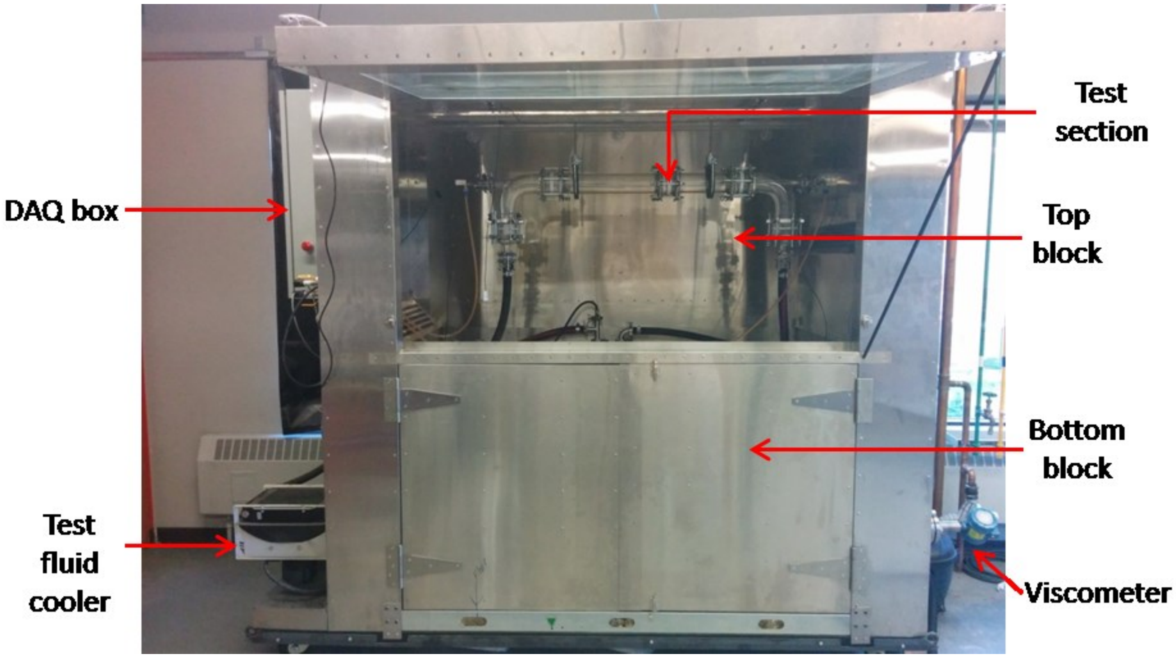

Figure 3.2 Annotated digital image of the actual experimental setup

A digital image is shown in Figure 3.2 of the actual experimental setup. This figure shows that the whole setup is divided into two blocks. The bottom block contains all the pipework, connections, pumps and heater to supply experimental test fluid at the necessary conditions to the test section. The top block contains the main flow channel and the test section which is made of optical glass. Temperature sensors were installed at locations within each block, inside the test fluid reservoir and upstream and downstream of the test section. A heat exchanger was also connected to this setup to cool down the test fluid to ambient temperature after one cycle of the experiment. An in situ viscometer is also shown in the figure with its external transmitter to the bottom block and its transducer within the test fluid reservoir.

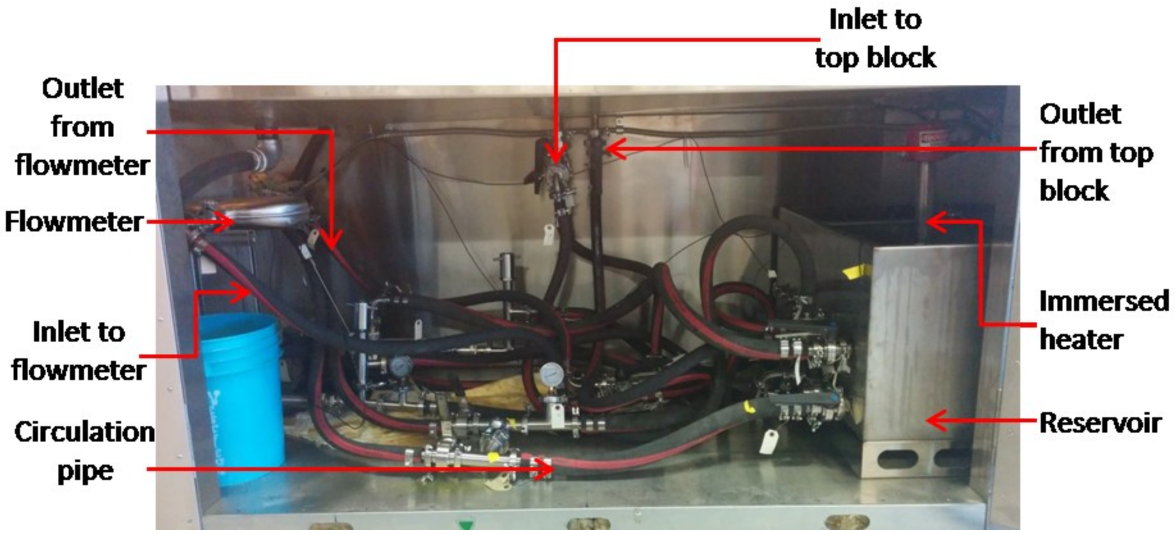

Figure 3.3 Annotated digital image of the bottom block

Figure 3.3 shows an expanded view of the bottom block. The heater was immersed in the test fluid reservoir. Pump 1 was used to circulate test fluid inside the circulation loop so that there is no stratifying layer of fluid in the reservoir. A viscometer was connected with the test fluid reservoir to measure the instantaneous viscosity at the time of heating. A temperature sensor was connected both with the test fluid reservoir and bottom block to measure the temperature of test fluid and bottom block air temperature respectively. Pump 2 was used to flow the heated test fluid to the top block and across the test section. A mass flow meter was connected between pump 2 and top block. The whole piping loop was insulated to keep the test fluid temperature same throughout the whole system.

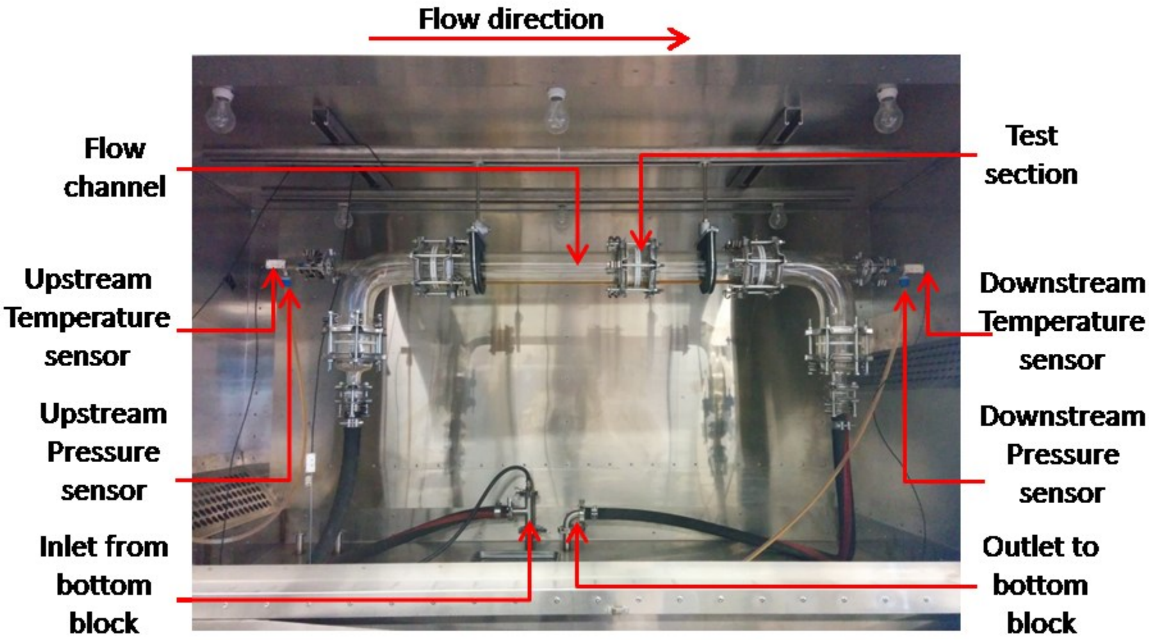

Figure 3.4 Annotated digital image of the top block

Figure 3.4 shows the top block of the test setup. The top block contained the flow channel with the test coupon, pressure and temperature sensors along with fan heaters. The main flow channel was made of borosilicate glass with 76.2 mm (3 in) inner diameter (QVF®, De Dietrich Process Systems). The total length of the channel was 109.2 cm (43 in). The test section was positioned after 66.04 cm (26 in) from the inlet of the flow channel, which was sufficient for fully developed flow in the flow channel. Temperature and pressure sensors were inserted into the flow channel to measure the upstream and downstream pressure and temperature across the test section. An air fan heater was also installed in the top block to blow hot air during experiment to maintain a uniform temperature in the top block. The top block air temperature was also measured.

3.1.1 Components used with the setup

Different mechanical and electrical components were used with this experimental setup. The whole setup was contained in a steel box with sufficient insulation to maintain even operating temperature. A glass door was hinged with the top block for easy access and observation of the experiment. The specifications of all the other components are given below.

Pumps: - Two progressive cavity pumps (N series, D Metering pump, Seepex Inc.) were used for running the whole cycle. Both of these pumps were capable of pumping low to high viscous fluids. One large pump (BN range) was used to circulate fluid from the reservoir through the circulation pipe and back to the reservoir. It's capacity was 0.03 m^3/h - 500 m^3/h with maximum pressure up to 4964 kPa (720 psi). A second (smaller) pump (MD range) was used for circulating flow from reservoir to test section and back to reservoir. This pump was also capable of pumping shear sensitive and chemically aggressive fluids. The capacity of the pump was 0.002 m^3/h – 1 m^3/h with maximum pressure of 2482 kPa (360 psi).

Viscometer: - The test fluid's viscosity was measured with an inline viscometer connected to the test fluid reservoir. A fork type viscosity meter (7827 High performance viscosity meter, Micro Motion Inc.) was used for this purpose. The operating range of this viscometer is 0.5 cP to 20,000 cP. The standard accuracy of this meter is ±0.2 cP for the range of 0.5 cP to 10 cP and ±1 % for the rest of the range. The data was repeatable for ±0.5 % of the reading. Operating temperature range was -50 °C to 200 °C. While the operating range of the viscometer pressure was up to 20 MPa there was no process pressure effect for the current work.

Flow meter: - Flow rate and density were measured using a Coriolis mass flow meter (Micro Motion Elite series, Micro Motion, Inc.). The standard accuracy for mass/volume flow rate is ±0.10 % of the rate and ±0.5 kg/m^3 for density. For electronic parts of the flow meter the temperature range was -40 °C to 60 °C. As the test fluid temperature was outside of this range the compatible transmitter (Series 2700, Micro Motion, Inc.) was installed outside of the setup. For the selected model the process temperature change effect was ±0.001 % of maximum flow rate per °C of temperature. There was no process pressure effect on mass flow rate. Nominal flow rate was 1,050 kg/h and maximum flow rate was 2,100kg/h.

Heater and Fan:- One of the main variables of this experiment was temperature. Test fluid temperature was kept constant throughout the whole experimental setup. It was heated using an over the side immersion heater (TLCP303053, WATTCO^{TM}). The sheath material of the heater was copper and heat source needed 4 KW 240 V single phase 16 A current. To keep the test fluid temperature same at the test section, heated air was supplied to the top box of the experimental setup. To heat up and maintain air circulation 3 axial fan heater units (Series AF20, TUTCO/FARNAM) were used. The fan heaters needed a power source of 240 V, 85 mA current.

3.1.2 Instrumentation and control system

A feedback control system was used to control the flow loop and measurement of data. A data acquisition system (DAQ) connected to the setup logged data in real time. The test fluid reservoir temperature and upper air temperature were synchronized during the heating cycle of the test fluid. Inlet and outlet pressure and temperature of the test section, fluid reservoir temperature, upper air temperature, flow rate, viscosity and density of the test fluid were measured. Pump speed was controlled depending on the viscosity of the fluid.

Industrial RTD sensors (TR40, WikaIntstruments Ltd.) were used to measure all the temperatures. Absolute pressure for both inlet and outlet were measured with pressure transmitter (S-10, WikaIntstruments Ltd.) whose operating range is 0-206.842 kPa (0-30 psi). This type of transmitter has 2 wire output signals with the range of 4-20 mA with an accuracy of $\leq$ 0.25 %. Pumps were controlled using VFD (variable frequency drive) with input signal range 4 - 20 mA.

The control system was based on custom code (LabVIEW, National Instruments Inc.) developed by RGL Reservoir Management. Temperature of the test fluid reservoir was also controlled by controlling the heater output. Another option of the control system was preheating. So this control system could be used for both the running the experiment and preheating the system and fluid before the actual experiment.

3.1.3 Test section

This section describes the whole test section and the different geometries of slots used for the experiment. The sample coupons were named after the circular plate containing the particular shaped slot. The test section was defined as the part containing the coupon. The test section was a separate part of the flow channel. It was designed in a manner so that coupons with the different slots could be assembled and disassembled easily for different experiment runs.

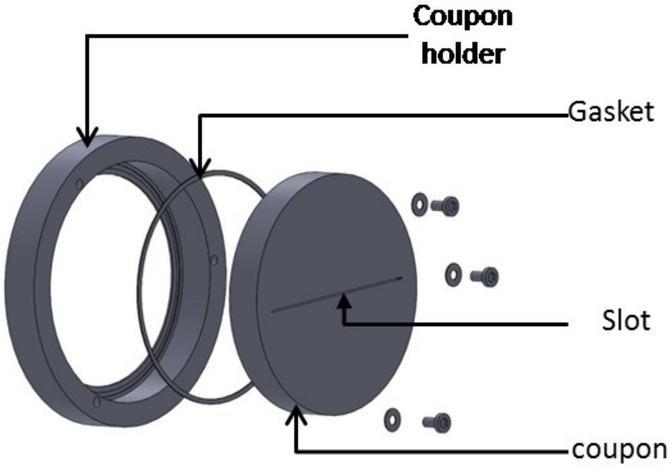

Figure 3.5 Annotated image of the test section

Figure 3.5 shows the whole test section used in the experiment. A gasket was used in the coupon holder to prevent leakage between upstream and downstream of the flow. The coupon was connected in the holder via a nut-bolt connection. Different coupons were made containing different slot geometries. Different slot geometries were made in each coupon and were installed as needed in the test section for the experiment. For the coupon material, acrylic sheet (poly methyl methacrylate, McMaster-Carr) and steel (supplied by RGL) were used. Slots were cut using a laser cutter for the acrylic sheet and metal cutting blade (part of RGL's manufacturing process) for the steel coupons.

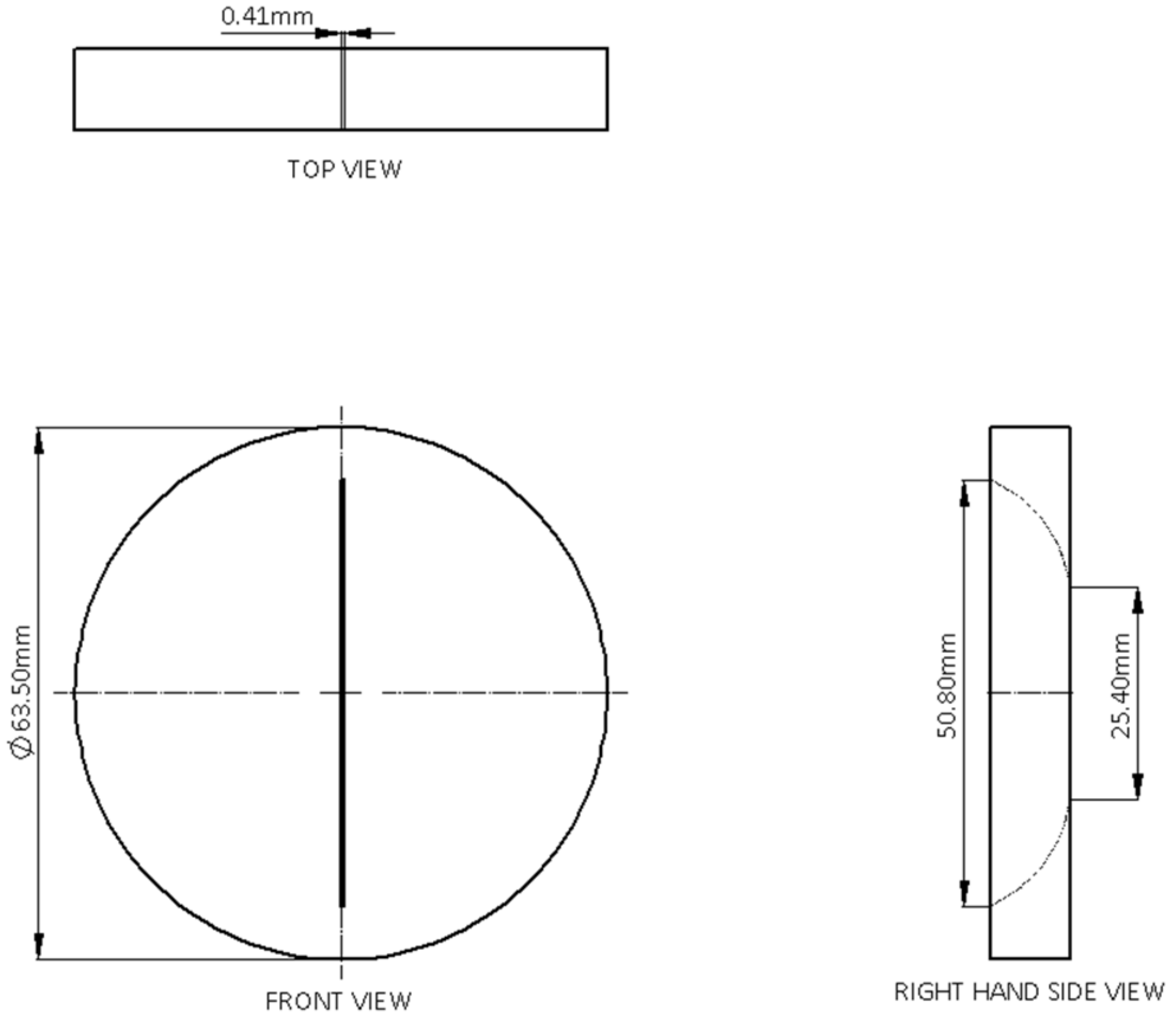

Figure 3.6 Orthographic view of the coupon with streamlined slot

Figure 3.6 is a representation of orthographic view of coupon and shows a scale view of the slot to the coupon. For the so-called 'streamlined slot' the inlet length is twice as long as exit length. The change in cross sectional area of the slot as shown in the RIGHT HAND SIDE VIEW is a result of the manufacturing process which used a plunging slitting saw. While the thickness and shape of the slot was varied, the scale and shape of the coupon was same.

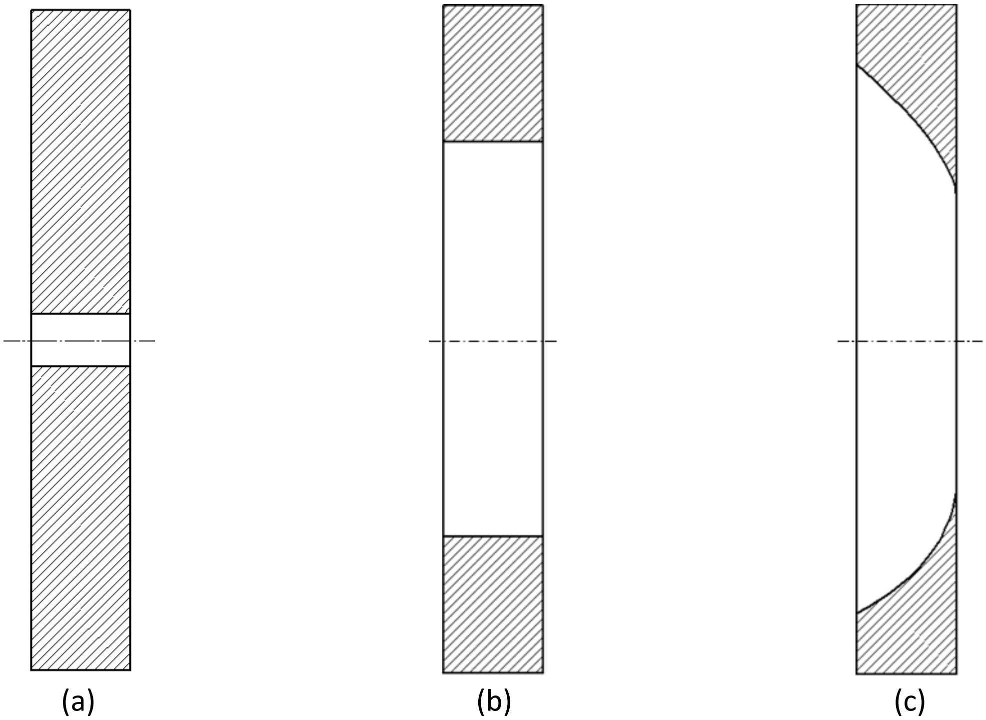

Figure 3.7 Cross sectional area for (a) circular slot (b) rectangular slot (c) streamlined slot

Figure 3.7 shows cross sectional view of the 3 different shapes of slot. For comparing different shape of slots cross sectional area across the flow was kept the same so that pressure loss can be measured for the same amount of fluid flow. Curvature is observed along the thickness for the streamlined slot which represents change in cross sectional are between entry and exit section of the slot. In this work all calculations were done based on the exit section of the slot. For rectangular and circular slot cross section was same throughout the thickness.

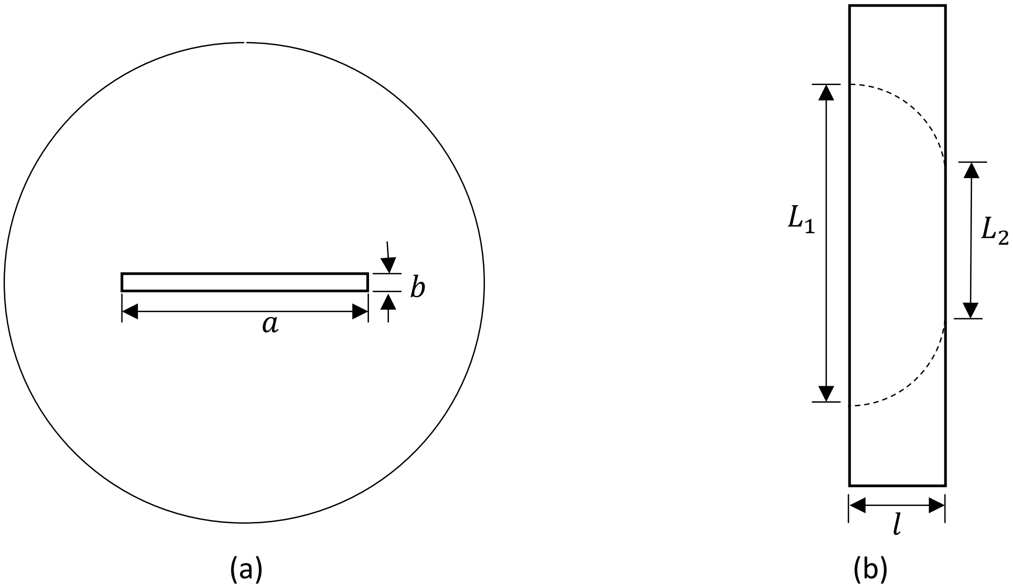

Figure 3.8 (a) Front view of rectangular slot coupon (b) side view of streamlined slot coupon

Figure 3.8 (a) shows the front view of rectangular slot coupon. Here, the slot length is defined by a and slot width is defined by b. These two parameters were varied to show the effect of aspect ratio $\left(AR_j = \frac{a}{b}\right)$ on pressure loss while cross sectional area was same for all the slots. Figure 3.8 (b) shows the side view of a streamlined slot coupon. This figure represents the inlet (L_1) and exit (L_2) length for streamlined slot. l is the thickness of the coupon. Hydraulic diameter $\left(D_h = \frac{4ab}{2(a+b)}\right)$ and all other calculations were done based on exit length scale ($a = L_2$) for the streamlined slot.

Table 3.1 Geometrical parameters for comparing different shapes of slots

Slot shape	Slot parameter	Cross sectional area (mm^2)	Diameter ratio (β)
Rectangular	a = 25.4, b = 0.5, l = 9.525	12.7	0.0105
Streamlined	a = L_2= 25.4, b = 0.5, L_1 = 50.8, l = 9.525	12.7	0.0105
Circular	d = 4	12.7	0.0525

Table 3.1 shows different geometrical parameter for comparison between 3 different shapes of slots. Specific set of slot length (a) and width (b) were selected to conduct the experiment for streamlined slot. These parameters and calculated parameters (A, D_h and β) are shown in Table 3.2. Slot parameters for rectangular slots are shown in Table 3.3 and Table 3.4. Each rectangular and circular slot would take on an average of 1 hr to manufacture including cutting the slot and calibrating the dimensions. The four sets of slots described in Table 3.1, Table 3.2, Table 3.3 and Table 3.4 were used to do the experiments. Each experiment for each slot took around 7 - 8 hr including preheating the test fluid before the experiment and cooling off the test fluid after the experiment.

Table 3.2 Different parameters for the streamlined slots

Slot width (b), mm	Slot length (a), mm	Cross sectional area(A), mm^2	Hydraulic diameter (D_h), mm	Diameter ratio (β)
0.41	25.4	10.414	0.81	0.0105
0.43	25.4	10.922	0.85	0.011
0.5	25.4	12.7	0.98	0.0128
0.53	25.4	13.462	1.04	0.0136
0.58	25.4	14.732	1.13	0.0149

Table 3.3 Parameters for rectangular slots with slot thickness l= 9.525 mm

a,Length (mm)	b,Width (mm)	Hydraulic diameter D_h (mm)	Area, A (mm^2)	Thickness, l (mm)	$TD = \frac{l}{D_h}$	$AR_j = \frac{a}{b}$	Diameter ratio, β
50.0	0.50	0.99	25	9.525	9.62	100.0	0.0130
47.5	0.53	1.04	25	9.525	9.15	90.3	0.0137
44.8	0.56	1.10	25	9.525	8.64	80.3	0.0145
43.5	0.57	1.13	25	9.525	8.40	75.7	0.0149
41.9	0.60	1.18	25	9.525	8.10	70.2	0.0154
38.8	0.64	1.27	25	9.525	7.51	60.2	0.0166
33.6	0.74	1.46	25	9.525	6.54	45.2	0.0191
27.5	0.91	1.76	25	9.525	5.41	30.3	0.0231
16.3	1.54	2.81	25	9.525	3.39	10.6	0.0369
5	5.00	5.00	25	9.525	1.91	1.0	0.0656

Table 3.4 Parameters for rectangular slots with slot thickness l= 6.35 mm

a,Length (mm)	b,Width (mm)	Hydraulic diameter D_h (mm)	Area, A (mm^2)	Thickness, l (mm)	$TD = \frac{l}{D_h}$	$AR_j = \frac{a}{b}$	Diameter ratio, β
50.0	0.50	0.99	25	6.35	6.41	100.0	0.0130
47.5	0.53	1.04	25	6.35	6.10	90.3	0.0137
44.8	0.56	1.10	25	6.35	5.76	80.3	0.0145
43.5	0.57	1.13	25	6.35	5.60	75.7	0.0149
41.9	0.60	1.18	25	6.35	5.40	70.2	0.0154
38.8	0.64	1.27	25	6.35	5.01	60.2	0.0166
33.6	0.74	1.46	25	6.35	4.36	45.2	0.0191
27.5	0.91	1.76	25	6.35	3.61	30.3	0.0231
16.3	1.54	2.81	25	6.35	2.26	10.6	0.0369
5	5.00	5.00	25	6.35	1.27	1.0	0.0656

3.2 Rheological model of the test fluid

Since the effect of pressure loss coefficient is different for Newtonian and non-Newtonian fluid it is important to classify the fluid being used in any experimental setup according to its rheological parameter. A double gap cylinder type rheometer (18318 RheolabQC, Anton Paar Inc.) was used to measure the effect of shear strain and stress on the test fluid with temperature. The temperature range for the flow cell was -20 °C - 80 °C. This could be operated manually or automatically for a range of conditions under computer control. Torque range for this device is 0.25 mNm - 75 mNm and the rotational speed range is 0.01 Hz - 1500 Hz.

A water bath (Julabo F12 ED, Julabo USA Inc.) was used in connection with rheometer to keep the temperature of test fluid constant. Temperature range of this water bath was -20 °C to 120 °C and it could be used for both cooling and heating.

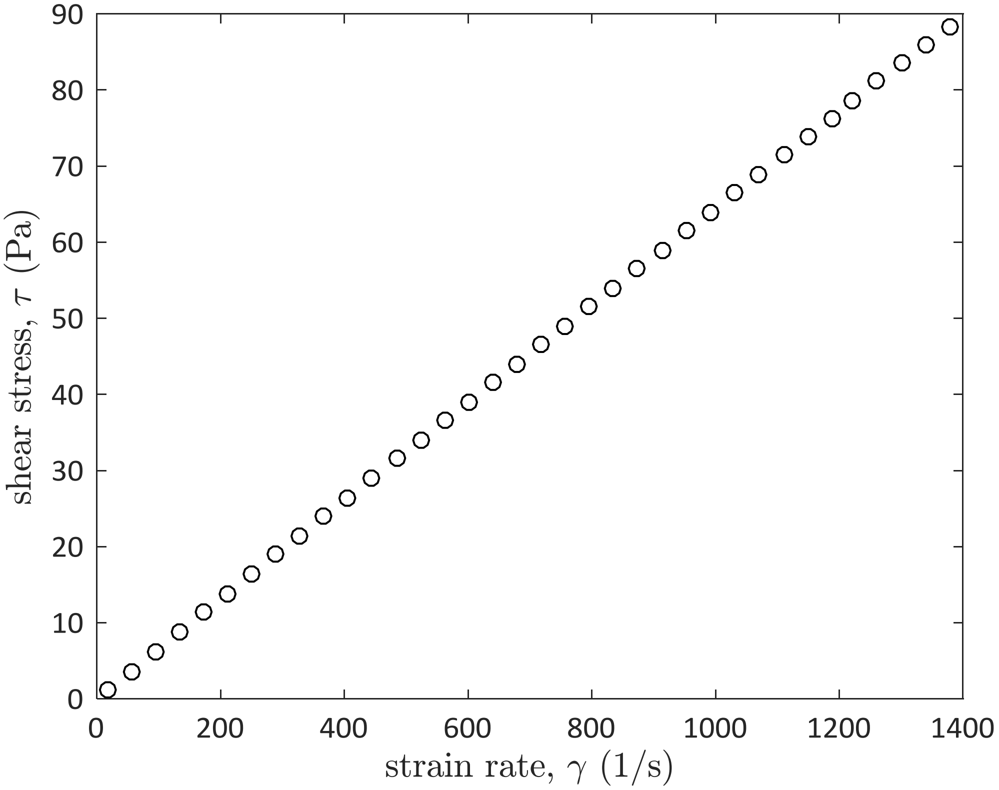

Figure 3.9 Plot of strain rate vs shear stress for test fluid at 75 °C

For the rheological modelling both temperature and shear rate was varied to determine the effect of shear rate for different temperatures. Figure 3.9 shows the shear rate (γ) and shear stress (τ) relation for experimental test fluid (BRIGHTSTOCK, MO1195, Fuchs Lubricants Canada Ltd.). This fluid is a thick motor oil which was selected for its similar properties of bitumen under the conditions found in SAGD operations. Shear rate (γ) was varied from 0 to 1,400 1/s in these test. The test fluid can be categorized as Newtonian fluid from the definition of a Newtonian fluid (Chapter 2) as there is a linear relation between shear rate (γ) and shear stress (τ).

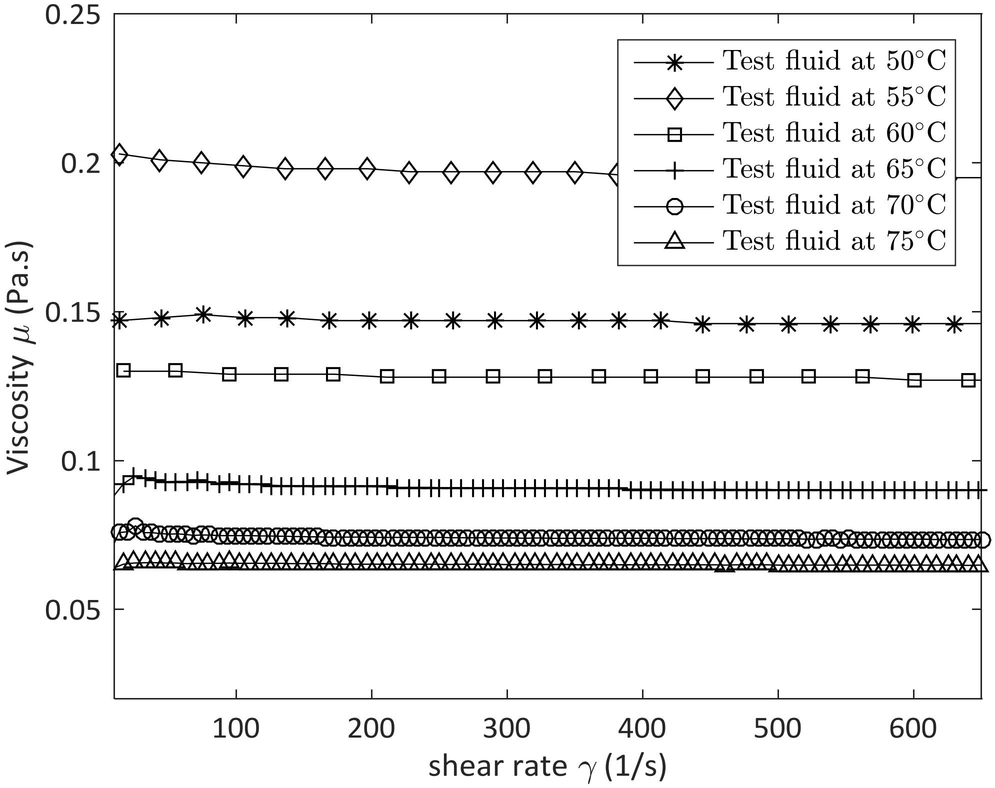

Figure 3.10 Viscosity of test fluid at different temperature and shear rate

Figure 3.10 shows the variation of viscosity of with temperature. Viscosity was measured at five different temperature (*T* = 50 °C, 55 °C, 60 °C, 65 °C, 70 °C, 75 °C) with a wide range of shear rate (0 - 700 1/s). From this figure it is evident that this fluid has a strong dependency on temperature. Within this temperature range the viscosity changes from 0.2 Pa.s to 0.06 Pa.s for 50 °C to 75 °C. For all temperatures, the viscosity does not change with shear rate. This confirms that this experimental fluid remains Newtonian for all the cases.

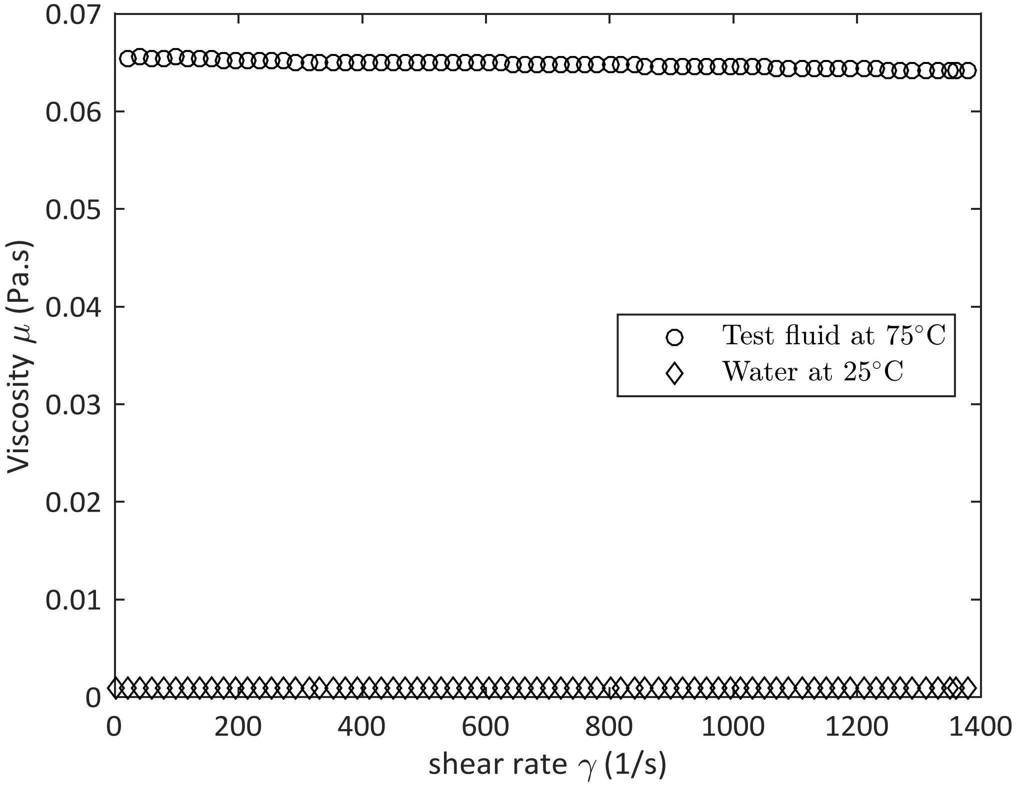

Figure 3.11 Comparison of viscosity between water and test fluid

Figure 3.11 shows the comparison of viscosity for water, μ_{water} = 0.0008 Pa.s at 25 °C and experimental test fluid, $\mu_{test\ fluid}$ = 0.065 Pa.s at 75 °C. It shows that both water and test fluids are Newtonian fluid. The test oil is a heavier fluid compared to water even at 75 °C. Since the test fluid's viscosity can be varied over a wide range with small temperature difference (T = 50 °C - 75 °C), it was chosen as the experimental fluid.

3.3 Experimental procedure

A predefined procedure was followed to undertake the experiments. The first step of this procedure was to preheat the test fluid. As shown in section 3.2 it is known that even at 50 °C the viscosity of the test fluid is 0.2 Pa.s. So, at room temperature it would be very hard to flow through the test loop pipe and other components. That is why the oil was preheated to a specific temperature (45 °C) using the second flow loop and heater. When preheating the large pump was used to circulate test fluid through the circulation pipe to make sure even temperature distribution in the fluid reservoir. This procedure was monitored through the DAQ and control system.

After achieving a desired temperature the test coupon was installed in the test section and in the main flow channel in top block. There were two air vents in main flow channel which were kept open to allow air purging. At the end of preheating the large pump was kept circulating the test fluid in the circulation pipe while small pump was used to pump the test fluid through flow meter into the flow channel, past the test section and back to reservoir. The outlet valve of the main flow channel was kept closed while main flow channel was filled using the small pump. Air vents were kept open until the whole flow channel (both upstream and downstream) was filled to remove air from the system. After completely filling the test section, the air vents were closed and outlet valve was opened.

After the preheating and priming of the system the feedback control system was turned on and set to a specified set of run conditions including pressure difference across the test section, initial and final temperature of the reservoir fluid, offset between top block and oil reservoir temperature to run an experiment. The heater was set to heat up the test fluid from initial to final temperature while the control system would keep constant pressure difference across the test section. Flow rate was monitored and would depend on the temperature and hence viscosity of the test fluid. During this experimental cycle, data was logged at 50 Hz in real time and all the necessary parameters were measured. The cycle was stopped when reservoir fluid reaches the final temperature. The same process was done for all types and shapes of coupon.

3.4 Data processing

The typical experiment setup described above was intended to measure some specific parameters. The control variables were fluid temperature (T), Pressure difference (ΔP) across the slot, slot geometry (a, b). The output variables were viscosity (μ), flow rate (Q). From these data non-dimensional parameters were defined and calculated.

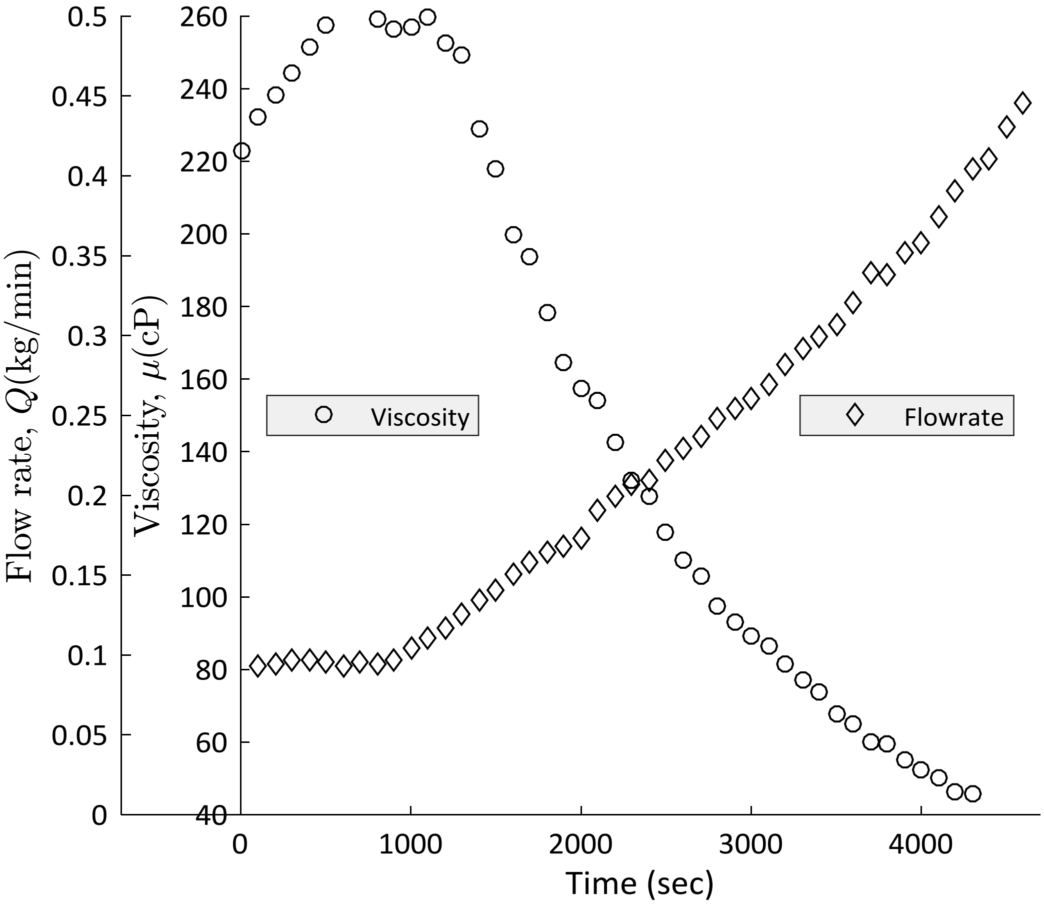

Figure 3.12 Experimentally measured viscosity and flow rate for different temperature

Figure 3.12 shows an example data set the experimentally measured viscosity and flow rate with the measured test fluid temperature from the fluid reservoir. One of the output variables was flow rate and the experiment was designed so that flow rate depends on viscosity of the fluid. From the figure it is confirmed that with increasing temperature of the test fluid in the reservoir viscosity decreases and with that, flow rate increases. A fluctuation or anomaly is visible for initial time for both parameters. This region indicates the time when flow channel was being filled up and total flow loop was not completely full.

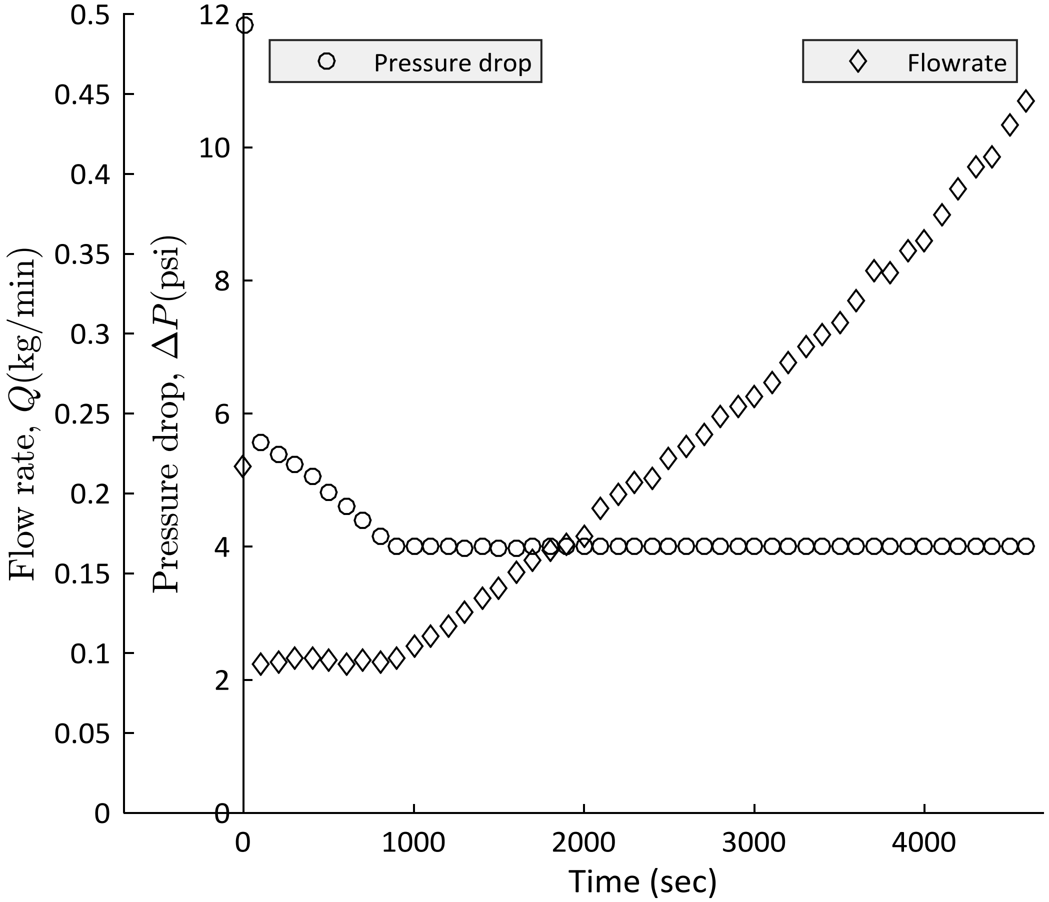

Figure 3.13 Experimentally measured pressure drop and flow rate for different viscosity

Figure 3.13 shows the characteristics of two important experimental data with time. One is the pressure difference across the slot (ΔP) and was one of the main controlled variables. For the whole experiment it was kept constant as 27580 Pa (4 psi). The flow channel takes some time (~900 sec) to be filled both upstream and downstream and this time is reflected on the figure where it shows the pressure difference is more than 4 psi. From the figure it also shows ΔP as a smooth line and no noise in the data was visible for the remainder of the experiment. The second parameter shown in the figure is the flow rate (Q) which was an output for this experiment and dependent on viscosity. It increased almost linearly. This figure also shows a time scale for running one typical experiment which includes ~900 sec to prime the system and ~3,400 sec for an experimental run from an initial temperature of 45 °C to 75 °C.

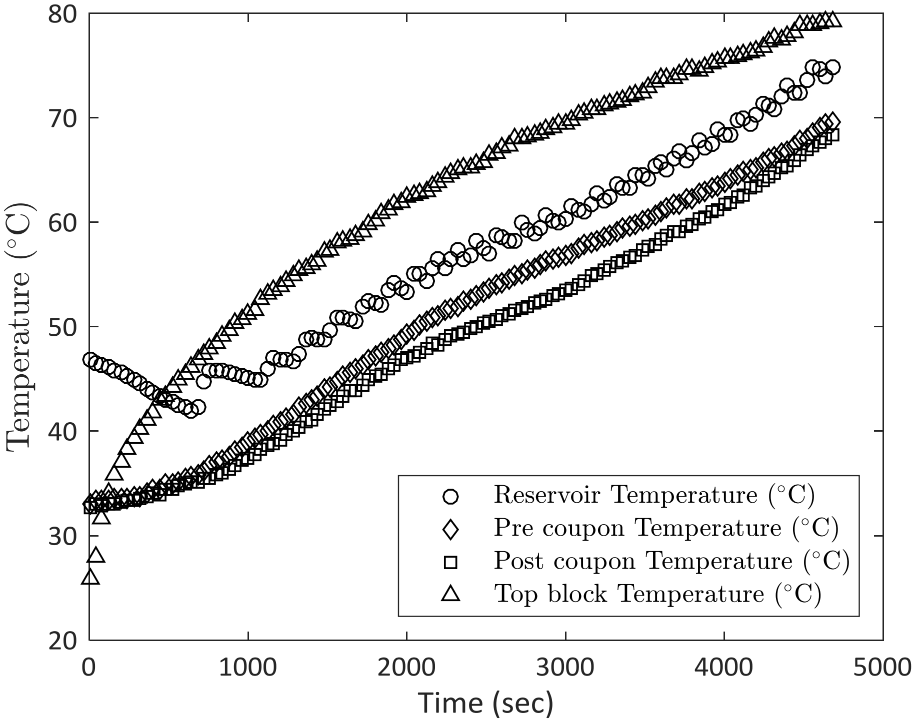

Figure 3.14 Temperature measurements at different position of the setup

Figure 3.14 shows temperature distribution at different positions in the experimental setup as a function of time. The top block of the experimental setup contained the whole test section and flow channel and it was insulated. Heated air was supplied to this block so that no heat loss can happen here. From the figure it is evident that the top block air temperature remained always at a higher temperature (10 °C offset) relative to the reservoir fluid temperature. Reservoir fluid was heated by a heater and it was controlled by a thermostat. After reaching temperature set point it was turned off and was turned on again when it crossed the offset value. This appears as a regular fluctuation in the temperature time series for the reservoir temperature. Parameters dependent on this temperature were therefore averaged within some specific temperature scale. Pre-coupon and post-coupon temperature was measured inside the flow channel and they were generally almost similar. Difference between reservoir temperature and pre coupon, post coupon temperature was within 2 °C. Over the time same trend for all the temperature line confirms that there was no stratification of oil in the reservoir.

From these measured data some non-dimensional parameters (defined in Chapter 1) were calculated to represent the results of the experiment. Sample calculations for determining these non-dimensional parameters are as follows-.

Table B.1(Appendix B) shows the data for rectangular slot whose dimensions are a = 0.05 m and b = 0.0005 m. Cross sectional area of the slot

$$\begin{aligned} A &= a \times b \\ &= 0.05\ \mathrm{m} \times 0.0005\ \mathrm{m} \\ &= 0.000025\ \mathrm{m}^2 \end{aligned}$$

Average slot inlet velocity can be calculated as:

$$
\begin{aligned}
u &= \frac{Q}{A \times \rho \times 60} \\
&= \frac{0.33264 \, \frac{\mathrm{kg}}{\mathrm{min}}}{0.000025 \ \mathrm{m}^2 \times 871.18 \, \frac{\mathrm{kg}}{\mathrm{m}^3} \times 60 \ \mathrm{sec}} \\
&= 0.255 \ \mathrm{ms}^{-1}
\end{aligned}
$$

Hydraulic diameter for this slot can be calculated as:

$$
\begin{aligned}
D_h &= \frac{4ab}{2(a+b)} \\
&= \frac{4 \times 0.05 \ \mathrm{m} \times 0.0005 \ \mathrm{m}}{2(0.05 \ \mathrm{m} + 0.0005 \ \mathrm{m})} \\
&= 0.00099 \ \mathrm{m}
\end{aligned}
$$

Reynolds number at this flow condition can be calculated as:

$$
\begin{aligned}
Re &= \frac{\rho u D_h}{\mu} \\
&= \frac{871.18 \, \frac{\mathrm{kg}}{\mathrm{m}^3} \times 0.255 \ \mathrm{ms}^{-1} \times 0.00099 \ \mathrm{m}}{194.2641 \ cP} \\
&= \frac{871.18 \, \frac{\mathrm{kg}}{\mathrm{m}^3} \times 0.255 \ \mathrm{ms}^{-1} \times 0.00099 \ \mathrm{m}}{194.2641 \ \times 0.001 \ \mathrm{Pa.s}} \\
&= 1.13
\end{aligned}
$$

Non-dimensional pressure drop for this condition can be calculated as:

$$\begin{aligned} P^* &= \frac{\Delta P}{\frac{1}{2}\rho u^2} \\ &= \frac{8.8756\ \mathrm{psi}}{0.5 \times 871.18\,\frac{\mathrm{kg}}{\mathrm{m}^3} \times (0.255\ \mathrm{ms}^{-1})^2} \\ &= \frac{8.8756\ \times 6894.75\ \mathrm{Pa}}{0.5 \times 871.18\,\frac{\mathrm{kg}}{\mathrm{m}^3} \times (0.255\ \mathrm{ms}^{-1})^2} \\ &= 2160.51 \end{aligned}$$

This sample calculation shows that Reynolds number and non-dimensional pressure drop are a strong function of density and viscosity and both these two parameters are a function of temperature. As Figure 3.14 shows that reservoir temperature was fluctuating so these fluid properties (density, viscosity) were averaged within the scale of ±0.5 °C for a specific temperature using custom processing code (MATLAB R2015b, The Mathworks Inc.).

3.5 Uncertainty analysis

Uncertainties of the non-dimensional parameters were calculated using a consecutive error propagation approach [40]. Reynolds number (Re) calculated here is a function of inlet velocity to the slot, hydraulic diameter (D_h), density (ρ) and viscosity (μ). But inlet velocity to the slot was calculated from flow rate (Q) and slot geometry (a, b) and density (ρ). So uncertainty for inlet velocity to the slot was first calculated taking slot geometry uncertainty as $\pm$ 0.0025 mm. Uncertainty for flow rate was ± 0.10 % and that of density was ± 0.5 $\mathrm{Kg/m^3}$. Both of these data were calculated from the specification of flow meter manufacturer. The uncertainty of the inlet velocity of the slot was calculated (Appendix A) as 4.45×10^{-6} m/s. Similarly, the hydraulic diameter was a function of slot geometry (a, b), the uncertainty in this parameter was calculated as (Appendix A) was 4.92×10^{-6} m. Uncertainty for the viscosity was specified as $\pm$ 1 % for $\mu > 10$ cP in the manufacturer's specification of the viscometer. From these data uncertainty for Reynolds number was calculated as $\pm$ 0.145 and that is $\pm$ 1.44 % for Re = 10.07 (Appendix A)

Similarly, non-dimensional pressure loss (P^*) is a function of pressure loss across the slot (ΔP), density (ρ) and inlet velocity to slot. From the specification of the pressure transducer it was found that uncertainty for measured pressure is 0.25 %. So, uncertainty for non-dimensional pressure loss was calculated as $\pm$ 0.414 and that is $\pm$ 0.126 % for P^* = 327.59 (Appendix A).

Chapter 4: Effect of slot shape, slot width and viscosity

This experiment was constructed to investigate the effect of slot geometry on the measured pressure drop by varying the slot geometry; aspect ratio (AR_j), slot shape, diameter ratio (β) and fluid property, viscosity (μ). The viscosity within the flow loop was varied by controlling temperature of the test fluid. During an experiment pressure drop across the slot was maintained at 27579 Pa (4 psi) while volume flow rate was measured for the fluid's temperature range of 50 °C – 75 °C. Results for different shapes are discussed within this temperature range followed by a comparison in between them. This experiment was carried out using the facility described in Chapter 3. The investigation will first consider pressure drop through the symmetrical streamline configuration used in the industry. Slots of rectangular geometry of then considered starting followed by the circular geometry.

4.1 Results for the streamlined slots

Pressure loss characteristics for the streamlined slot will be analyzed here using the normalized pressure loss parameter, P^*. This type of slot is mainly used in slotted liners in the SAGD operation as discussed in section 1.1. The particular shape is a result of the manufacturing process using a circular slitting saw which leads to the 'streamline' shape at the inlet of the slot. The same experimental procedure was followed for each slot with different slot width (b).

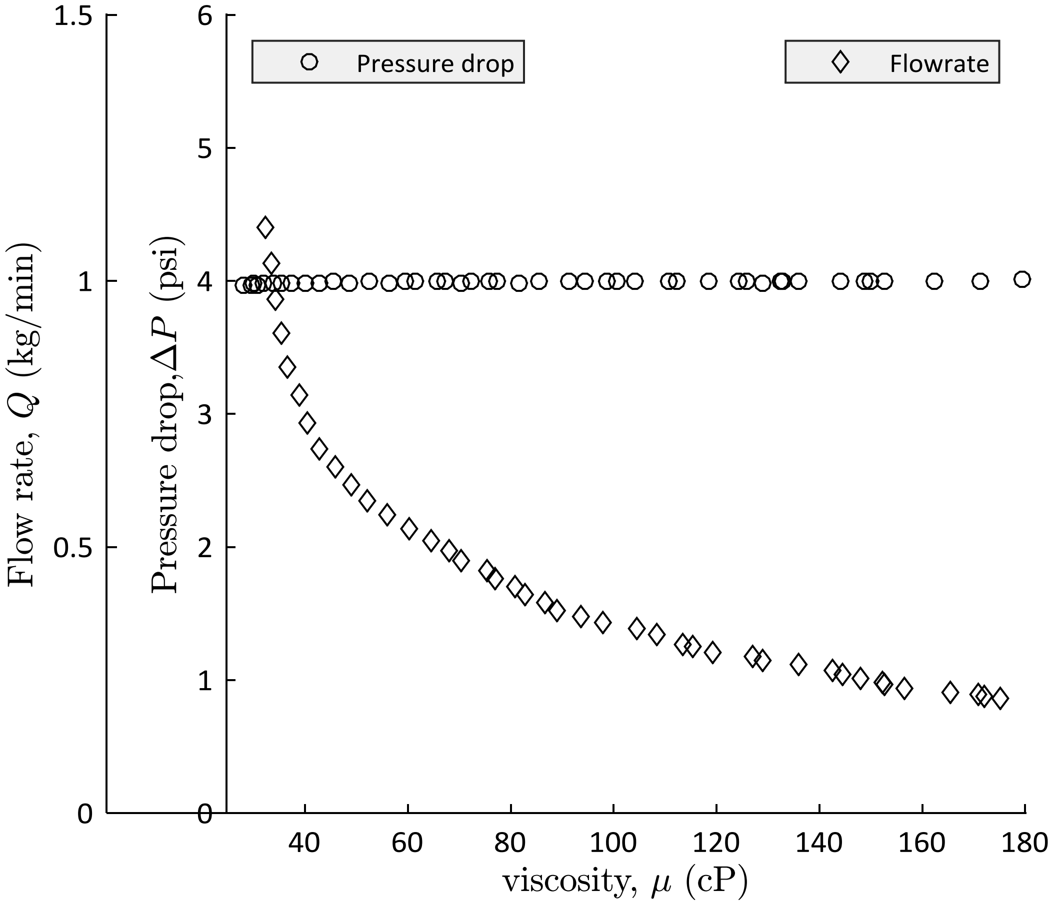

Figure 4.1 Plot of experimentally measured data for a streamlined slot

Figure 4.1 shows an example set of experimentally measured raw data for one single coupon with streamlined slot (a = 25.4 mm, b = 0.5 mm). As discussed in Chapter 3 pressure drop was one of the controlled variables. This figure shows that it was kept constant, ΔP = 4 psi. Flow rate (Q) was an output variable and a function of viscosity. From this figure it is evident that there is a non-linear relationship between flow rate (Q) and viscosity (μ). Here, flow rate can be represented as the kinetic energy and pressure drop can be represented as the energy associated with static pressure. From a standard application of Bernoulli's principle, a constant gap between these two was expected for any viscosity. But deviation from this principle is observed in Figure 4.1. This indicates that the viscosity has an effect on the pressure loss across the slot. Experimental results of other cases are shown in Appendix C.1.

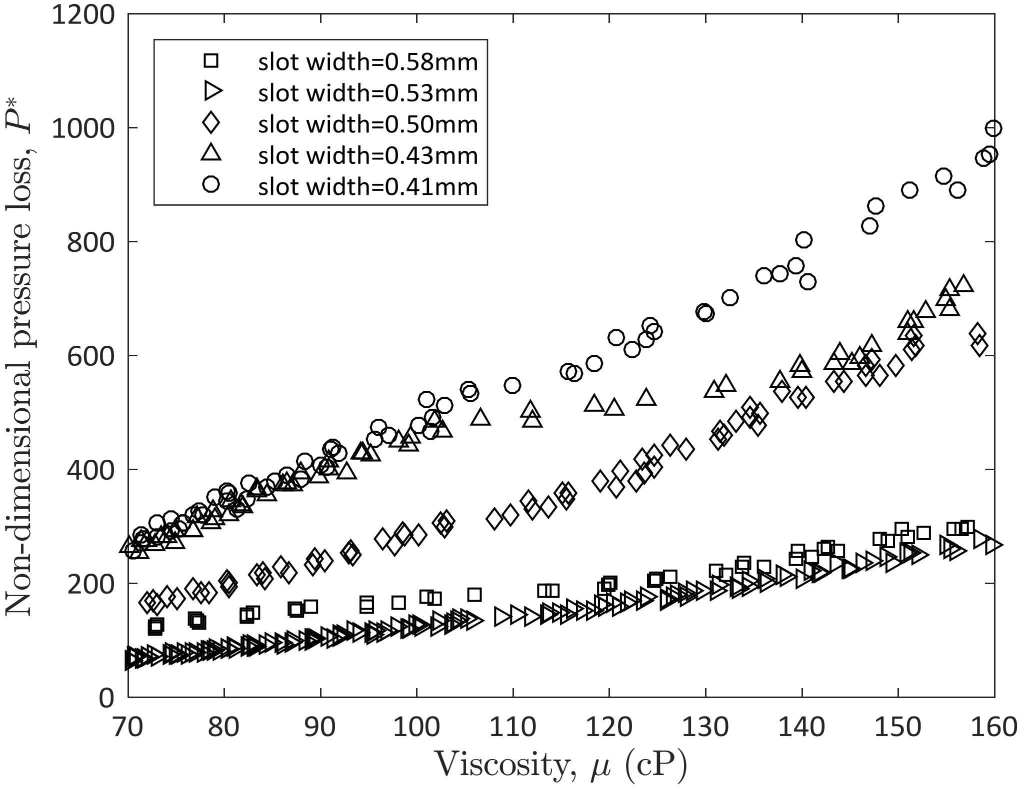

Figure 4.2 Plot of non-dimensional pressure loss for the streamlined slots with different slot width

The experimental data can be re-expressed as a non-dimensional pressure loss (P^*) using equation 1.5. Figure 4.2 shows non-dimensional pressure loss for different slot widths (b) but for same slot length (a = 25.4 mm). This figure shows that there is an increasing trend in non-dimensional pressure loss for any slot width with increasing viscosity. The figure shows that for any viscosity a narrower slot generally has a higher pressure loss. Also, for narrower slots the gradient change in $P*$ as a function of viscosity is higher. Effect of slot width (b) on pressure loss is prominent between minimum (b = 0.41 mm) and maximum (b = 0.58 mm) slot width. For low viscosity (μ = 70 cP), $P*$ is increased by a factor of $\sim$2 between slot width b = 0.41 mm and b = 0.58 mm and for high viscosity (μ = 158 cP) it is increased by a factor of $\sim$3. It should be noted that for a narrower slot the diameter ratio (β) decreases (from 0.0149 to 0.0105, Table 3.2) and also the contraction increases. An extra amount of energy is needed to overcome this contraction. That is why for a narrower slot pressure loss increases. Alvi et al. [17] reported the same trend for the range of diameter ratio (β) from 0.208 to 0.808. This loss is also higher for higher viscosity. That means that for a more viscous fluid, some extra amount of energy is needed to overcome that contraction factor. The effect of slot width between b = 0.58 mm and b = 0.53 mm is not effective because for this two slots slot width decreases only by 8.62 %.

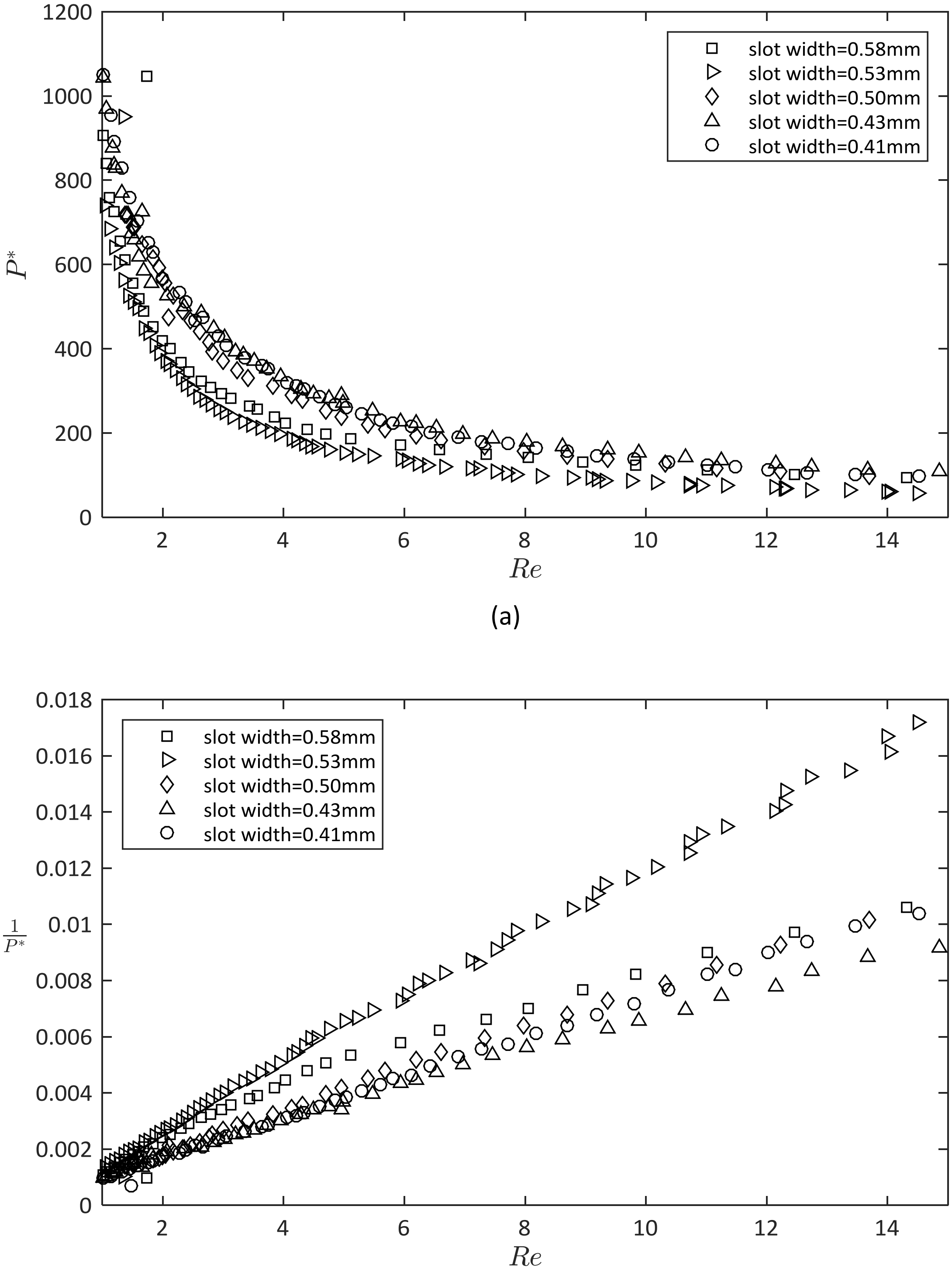

(a)

(b)

Figure 4.3 (a) Plot of non-dimensional pressure loss vs Reynolds number and (b) plot of inverse of non-dimensional pressure loss vs Reynolds number for different slot widths of the streamlined slot

Figure 4.3(a) shows the variation of non-dimensional pressure loss with Reynolds number. It shows that for a streamlined slot and for different slot width, the pressure loss characteristics follow the standard trend line for low Reynolds numbers. For $Re < 15$ it shows that with increasing Reynolds number the pressure loss decreases with an exponential decay. At very low Reynolds number the effect of slot width on pressure loss is strong but at high Reynolds number ($Re > 8$) effect of slot width is not prominent. The literature [17] indicates that a constant pressure loss is apparent at a much higher Reynolds numbers of $Re \sim 100$ and for β in the range of 0.2 - 0.8. But from the current data shown in the figure (Figure 4.3 (a)) it is observed that pressure loss starts to assume a constant value for Reynolds number as low as Re = 10 with the diameter ratio β = 0.015 - 0.0105.

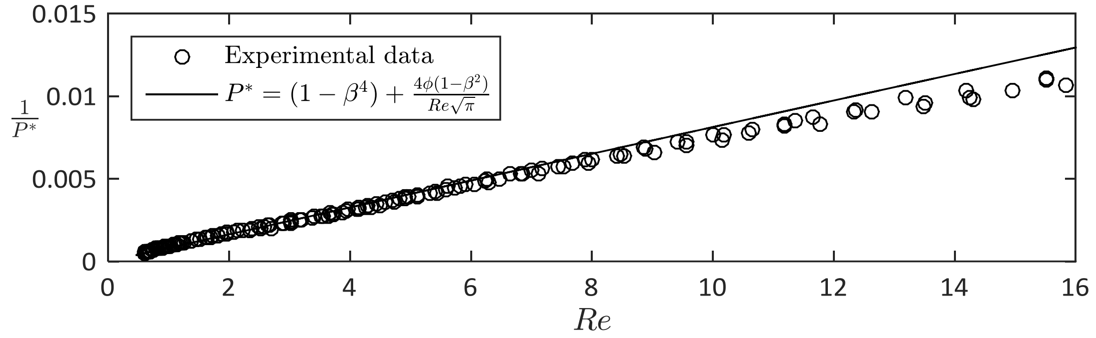
0.015
0.01
0.005
0
$\frac{1}{P^*}$
Experimental data
$P^* = (1-\beta^4) + \frac{4\phi(1-\beta^2)}{Re\sqrt{\pi}}$
0
2
4
6
8
10
12
14
16
Re

(a)

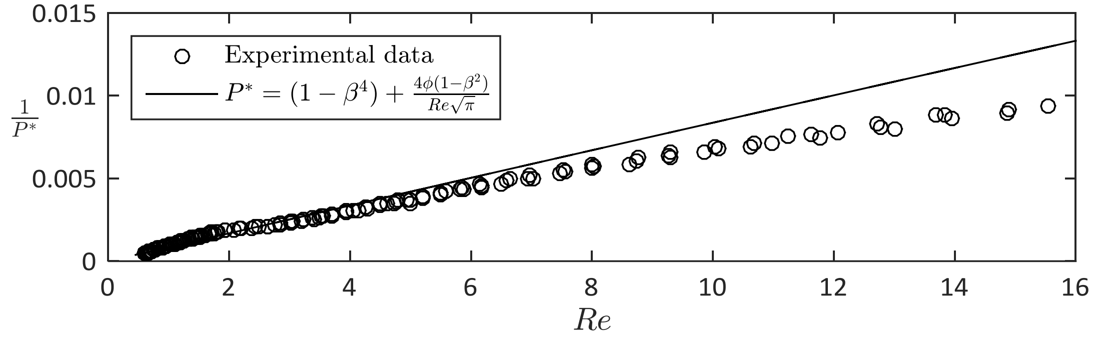
0.015
0.01
0.005
0
$\frac{1}{P^*}$
Experimental data
$P^* = (1-\beta^4) + \frac{4\phi(1-\beta^2)}{Re\sqrt{\pi}}$
0
2
4
6
8
10
12
14
16
Re

(b)

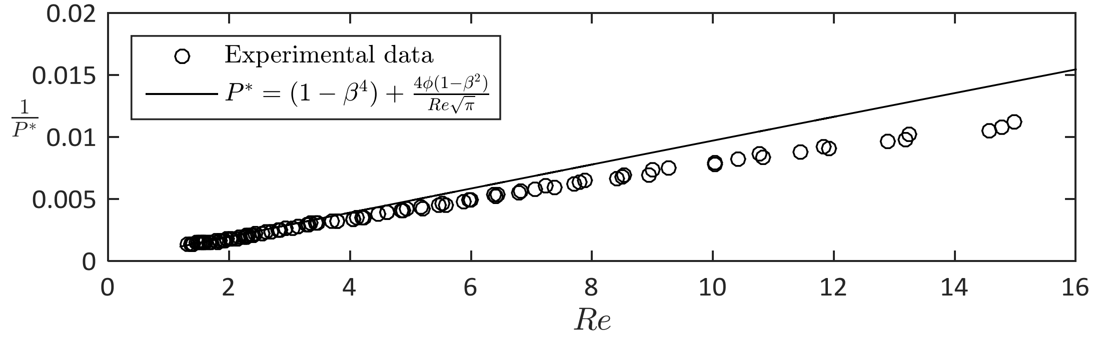
0.02
0.015
0.01
0.005
0
$\frac{1}{P^*}$
Experimental data
$P^* = (1-\beta^4) + \frac{4\phi(1-\beta^2)}{Re\sqrt{\pi}}$
0
2
4
6
8
10
12
14
16
Re

(c)

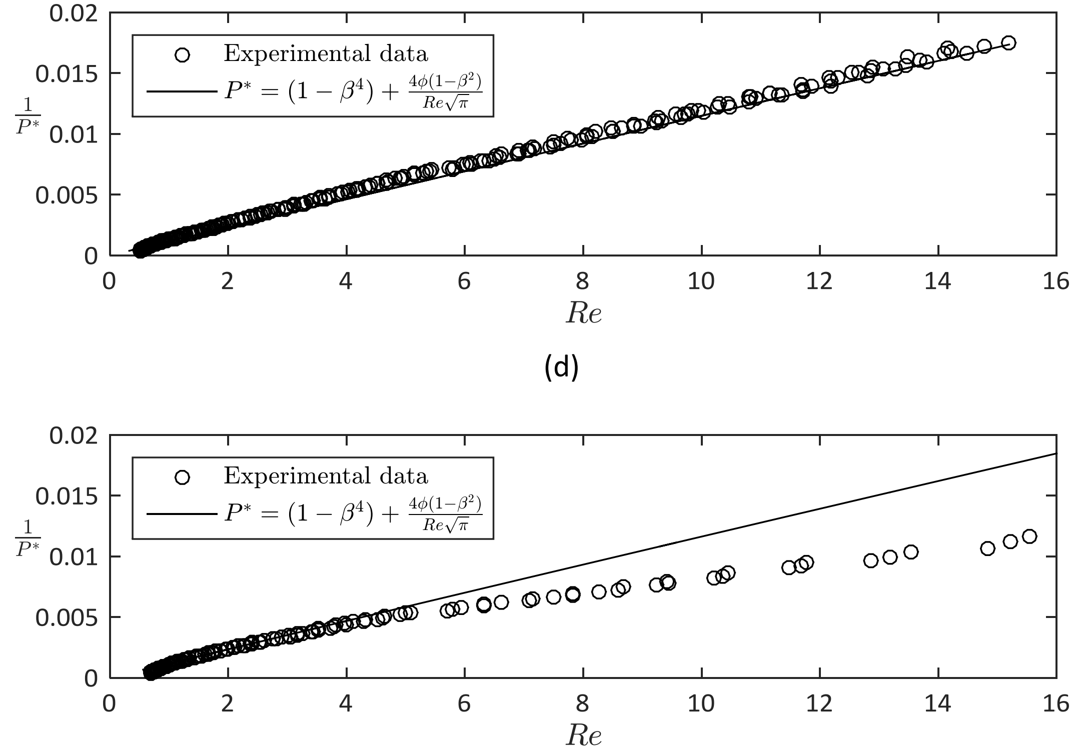

(d)

(e)

Figure 4.4 Plot of comparison between theoretical model and experimental data for streamlined slots with slot width (a) 0.41 mm, (b) 0.43 mm, (c) 0.50 mm, (d) 0.53 mm and (e) 0.58 mm

Figure 4.4 shows the comparison of experimental data for the streamlined slots with theoretical model developed in Chapter 2. The theoretical model was fitted with experimental data for each slot using nonlinear least square method (Matlab 2015a, Mathwork Inc.) and empirical factor ϕ was calculated. The trend in the data is same for all the slots (b = 0.41 mm, 0.43 mm, 0.50 mm, 0.53 mm and 0.58 mm); with increasing Reynolds number, pressure loss decreases or, $\frac{1}{P^*}$ increases. Figure 4.4 shows that the theoretical model is in good agreement with the experimental data for $Re \leq 8$ for all the slots except for slot width b = 0.58 mm. A difference is observed between theoretical model and experimental data for high Reynolds number ($Re > 8$). This shows that the theoretical model might not be accurate for high Reynolds number. The analytical model does depend on a constant empirical factor (ϕ). This factor (ϕ) controls the convergence of flow streamlines (defined in Chapter 2) from upstream into the contraction area. So this factor would largely depend on diameter ratio, β. The factor (ϕ) was calculated using a non-linear least square curve fitting method for different slot width.

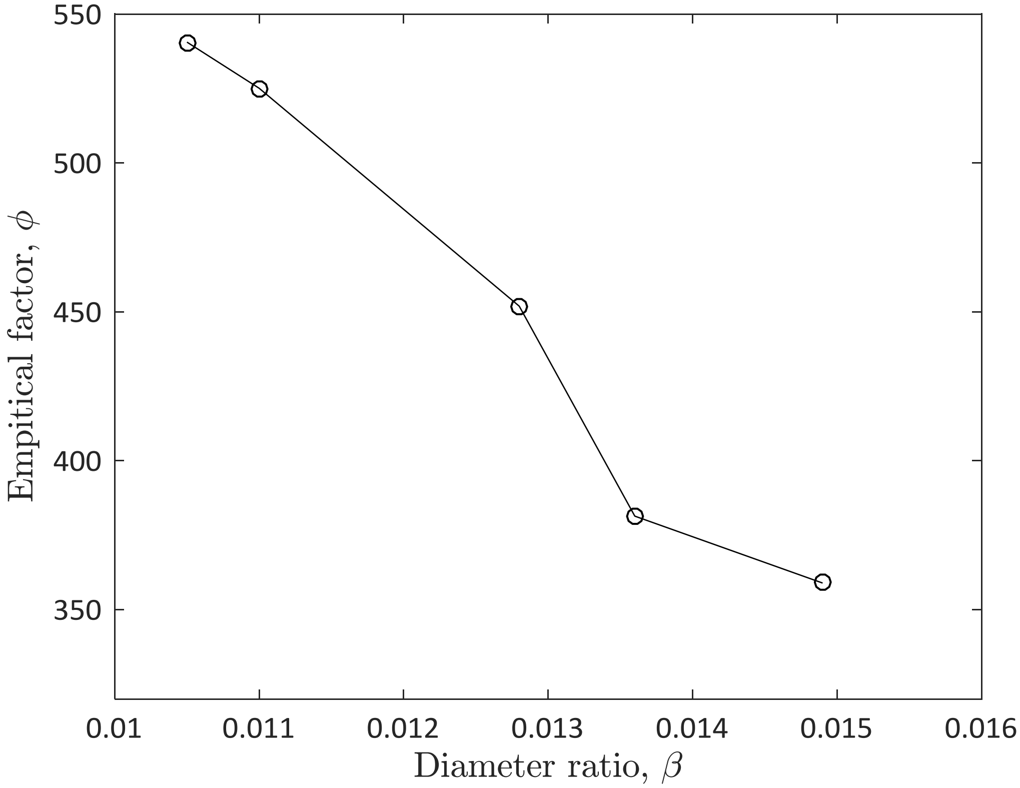

Figure 4.5 Plot of empirical factor (ϕ) vs diameter ratio (β)

Figure 4.5 shows the plot of the calculated empirical factor (ϕ) for different diameter ratios. This result indicates that with increasing diameter ratio (β), the empirical factor (ϕ) decreases almost linearly. With increasing diameter ratio the slot becomes wider and streamlines converge smoothly from the main flow channel to the slot. This is shown as a decrease in the empirical factor, ϕ.

4.2 Results for the rectangular slot

To understand the influence of changing the geometry from streamlined to rectangular an experiment was conducted with a same cross sectional area (A) of the streamlined (a = 25.4 mm, b = 0.50 mm) and the rectangular slot. Pressure loss characteristic for varying viscosity and hence Reynolds number for the rectangular slot will be discussed here.

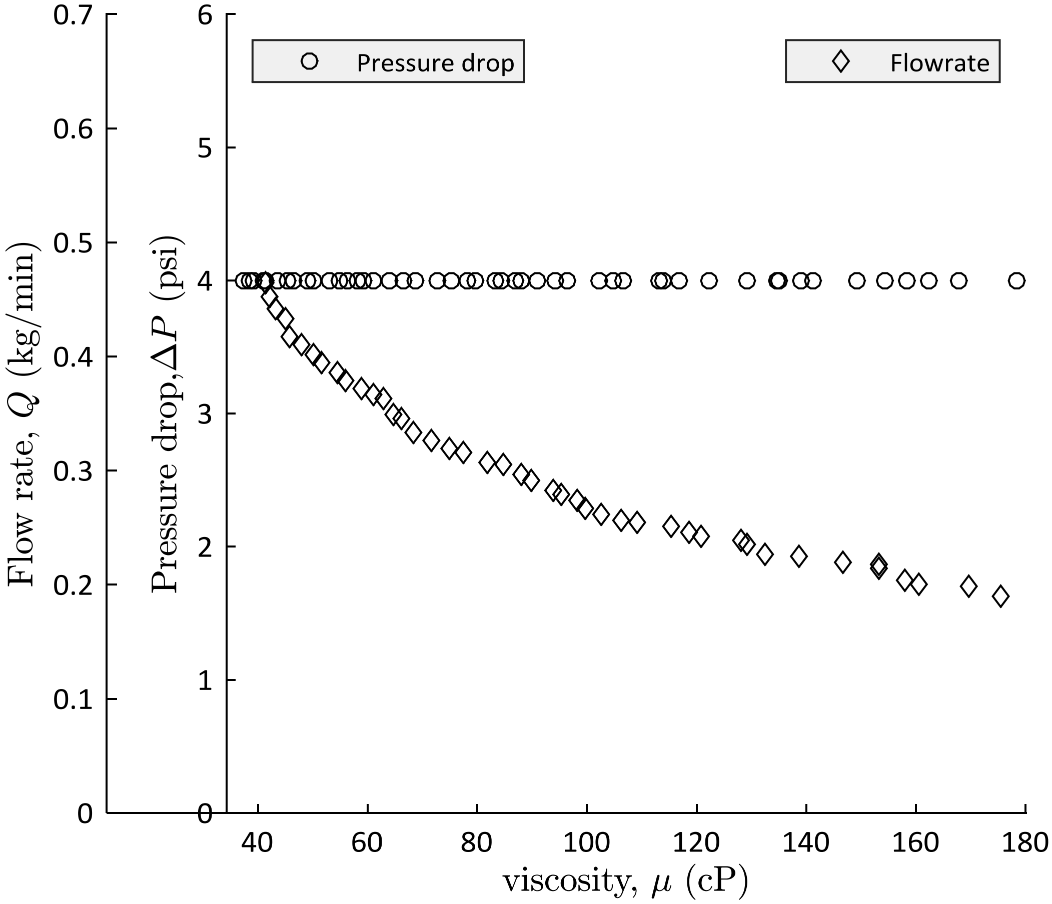

Figure 4.6 Plot of experimentally measured data for a rectangular slot (a = 25.4 mm, b = 0.50 mm)

Figure 4.6 shows experimentally measured flow rate (Q) and pressure drop (ΔP) with varying viscosity (μ) for a rectangular slot (a = 25.4 mm, b = 0.50 mm). This figure confirms that experiment for rectangular slot followed the same procedure as of streamlined slots. Pressure drop was kept constant throughout the experiment (ΔP = 4 psi) and flow rate (Q) was measured which increased with decreasing viscosity (μ) as expected.

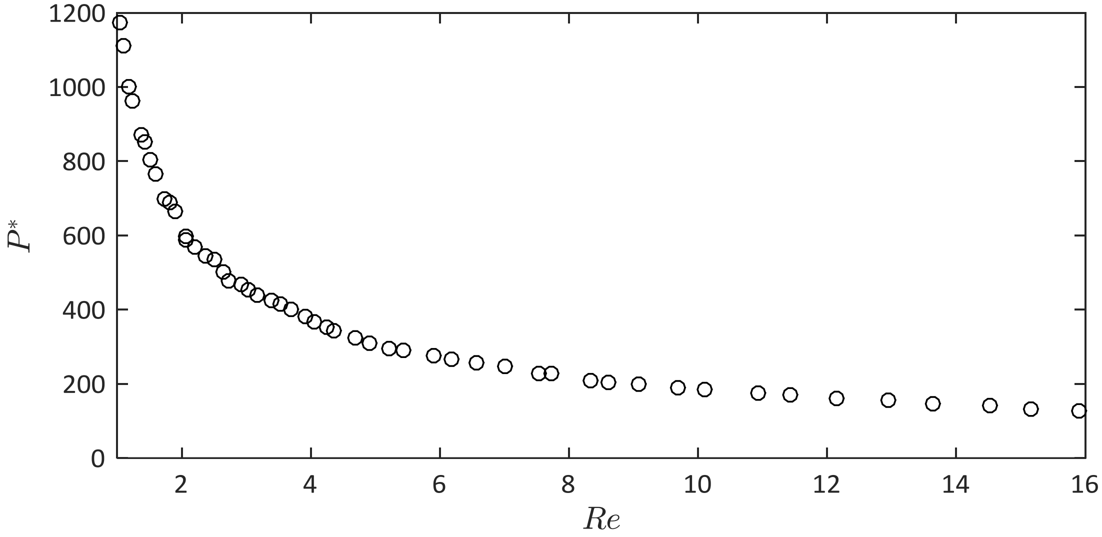

(a)

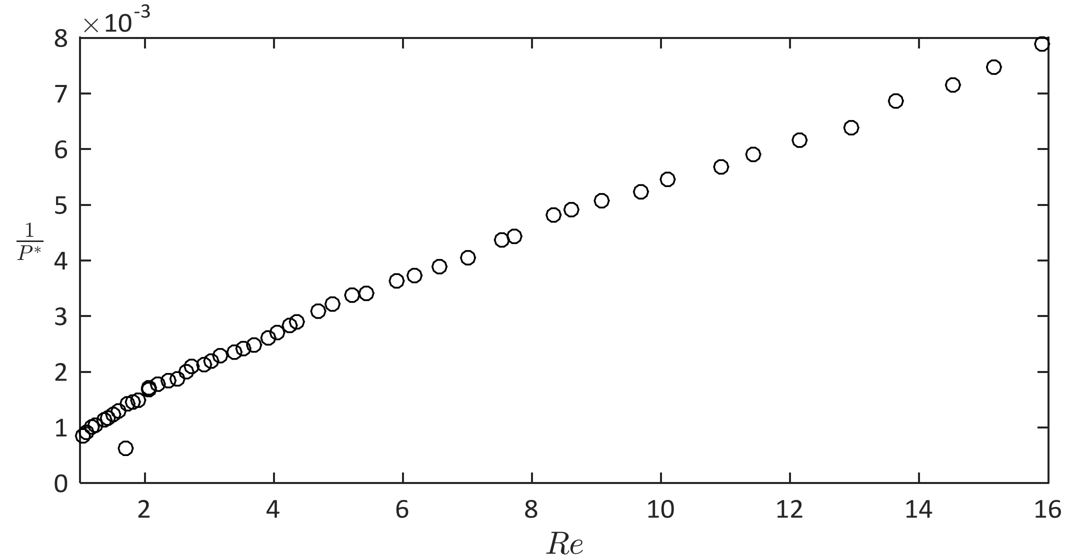

(b)

Figure 4.7 (a) Plot of non-dimensional pressure loss vs Reynolds number and (b) plot of inverse of non-dimensional pressure loss vs Reynolds number for a rectangular slot

Non-dimensional pressure loss (P^*) and Reynolds number (Re) are calculated using equation 1.5 and equation 1.1 respectively. Figure 4.7(a) shows the variation of non-dimensional pressure loss with Reynolds number. As discussed in the previous section, for a rectangular slot P^* also decreases with increasing Reynolds number for $Re < 16$.

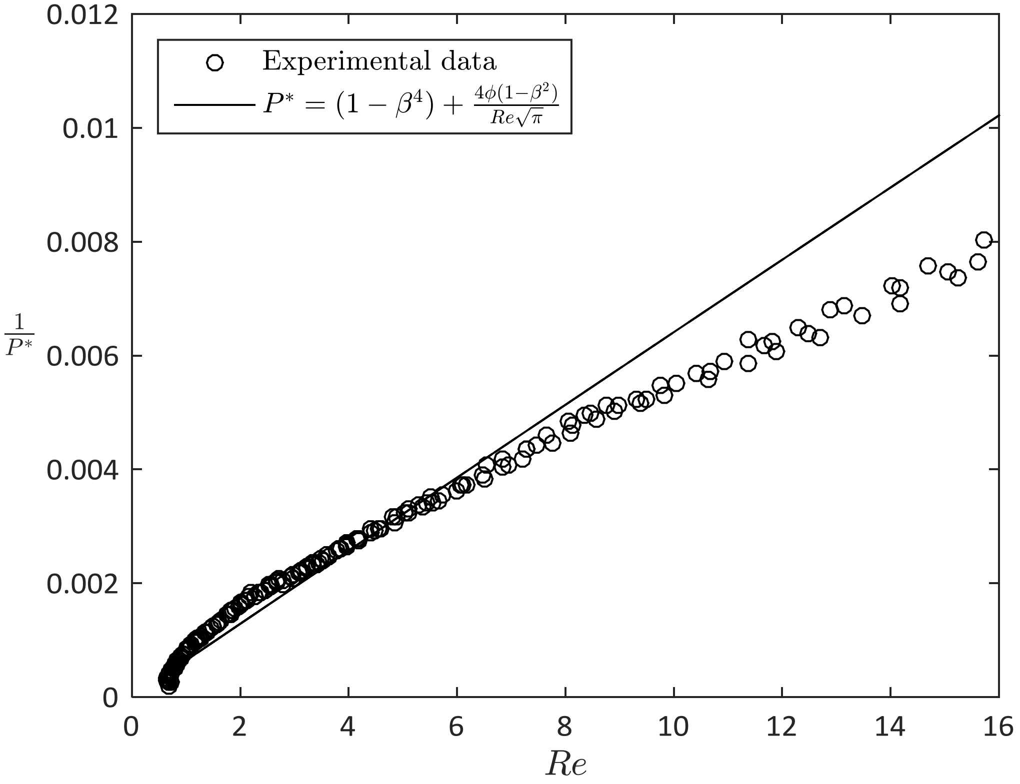

Figure 4.8 Comparison for the theoretical model with the experimental data for a rectangular slot

Figure 4.8 shows the comparison between experimental data and theoretical model for rectangular slot. The figure shows a good agreement between experimental data and theoretical model for $Re \leq 8$. This shows that the theoretical model works well for predicting pressure loss for low range of Reynolds number. For this fit, the empirical factor ϕ was calculated to be 686.84. For the same diameter ratio (β = 0.0128) streamlined slot, the empirical factor was calculated to be ϕ = 451.92. This indicates that the empirical factor ϕ is also a function of slot shape. For the streamlined slot, lower value of ϕ represents that less convergence is required for this kind of slots to allow the flow through the contraction region.

4.3 Results for the circular slot

To evaluate pressure loss characteristics of rectangular and streamlined slot an experiment was conducted with geometry of a circular slot (d = 4 mm, β = 0.073) with the same cross sectional area as the rectangular and the streamlined slot. Following the same procedure data was collected for this configuration.

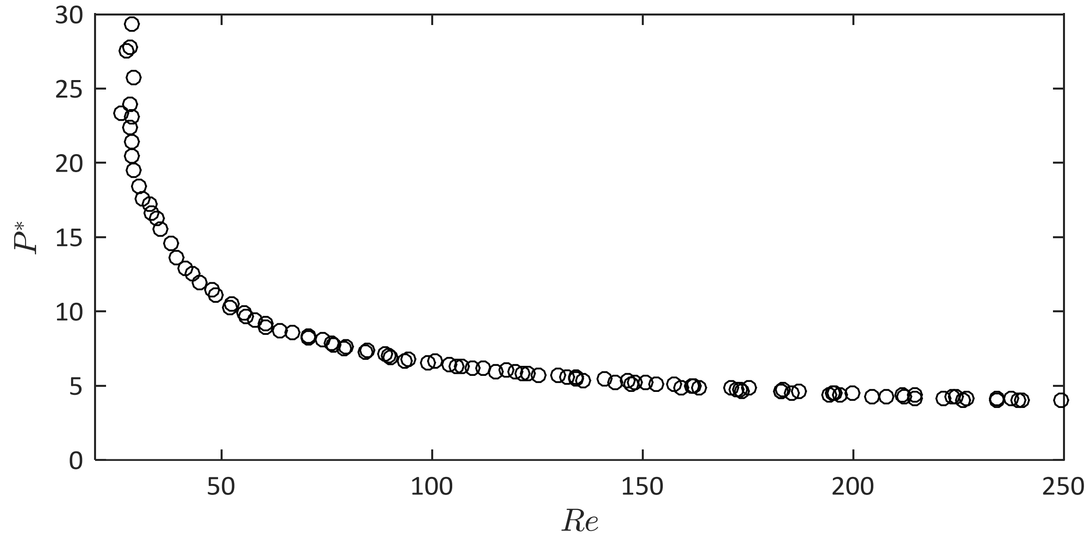

(a)

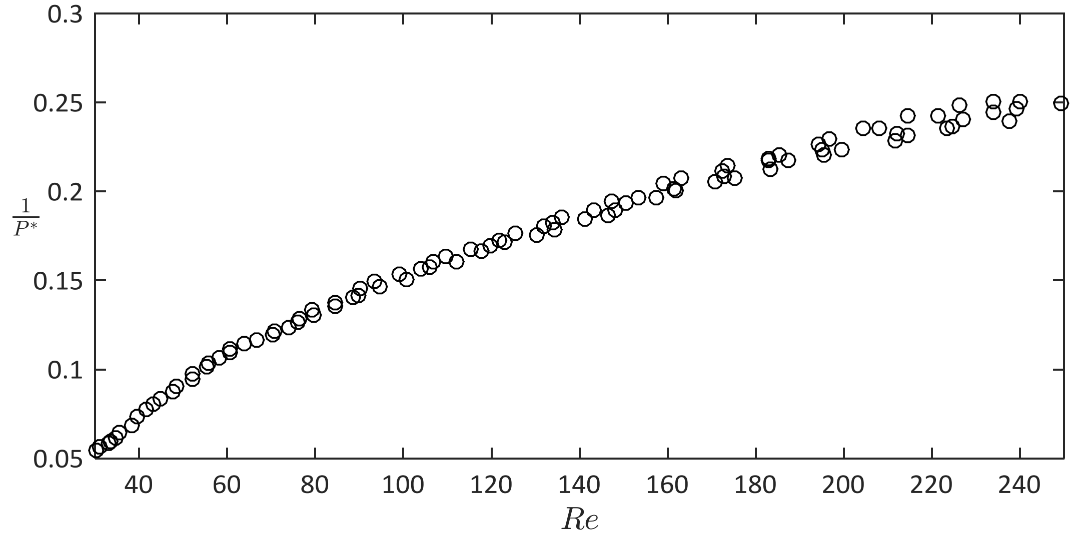

(b)

Figure 4.9 (a) Plot of non-dimensional pressure loss vs Reynolds number and (b) plot of inverse of non-dimensional pressure loss vs Reynolds number for a circular slot

Figure 4.9 (a) shows the variation of P^* with Reynolds number. Here, the viscous force is normalized as Reynolds number. It shows that at low Reynolds number the viscous force is predominant and P^* decreases with increased Reynolds number.

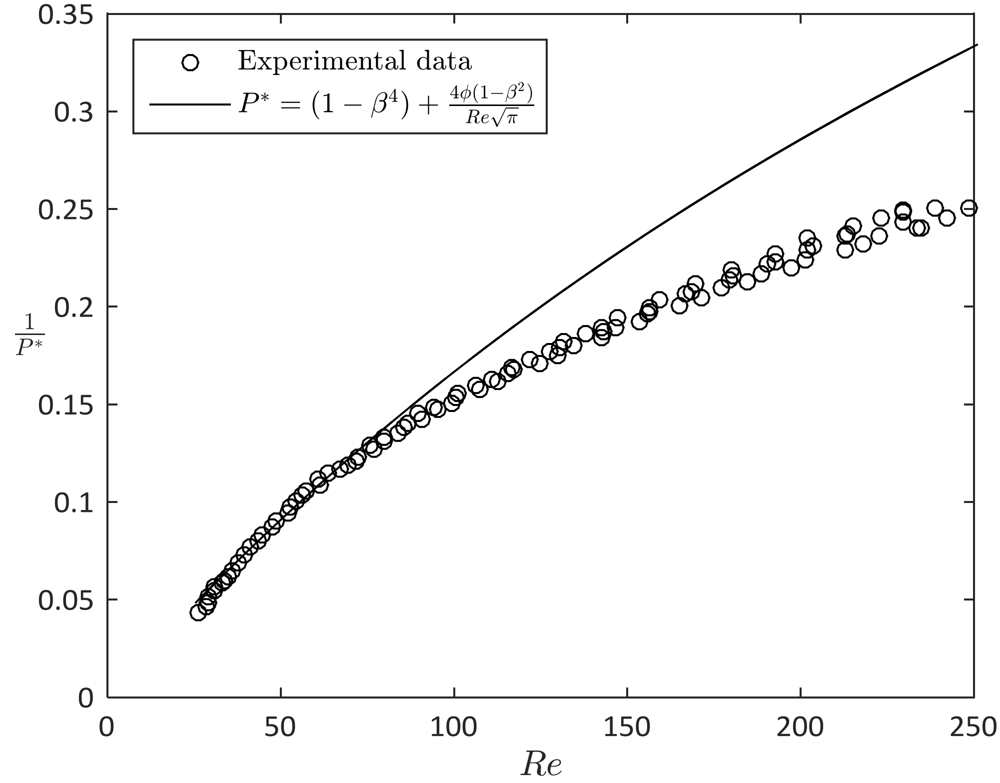

Figure 4.10 Comparison of the theoretical model with the experimental data for a circular slot

Figure 4.10 shows the comparison between the experimental data and the theoretical model for non-dimensional pressure loss. This figure confirms that the theoretical model only works for lower range of Reynolds number. Operating range of Reynolds number for circular slot was high ($20 < Re < 250$) than that of rectangular and streamlined slot ($1 < Re < 16$). Due to this high operating range of Reynolds number experimental data for the circular slot does not fit well with the theoretical model. Still, the trend for both data is the same, with increasing Reynolds number, P^* decreases ($\frac{1}{P^*}$ increases). For the circular slot ($\beta = 0.073$) the empirical factor was calculated as ϕ = 243.7 using a non-linear least square curve fitting method with the experimental data.

4.4 Comparison between different slot shapes

As for all three shapes of slots; streamlined, rectangular and circular similar trends and characteristics are evident, a comparison between them would give a better understanding about their properties and performance.

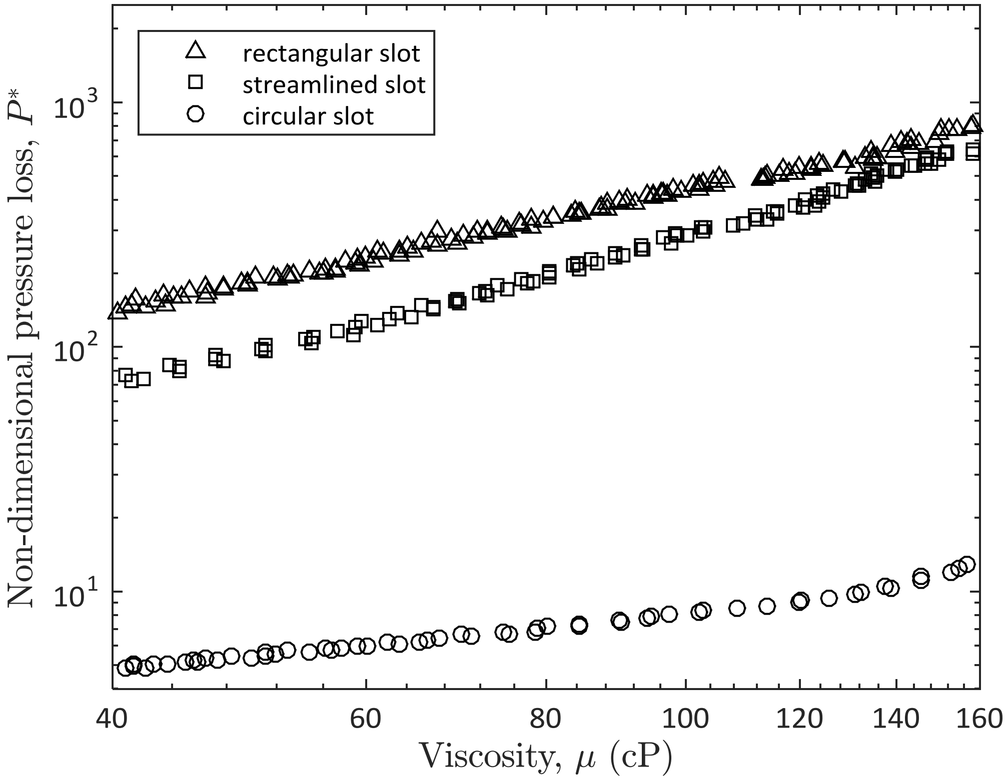

Figure 4.11 Comparison of non-dimensional pressure loss between circular, rectangular and streamlined slot

Figure 4.11 shows the comparison of non-dimensional pressure loss with respect to viscosity. The cross sectional area (A = 12.7 mm^2) was the same for all the slots to allow the only change to be the geometry of the slot. For each shape, P^* increases with increasing viscosity. For the same cross sectional area P^* is significantly higher for the rectangular and streamlined slot rather than the circular slot. This change can be attributed to the difference in diameter ratio $\left(\beta = \frac{D_h}{D}\right)$ for these slots. For circular slot diameter ratio was β = 0.073, which was ~5.7 times higher than that of rectangular and streamlined slot (β = 0.0128). For low values of β the contraction causes the flow to change abruptly in forward direction creating higher pressure loss. The same characteristic was also reported in previous work [17]. Non-dimensional pressure loss, P^* is almost the same for rectangular and streamlined slot at higher viscosity values and at lower viscosity values the rectangular slot experiences higher pressure loss. One interpretation is that the streamlined slot converges flow more smoothly than the rectangle one causing less pressure loss.

From these results it can be concluded that pressure loss is a function of viscosity of the fluid and the diameter ratio (β) of the geometry. The shape factor for the streamlined, rectangular, and circular and slot width (b) factor have also been analyzed here. For the narrower streamlined slot (b = 0.41 mm) pressure loss was highest than the other ones. For all three shapes of slots pressure loss was observed to decrease with increasing Reynolds number. Comparison with theoretical model also shows the same trend.

Chapter 5: Effect of aspect ratio and thickness to diameter ratio for the rectangular slots

One of the objectives of this work was to investigate the effect of high aspect ratio (AR_j) on pressure loss characteristics at low Reynolds numbers. The effect of aspect ratio (AR_j) on pressure loss characteristic for the rectangular slots is discussed here. Length (a) and width (b) of the rectangular slot was varied while keeping the cross sectional area (A) constant. Starting with a square slot ($a = b$), the aspect ratio was changed gradually from 1 - 100 with 10 different slots to generate different configurations of the rectangular slot. Two sets (10 slots in each set) of rectangular slot were used with two different coupon thicknesses. Results for coupon thickness l = 9.525 mm will be discussed first followed by the results of coupon thickness l = 6.35 mm. Effect of thickness to diameter ratio $\left(TD = \frac{l}{D_h}\right)$ will also be analyzed here.

5.1 Results for slot thickness l = 9.525 mm

Results of slot thickness l = 9.525 mm will be discussed here. Effect of aspect ratio (AR_j) will be the main focus. Pressure loss characteristics at different temperature and aspect ratio will be then compared. 10 different slots were used for this set of experiments covering the range of aspect ratio (AR_j) from 1 - 100 for this slot thickness (l = 9.525 mm).

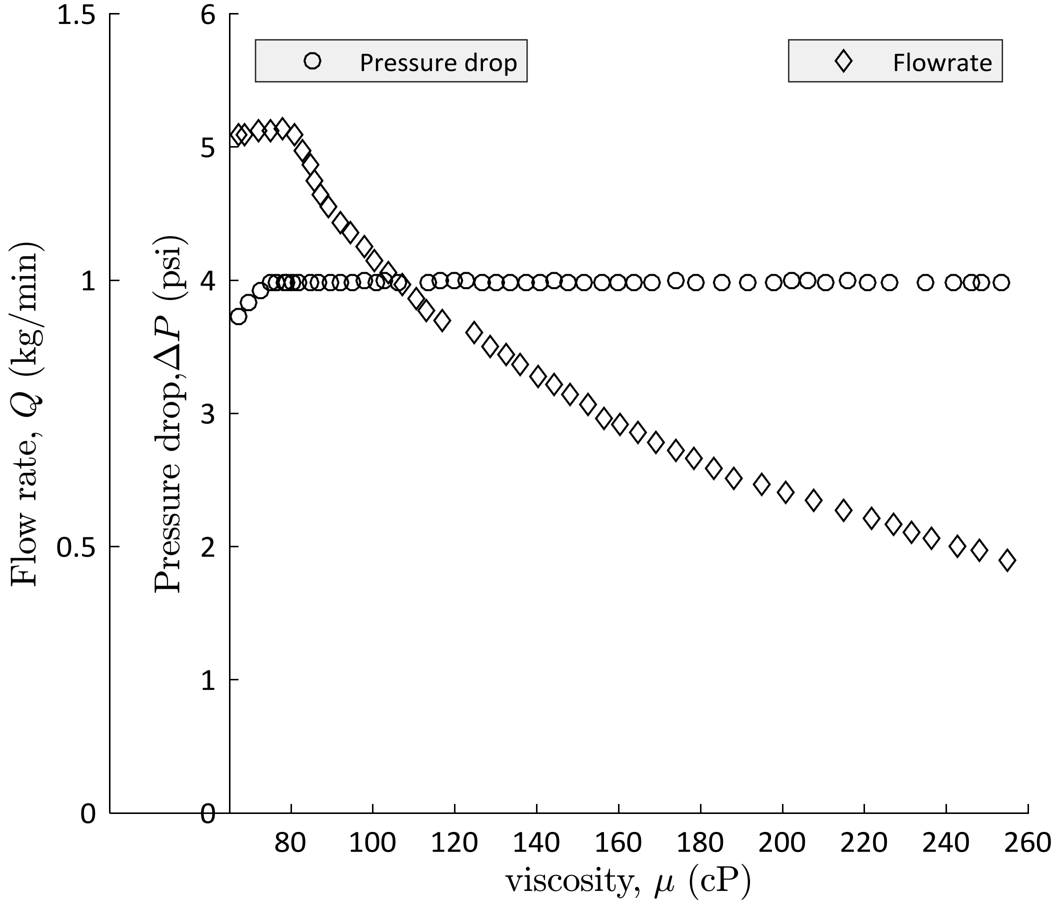

Figure 5.1 Plot of experimentally measured data for a rectangular slot (a = 50 mm, b = 0.50 mm, l = 9.525 mm)

Figure 5.1 shows the experimentally measured pressure drop and flow rate for a single coupon with rectangular slot (a = 50 mm, b = 0.5 mm) and thickness of the slot was, l = 9.525 mm. This figure is an example data set collected using the same experimental procedure documented in Section 3.3. Figures showing experimental data for all other slots are shown in the Appendix C.2 for reference. From these measured data non-dimensional pressure loss (P^*) was calculated using equation 1.5 and aspect ratio (AR_j) using equation 1.3 for all the slots.

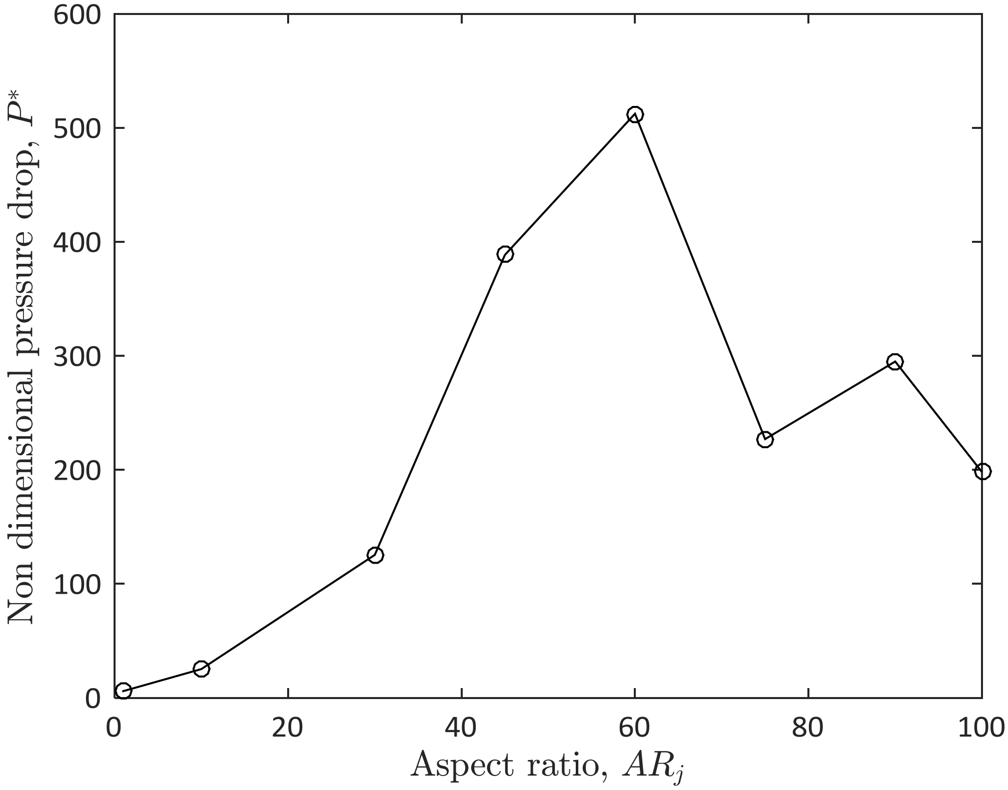

Figure 5.2 Plot of non-dimensional pressure loss for l = 9.525 mm at T = 60 °C

Figure 5.2 shows the variation of P^* for coupon thickness $l = 9.525$ mm and pressure loss as calculated at temperature T = 60 °C. One single data point in this figure represents one experiment with one slot which required about 1.5 hr of experimental time. Each experiment was conducted within the temperature range of 50 °C - 75 °C. Figure 5.2 shows calculated P^* for only T = 60 °C. With increasing aspect ratio (AR_j) the slot becomes narrower which also decreases diameter ratio (β). This is apparent as an increasing trend of pressure loss is observed with increased aspect ratio ($AR_j \leq 60$). After AR_j = 60 some deviation is observed in the trend. For the rectangular slot with aspect ratio AR_j = 75 a sudden drop in P^* is observed. There is also a general decrease in P^* for $AR_j > 60$. To identify if this is an experimental error and to confirm the repeatability of experimental data the experiments were repeated for aspect ratio AR_j = 75 and 90.

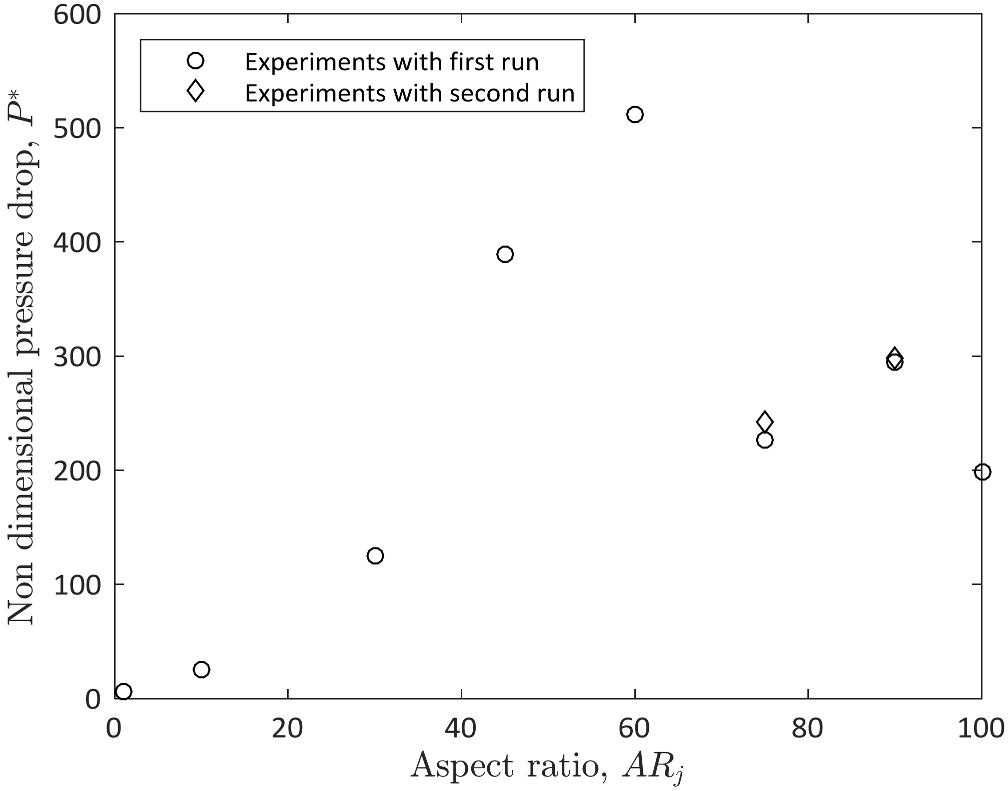

Figure 5.3 Plot of data repeatability test for AR_j = 75 and 90

Figure 5.3 shows non-dimensional pressure loss for varying aspect ratio with repeated data for aspect ratio AR_j = 75 and 90. The figure confirms that the following the same experimental procedures the data are repeatable. The difference between first and second run for aspect ratio AR_j = 75 is 6.69 % and for aspect ratio AR_j = 90 is 1.35 %. These data also confirms a sudden change in non-dimensional pressure drop for aspect ratio AR_j = 75. Another approach was undertaken to encompass the deviation by adding two more data points in the vicinity of aspect ratio AR_j = 75. The new data points chosen were aspect ratio AR_j = 70 and 80.

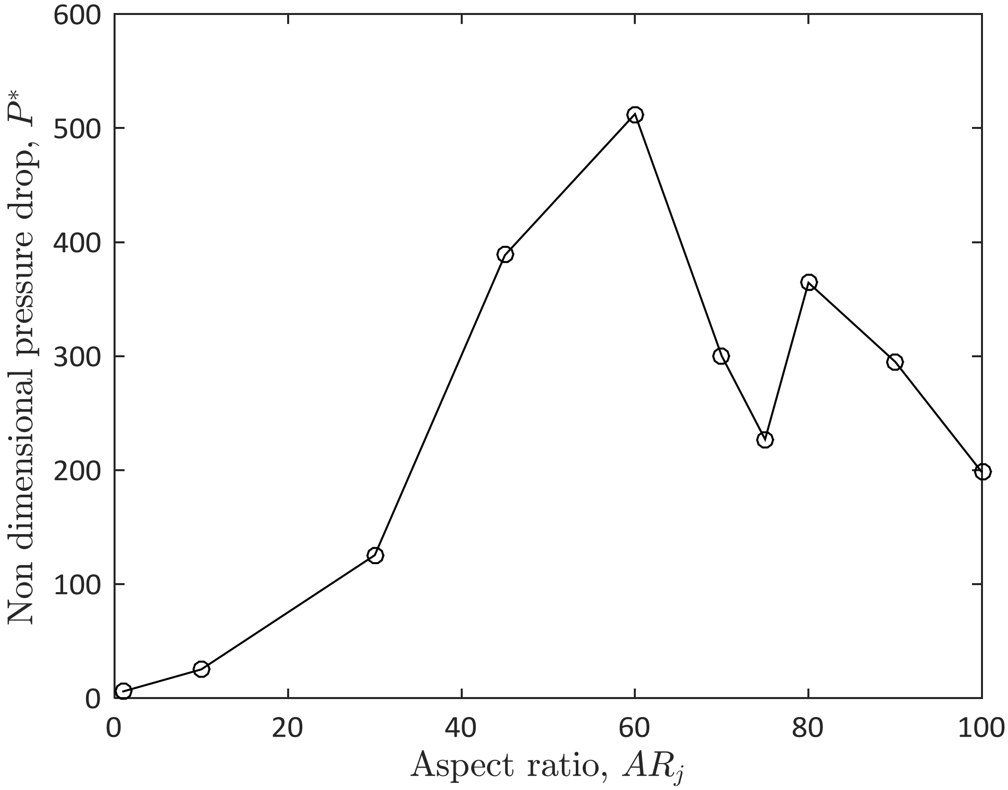

Figure 5.4 Plot of non-dimensional pressure loss for $l = 9.525$ mm with additional data points at AR_j= 70 and 80

Figure 5.4 shows non-dimensional pressure loss for slot thickness l = 9.525 mm at T = 60 °C with two additional data points (AR_j = 70 and 80). These data points confirm a definite drop in P^* at AR_j=75. $AR_j = 60$ can be characterized as a critical aspect ratio after which some other phenomenon are potentially present that affect the flow, such as axis switching or instable jet flow. Although past researchers [32] did not observe any instable behaviour of jet with $Re \leq 100$ but their aspect ratio was very low (AR_j~5). With higher aspect ratio (AR_j) the slot becomes narrower with increased length. So the flow does not converge uniformly along all directions for all configurations of slots. Due to these characteristics deviation from normal trend in pressure loss is observed here.

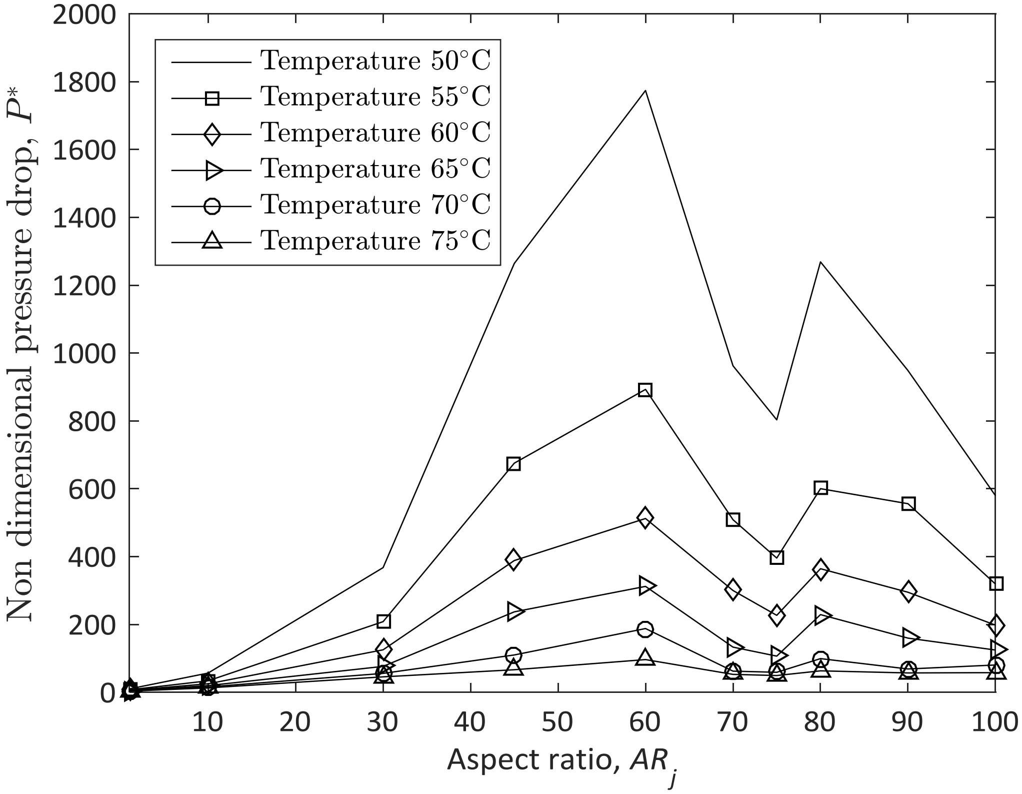

Figure 5.5 Plot of non-dimensional pressure loss for l = 9.525 mm at different temperature

Figure 5.5 shows variation of non-dimensional pressure loss with varying aspect ratio (AR_j = 1 - 100) for different temperatures. It shows that for all temperatures, P^* increases with increasing aspect ratio for $AR_j > 60$. Diameter ratio (β) changes from 0.012 to 0.065 (Table 3.3) for high to low aspect ratio slots. So, less contraction is experienced by the fluid flow at low aspect ratio and hence less shear deformation. That is why at a low aspect ratios (AR_j) temperature effect is not predominant. At high temperature viscosity reduces and Reynolds number increases. With increasing Reynolds number pressure loss in the system approaches a a constant value. That is why less fluctuation of pressure loss is observed at higher temperatures with varying aspect ratio. Within the range of temperature (50 °C - 75 °C) deviation from normal trend is observed for $AR_j > 60$ for every temperature measurement.

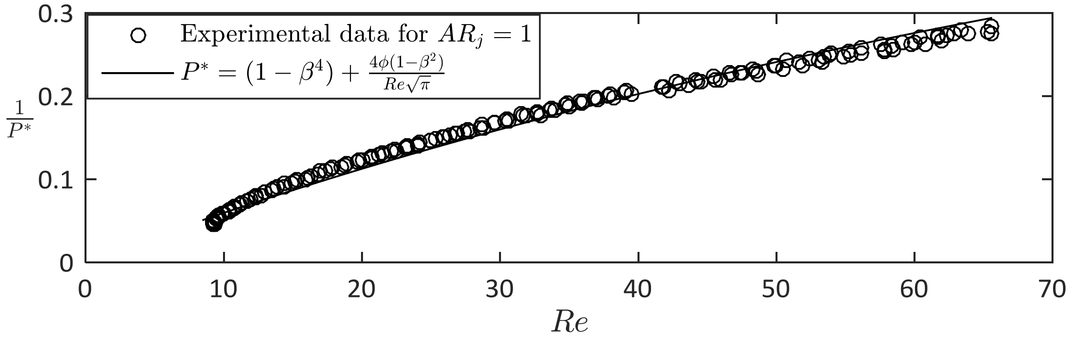

(a)

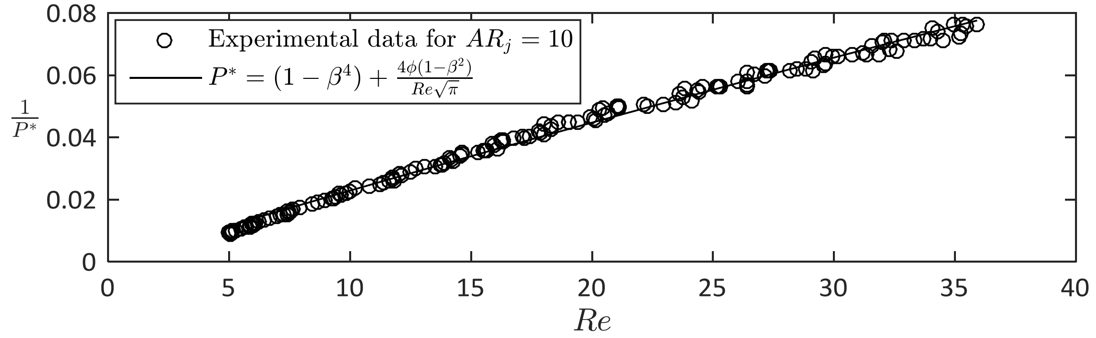

(b)

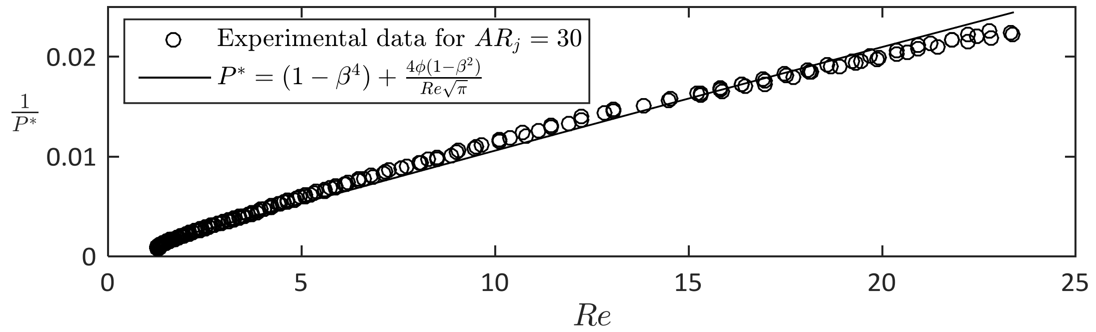

(c)

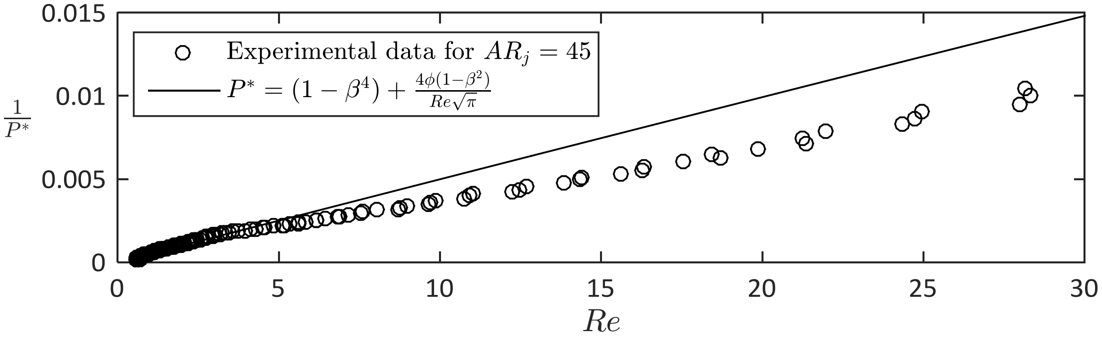
0.015
0.01
0.005
0
$\frac{1}{P^*}$
Experimental data for $AR_j = 45$
$P^* = (1-\beta^4) + \frac{4\phi(1-\beta^2)}{Re\sqrt{\pi}}$
0
5
10
15
20
25
30
Re

(d)

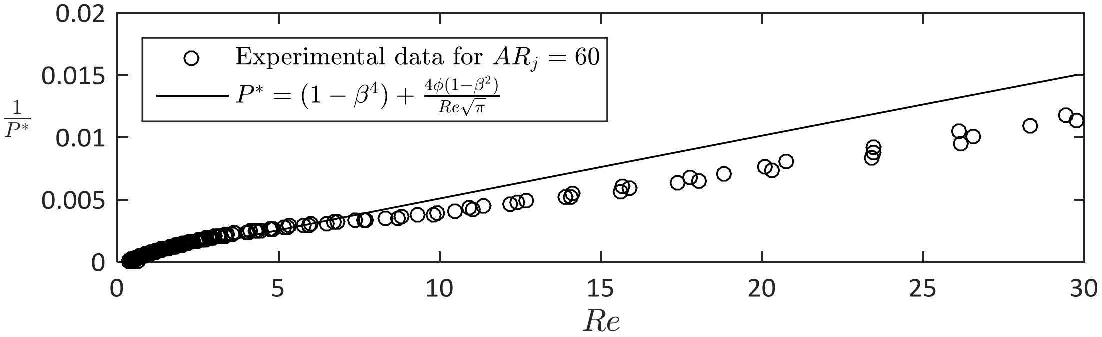
0.02
0.015
0.01
0.005
0
$\frac{1}{P^*}$
Experimental data for $AR_j = 60$
$P^* = (1-\beta^4) + \frac{4\phi(1-\beta^2)}{Re\sqrt{\pi}}$
0
5
10
15
20
25
30
Re

(e)

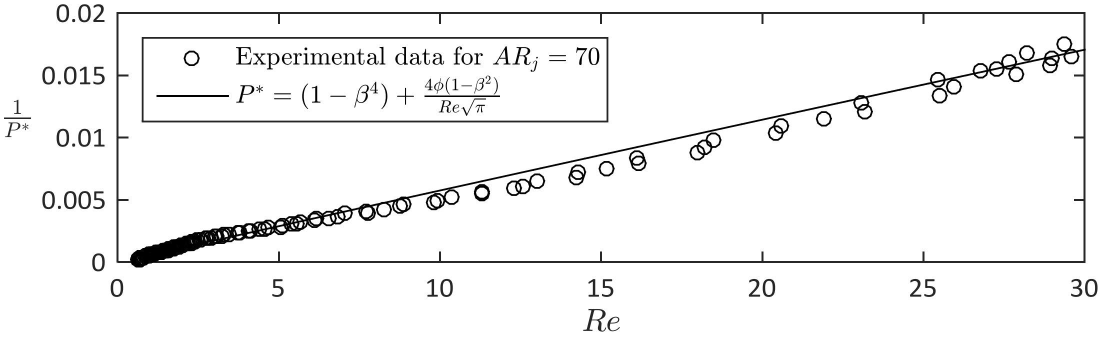
0.02
0.015
0.01
0.005
0
$\frac{1}{P^*}$
Experimental data for $AR_j = 70$
$P^* = (1-\beta^4) + \frac{4\phi(1-\beta^2)}{Re\sqrt{\pi}}$
0
5
10
15
20
25
30
Re

(f)

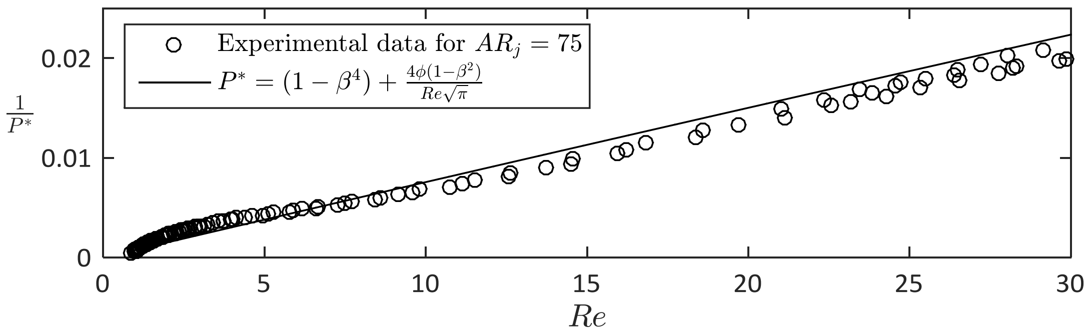
0.02
0.01
0
$\frac{1}{P^*}$
Experimental data for $AR_j = 75$
$P^* = (1-\beta^4) + \frac{4\phi(1-\beta^2)}{Re\sqrt{\pi}}$
0
5
10
15
20
25
30
Re

(g)

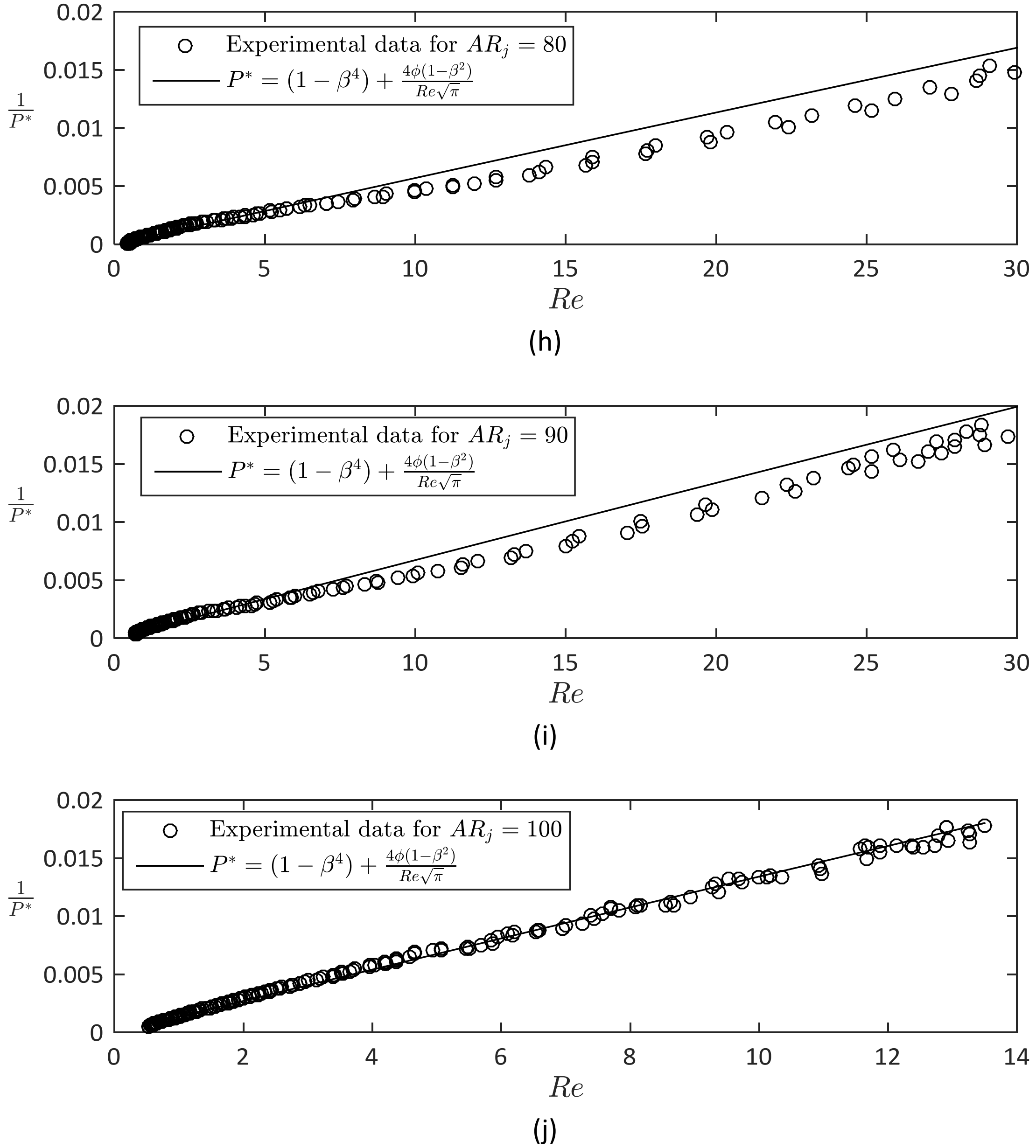

Figure 5.6 Comparison between the theoretical model and experimental data for rectangular slots (l = 9.525 mm) with (a) AR_j = 1, (b) AR_j = 10, (c) AR_j = 30, (d) AR_j = 45, (e) AR_j = 60, (f) AR_j = 70, (g) AR_j = 75, (h) AR_j = 80, (i) AR_j = 90, (j) AR_j = 100

Figure 5.6 shows the comparison between the theoretical model and the experimental data for rectangular slots with different aspect ratios (AR_j = 1 - 100). It represents that the theoretical model is in good agreement for low aspect ratio (AR_j = 1, 10, 30) slots. For high aspect ratio slots a deviation is observed in each experimental result mostly for high Reynolds number. This might be a representation that, the theoretical model might not be able to address the pressure loss characteristics for high aspect ratio slots, Because for developing the theoretical model (Section 0) aspect ratio factor was not considered and contraction was assumed as a circular shape.

Finlayson et al. [27] proposed that the pressure loss for a sudden contraction can be divided into two sections. These are a combination of momentum loss and viscous dissipation. According to [27] them pressure loss can be represented as:

$$\Delta P = \rho u^2(1-\beta^2) + k_l \frac{\mu u}{D_h} \tag{5.1}$$

where k_l is an empirical factor.

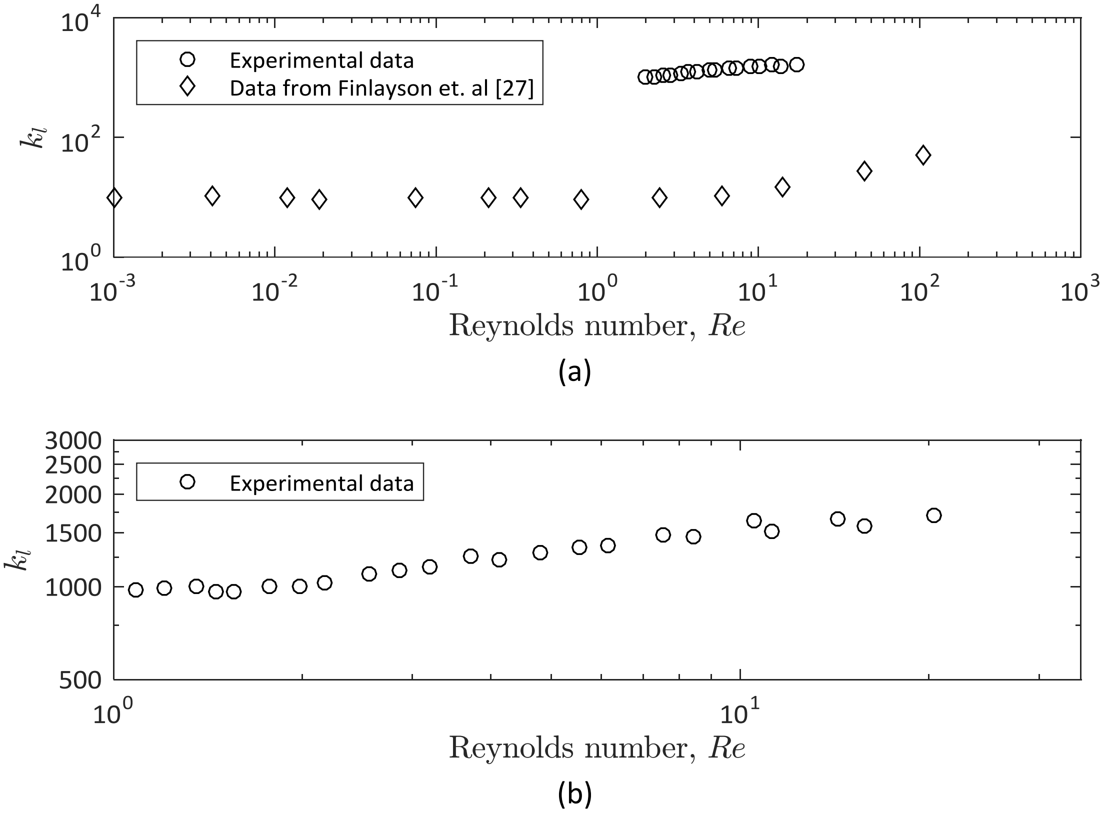

(a)

(b)

Figure 5.7 (a) Comparison between Finlayson et al. [27] data and the current experimental data, (b) expanded view of the experimental data

Figure 5.7(a) shows a comparison of the data from the empirical model developed by Finlayson et al [27] and the current experimental work. From Figure 5.7 (b) where k_l is calculated form current experimental results, it shows an increase in k_l factor at same Reynolds number range ($Re > 10$). A significant difference is observed in the scale of k_l factor between the cases. It is due to the factor that Finlayson et al. [27] worked with a high diameter ratio (β = 0.33) and they proposed that [27] with decreasing diameter ratio (β) k_l factor would increase. And calculated k_l factor from experimental data is very high because for this work, diameter ratio (β = 0.015) was very low.

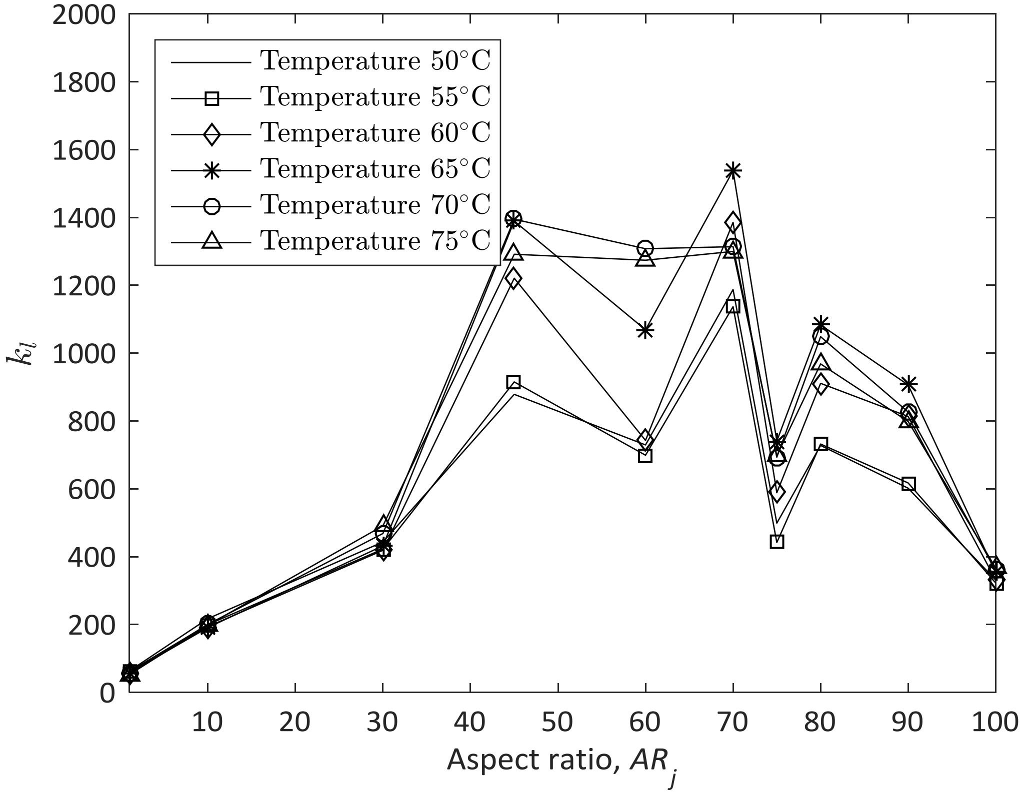

Figure 5.8 k_l factor variation with aspect ratio (AR_j) for slot l = 9.525 mm

Figure 5.8 shows the change in k_l with increasing aspect ratio (AR_j). It shows that k_l has a stronger dependence on aspect ratio rather than temperature. For low aspect ratio there is less shear deformation in the contraction region. That is why for low aspect ratio k_l factor is same for all the temperatures. Considerable increase in k_l factor is observed when aspect ratio changes from low to high.

5.2 Result for slot thickness l = 6.35 mm

In this section experimental result for coupon thickness l= 6.35 mm will be discussed. For this coupon aspect ratio (AR_j) was also varied from 1 - 100 with 10 different slots to see its effect on pressure loss. k_l factor will also be analyzed here for these slots.

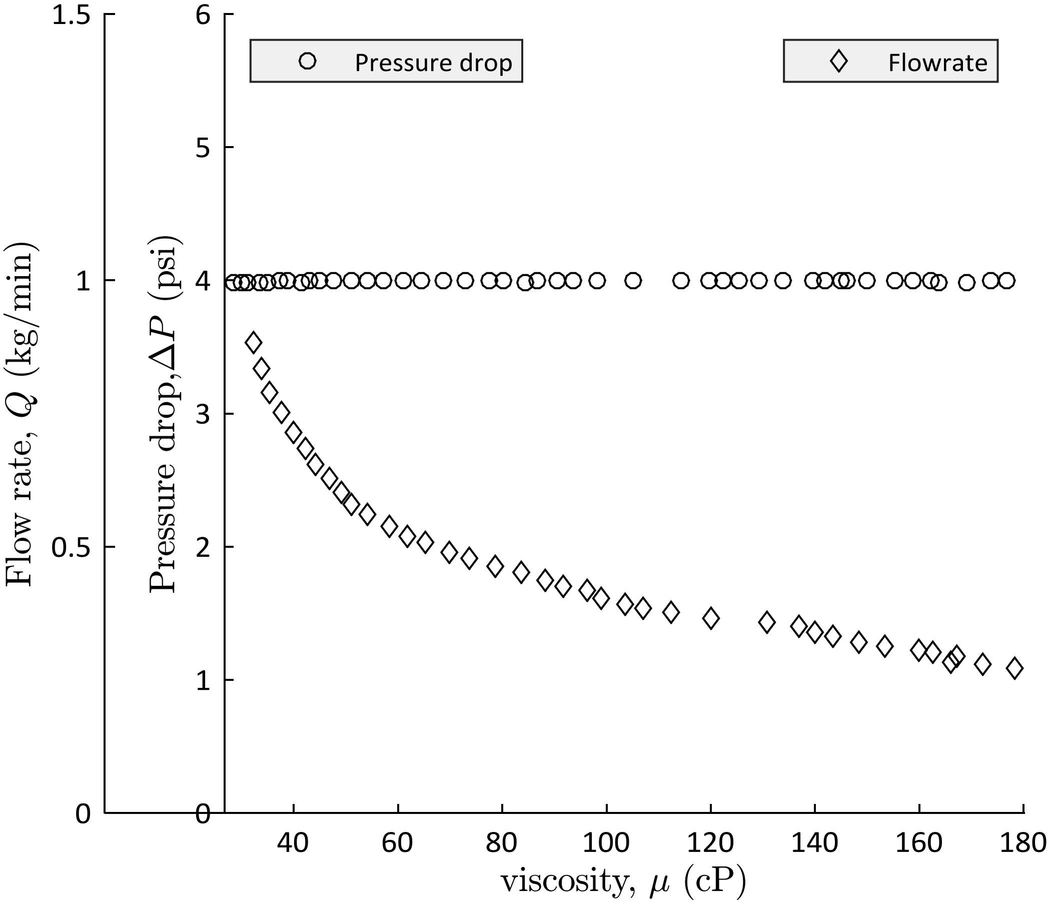

Figure 5.9 Experimentally measured data for a rectangular slot (a = 50 mm, b = 0.50 mm) with slot thickness l = 6.35 mm

Following the same experimental procedure a set of experiments were conducted with varying aspect ratio (AR_j = 1 - 100) for slot thickness l = 6.35 mm. Figure 5.9 shows an example experimental data set for a single experiment of that set with rectangular slot (a = 50 mm,

b = 0.5 mm). Experimental data for other cases are shown in Appendix C.3 From these experimental data non-dimensional pressure loss (P^*) was calculated using equation 1.5.

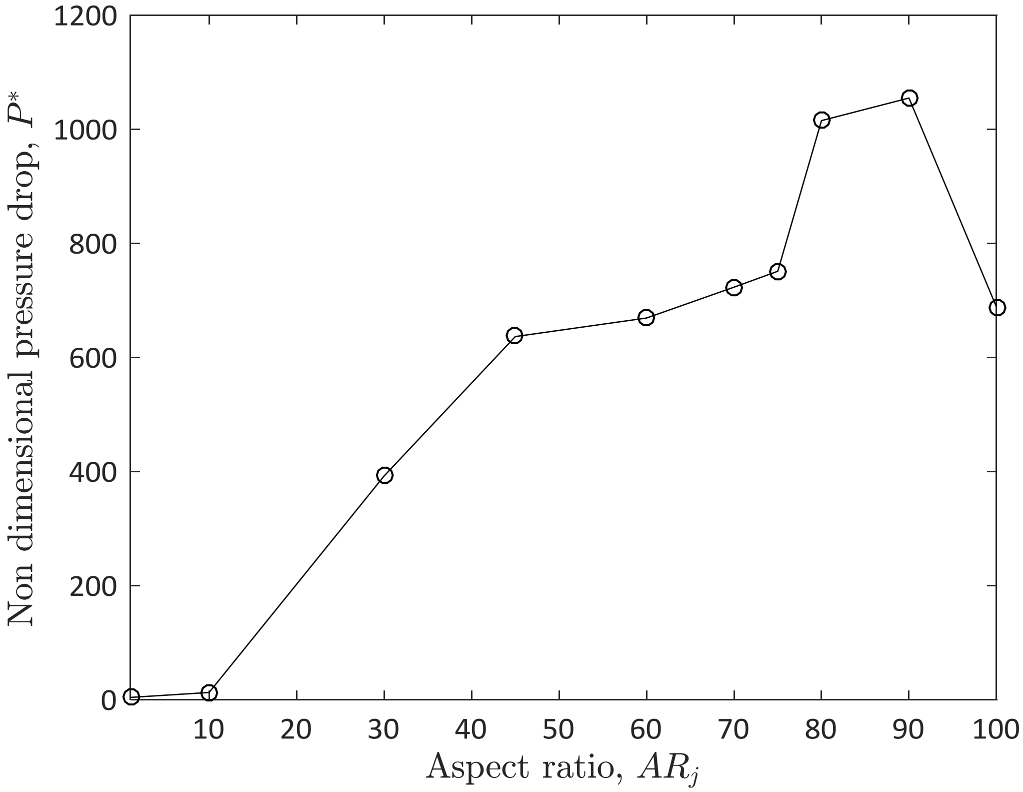

Figure 5.10 Non-dimensional pressure loss for l = 6.35 mm at T = 60 °C

Figure 5.10 shows the non-dimensional pressure loss variation with aspect ratio (AR_j). This result is for slot width l = 6.35 mm at T = 60 °C. At constant temperature the viscosity of the fluid is same, so the effect of pressure loss is only due to change in aspect ratio (AR_j). When the slot is square, flow through the slot is similar to flow through circular slot. As observed in previous chapter (Section 4.4) pressure loss is low for circular slot than rectangular slot. This is why for low aspect ratio (AR_j) pressure loss is low. With increasing aspect ratio (AR_j) pressure loss increases because of decreased diameter ratio (β). Some deviation from a normal increasing trend is observed for high aspect ratio (AR_j = 80, 90, 100) which might be due to potential instabilities of flow through slot. Although past researchers [32] have not observed any instability for the laminar flow, but their work was with very low aspect ratio (AR_j = 1, 1.5, 2, 3) compared to this work.

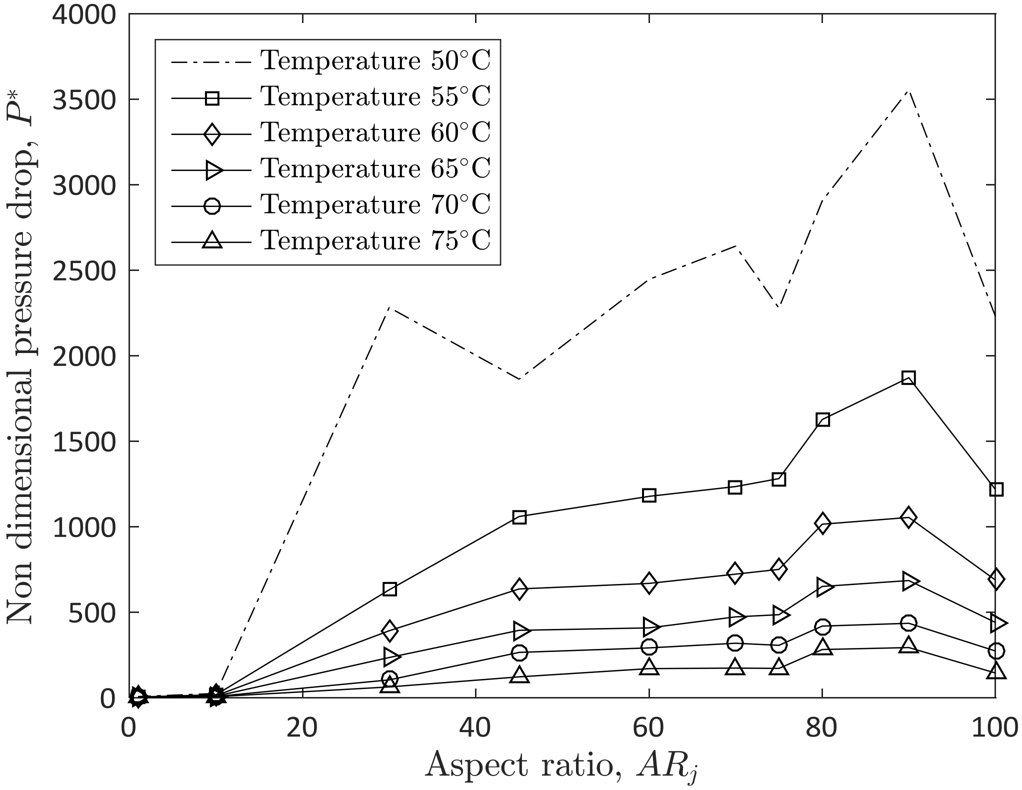

Figure 5.11 Non-dimensional pressure loss for l = 6.35 mm at different temperature

Figure 5.11 shows the variation of non-dimensional pressure loss with aspect ratio (AR_j) for different temperature. At different temperature pressure loss trend is same with aspect ratio (AR_j). Here temperature is a representation of fluid property (viscosity). At low aspect ratio the slot is not very narrow (contraction is not very abrupt) and shear deformation does not produce a major effect. This is why at low aspect ratio no variation is visible with respect to temperature. With increasing aspect ratio it shows that P^* is higher at low temperature, because at low temperature viscosity is significantly high. At higher temperatures the viscosity effect is not prominent. This is why a small increase is observed in P^* from low to high aspect ratio. The only factor contributed to this increase is the increase of aspect ratio.

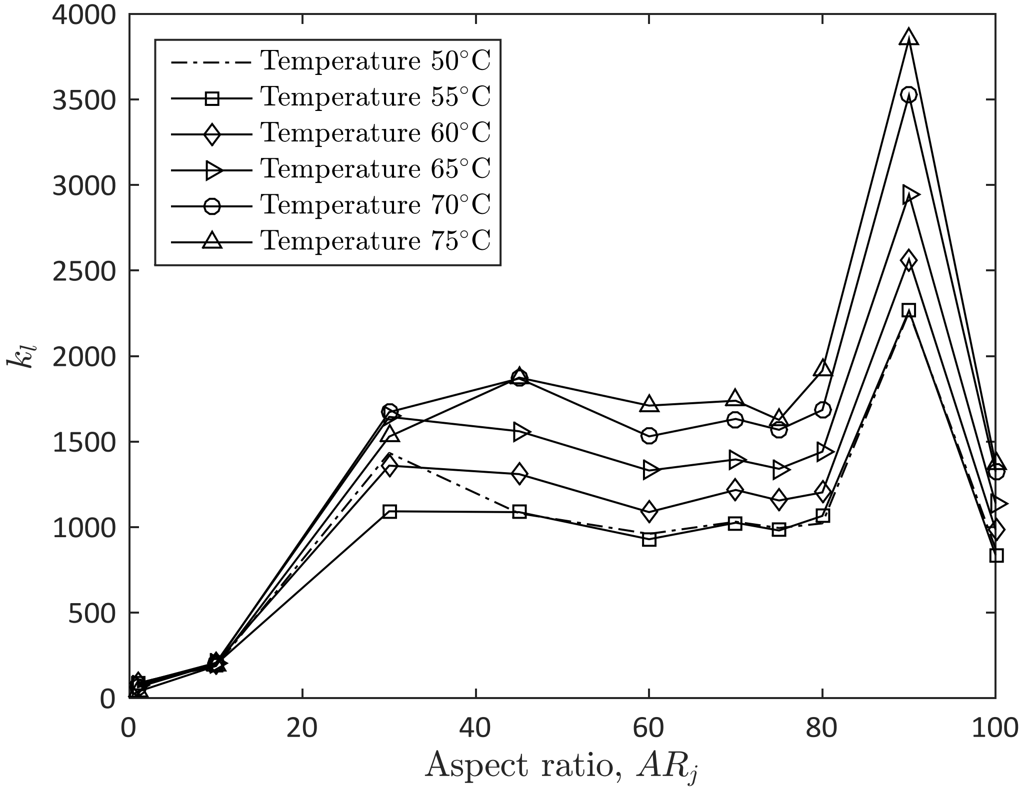

Figure 5.12 k_l factor variation with aspect ratio (AR_j) for coupon l = 6.35 mm

Figure 5.12 shows the change in k_l with increasing aspect ratio (AR_j). A considerable increase in k_l factor is observed when aspect ratio changes from 10 to 30. For AR_j = 30, 45, 60, 70 and 80 the contraction does not increase significantly and highlighting that k_l factor shows a stable trend. A strong peak at $AR_j = 90$ is observed which could be attributed to jet flow related phenomenon discussed previously. The characteristic of k_l is same for all the temperature in the high region of aspect ratio.

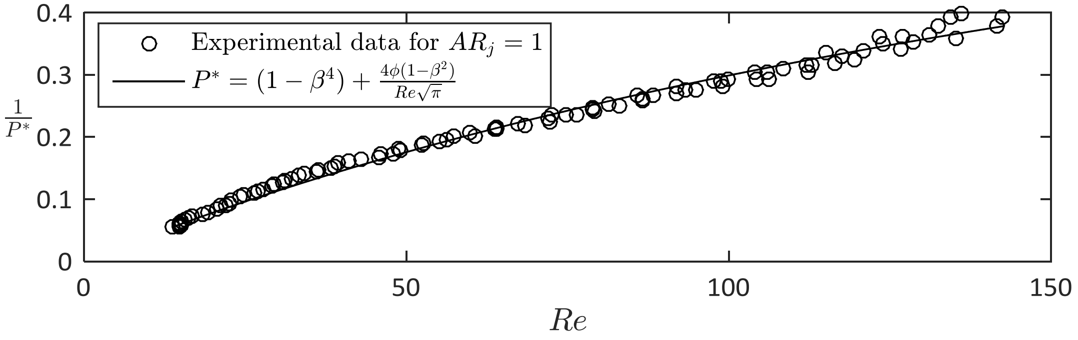
Experimental data for $AR_j = 1$
$P^* = (1-\beta^4) + \frac{4\phi(1-\beta^2)}{Re\sqrt{\pi}}$
$\frac{1}{P^*}$
0.4
0.3
0.2
0.1
0
0
50
100
150
Re

(a)

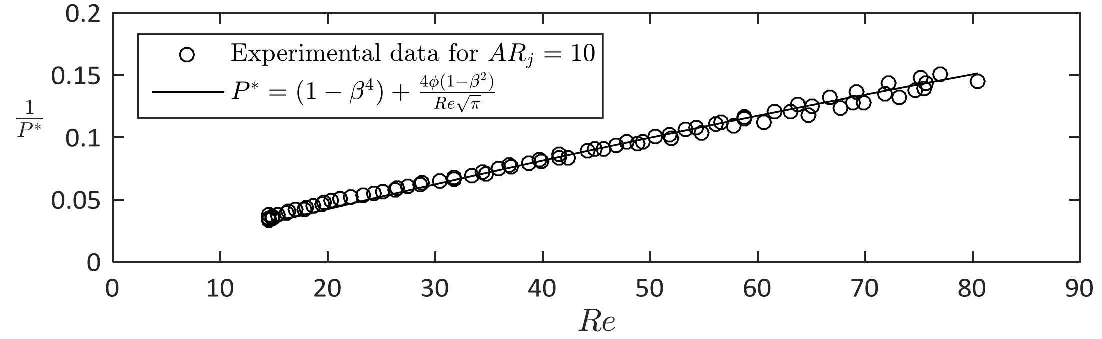
Experimental data for $AR_j = 10$
$P^* = (1-\beta^4) + \frac{4\phi(1-\beta^2)}{Re\sqrt{\pi}}$
$\frac{1}{P^*}$
0.2
0.15
0.1
0.05
0
0
10
20
30
40
50
60
70
80
90
Re

(b)

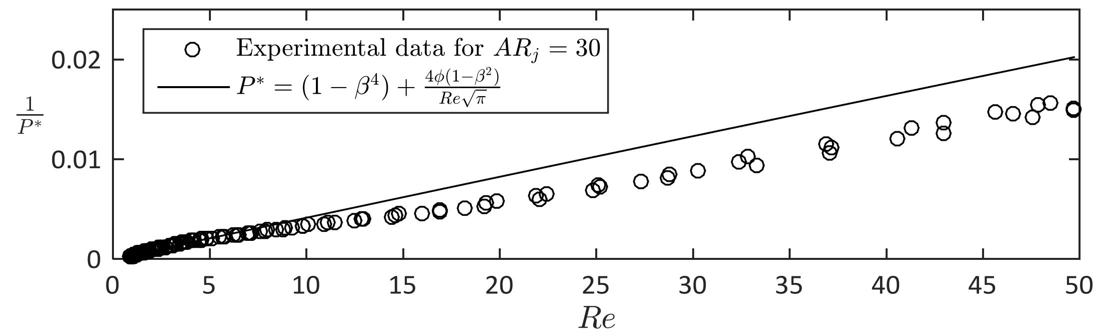
Experimental data for $AR_j = 30$
$P^* = (1-\beta^4) + \frac{4\phi(1-\beta^2)}{Re\sqrt{\pi}}$
$\frac{1}{P^*}$
0.02
0.01
0
0
5
10
15
20
25
30
35
40
45
50
Re

(c)

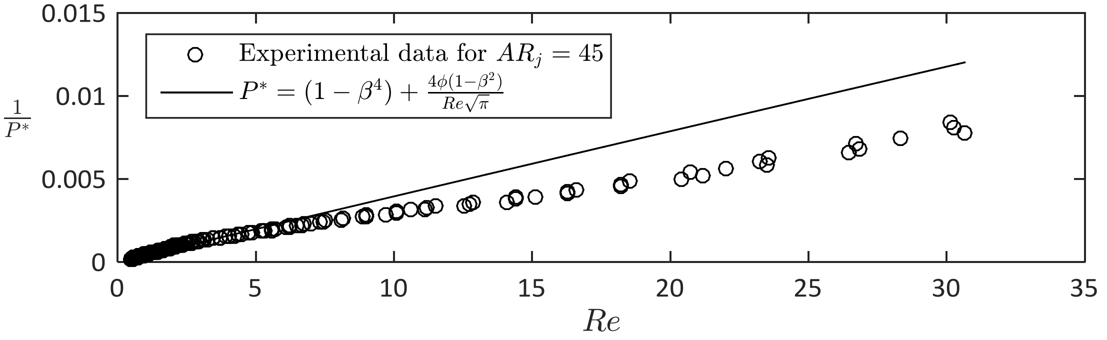
Experimental data for $AR_j = 45$
$P^* = (1-\beta^4) + \frac{4\phi(1-\beta^2)}{Re\sqrt{\pi}}$
$\frac{1}{P^*}$
0.015
0.01
0.005
0
0
5
10
15
20
25
30
35
Re

(d)

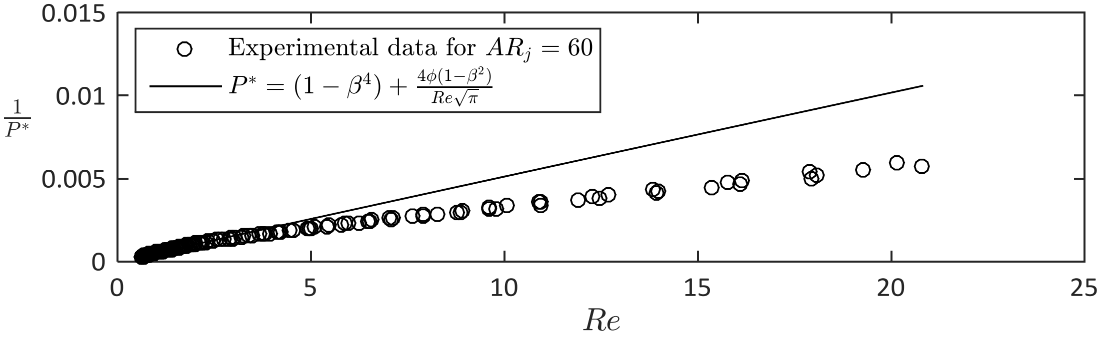

0.015
0.01
0.005
0
$\frac{1}{P^*}$
0
5
10
15
20
25
Re
Experimental data for $AR_j = 60$
$P^* = (1-\beta^4) + \frac{4\phi(1-\beta^2)}{Re\sqrt{\pi}}$

(e)

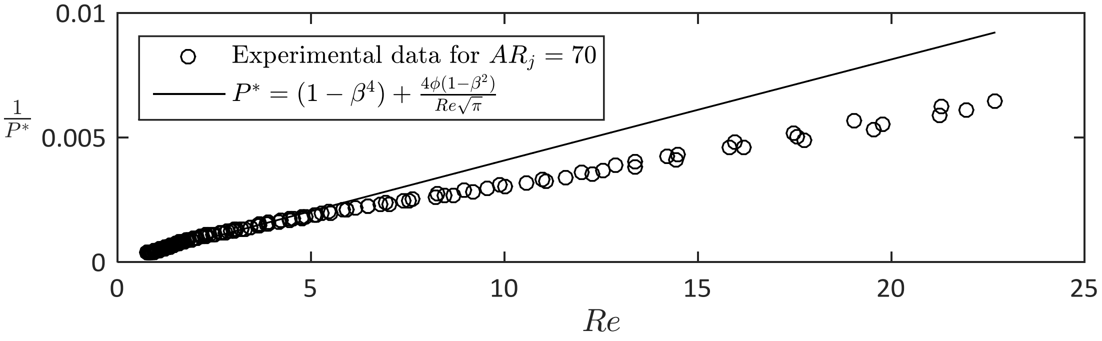

0.01
0.005
0
$\frac{1}{P^*}$
0
5
10
15
20
25
Re
Experimental data for $AR_j = 70$
$P^* = (1-\beta^4) + \frac{4\phi(1-\beta^2)}{Re\sqrt{\pi}}$

(f)

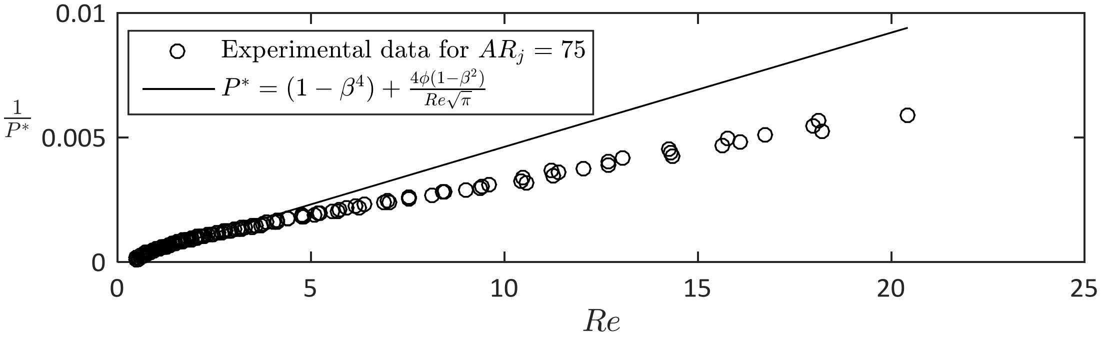

0.01
0.005
0
$\frac{1}{P^*}$
0
5
10
15
20
25
Re
Experimental data for $AR_j = 75$
$P^* = (1-\beta^4) + \frac{4\phi(1-\beta^2)}{Re\sqrt{\pi}}$

(g)

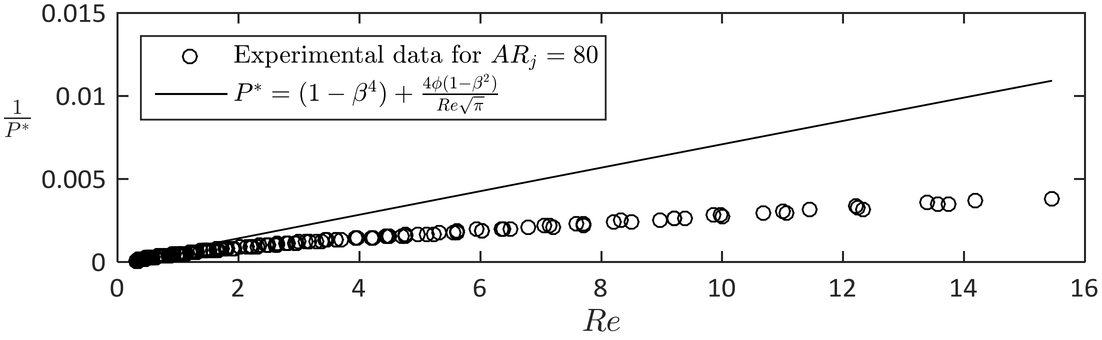

0.015
0.01
0.005
0
$\frac{1}{P^*}$
0
2
4
6
8
10
12
14
16
Re
Experimental data for $AR_j = 80$
$P^* = (1-\beta^4) + \frac{4\phi(1-\beta^2)}{Re\sqrt{\pi}}$

(h)

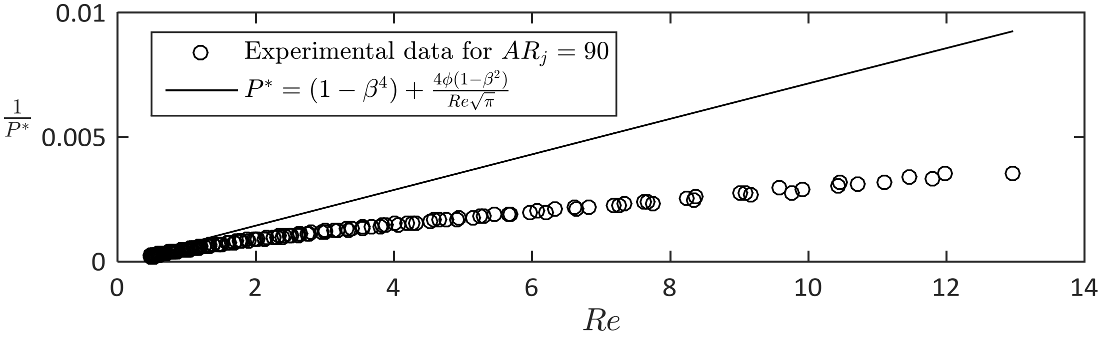

(i)

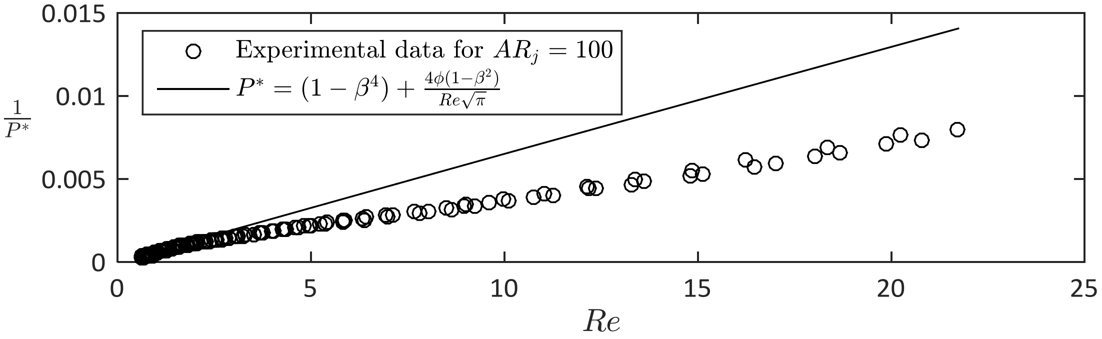

(j)

Figure 5.13 Comparison between the theoretical model and experimental data for rectangular slots (l = 6.35 mm) with (a) AR_j = 1, (b) AR_j = 10, (c) AR_j = 30, (d) AR_j = 45, (e) AR_j = 60, (f) AR_j = 70, (g) AR_j = 75, (h) AR_j = 80, (i) AR_j = 90, (j) AR_j = 100

Figure 5.13 shows the comparison of the theoretical model with the experimental data for different configurations of rectangular slots with slot thickness l = 6.35 mm. This figures again confirms that the theoretical model is in good agreement with the experimental data for low aspect ratio slots (AR_j = 1, 10). Potential jet characteristics (axis switching, instability) for high aspect ratios and assumption of circular slot for theoretical modelling might be the causes for deviation between theoretical model and experimental data for high aspect ratios.

5.3 Comparison between l = 6.35 mm and l = 9.525 mm thick slot

A comparison of non-dimensional pressure loss (P^*) between slot thickness l = 6.35 mm and l = 9.525 mm will give a better understanding about the effect of slot thickness. Slots having the same length (a) and width (b) but different thickness (l) are compared within their experimental range of Reynolds number. Same length (a) and width (b) will give the same hydraulic diameter (D_h) and diameter ratio (β) for a slot but by varying slot thickness (l) will change the thickness to diameter ratio $\left(TD = \frac{l}{D_h}\right)$.

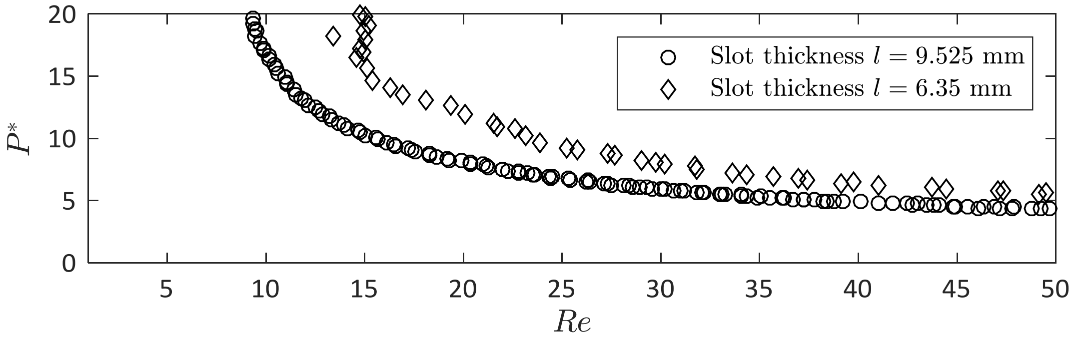

(a)

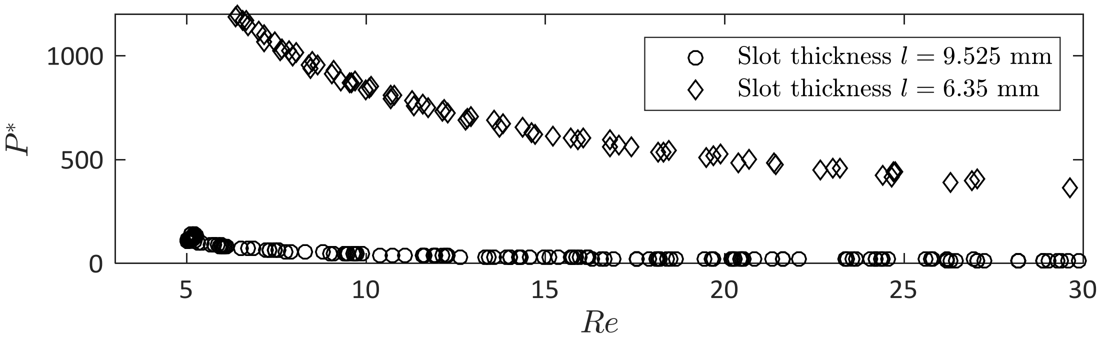

(b)

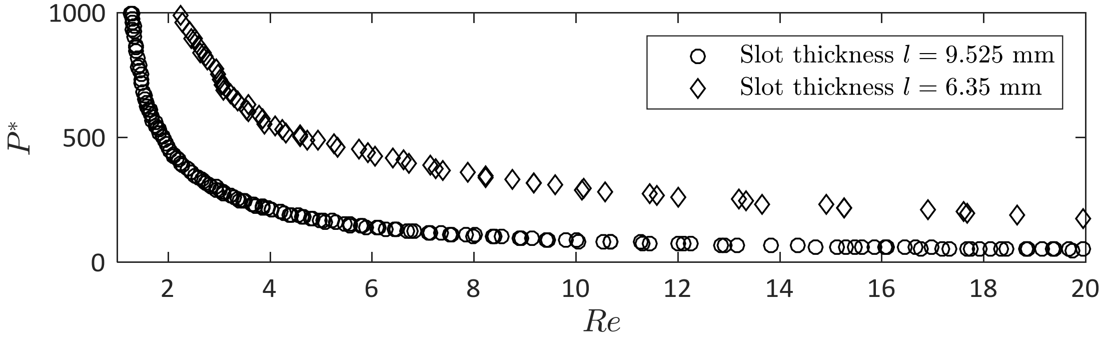

(c)

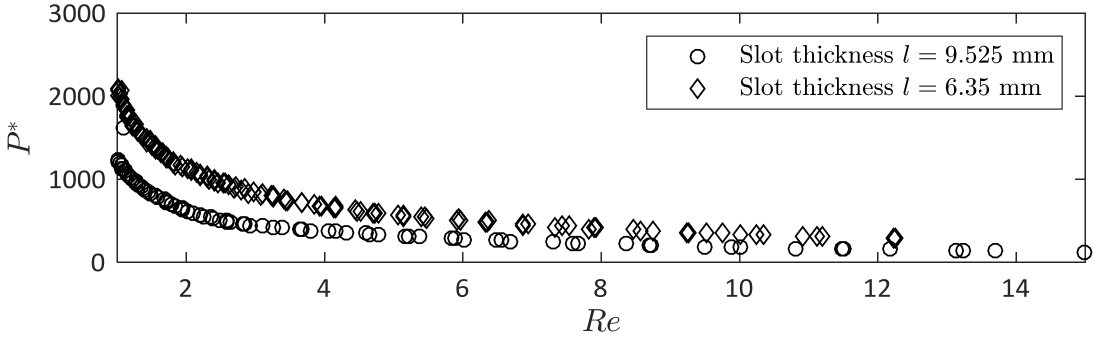

(d)

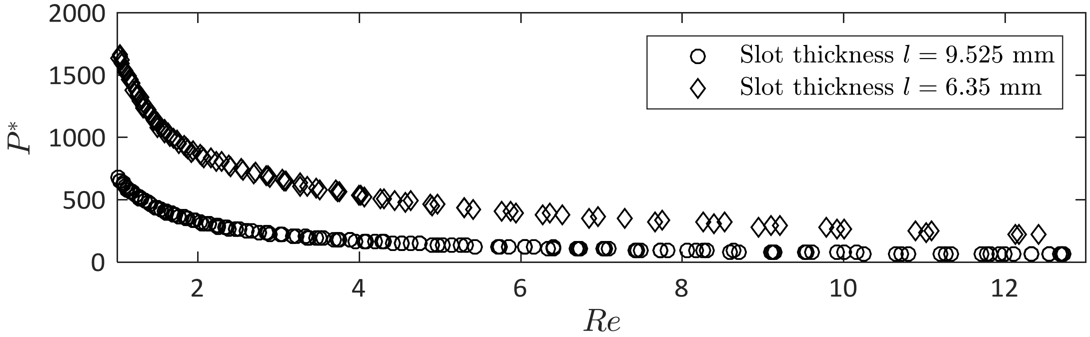

(e)

Figure 5.14 Comparison of non-dimensional pressure loss for different slot thicknesses with rectangular slots (a) a = 5 mm, b = 5 mm; (b) a = 16.3 mm, b = 1.54 mm; (c) a = 27.5 mm, b = 0.91 mm; (d) a = 47.5 mm, b = 0.53 mm; (a) a = 50 mm, b = 0.5 mm

Figure 5.14 shows the comparison of non-dimensional pressure loss for slot thickness l = 9.525 mm and l = 6.35 mm for five different cases. Figure 5.14 (a) shows the result of a square slot where both length (a) and width (b) was 5 mm. For this case of slots the thickness to diameter ratio $\left(TD = \frac{l}{D_h}\right)$ was reduced from 1.91 to 1.27 (Table 3.3 and Table 3.4) for thick

(l = 9.525 mm) to thin (l = 6.35 mm) slot while maintaining hydraulic diameter $\left(D_h = \frac{4ab}{2(a+b)}\right)$ for both slots. This reduction in the thickness to diameter ratio $\left(TD = \frac{l}{D_h}\right)$ is reflected in an increase in pressure loss by a factor of 1.3 - 1.4 over the range of Reynolds number ($15 < Re < 50$). Figure 5.14(e) represents the result of a slot which had the dimensions of a = 50 mm and b = 0.5 mm. The thickness to diameter ratio $\left(TD = \frac{l}{D_h}\right)$ was reduced from 9.62 to 6.41 (Table 3.3 and Table 3.4) for thick (l = 9.525 mm) to thin (l = 6.35 mm) slot. For this case there also an increase in P^* is observed by a factor of 2.45 - 3.65 for a range of Reynolds number ($1 < Re < 12$). Figure 5.14 (b), (c) and (d) with other configurations of rectangular slots also show the same trend for P^*. These results suggest that with decreasing thickness to diameter ratio $\left(TD = \frac{l}{D_h}\right)$, pressure loss increases for a lower range of Reynolds number ($1 \leq Re \leq 50$). The decrease in thickness to diameter ratio $\left(TD = \frac{l}{D_h}\right)$ represents a thinner slot with a wider slot width (increased D_h). From the previous analysis (Section 5.1 and Section 5.2) it is apparent that pressure loss is low for wider slots than narrower ones. This is the reason for increased P^* with decreasing thickness to diameter ratio $\left(TD = \frac{l}{D_h}\right)$. Previous researcher [8] also reported a similar trend with lower range of thickness to diameter ratio ($0.092 \leq \frac{l}{D_h} \leq 1.2$).

From this discussion it is evident that pressure loss is dependent on aspect ratio (AR_j) up to a limiting point. After that a deviation from normal trend is observed potentially due to other jet flow phenomena (axis switching of the flow, instability, or unequal convergence). The results show that the general trend is with increasing aspect ratio pressure loss would also increase. The main reason behind this is the increase in contraction with higher aspect ratio.

Another important geometric factor is the thickness to diameter ratio. The results show that while maintaining same cross sectional area and decrease in thickness to diameter ratio would increase the pressure loss.

Chapter 6: Conclusion and future recommendations

6.1 Conclusion

The research work conducted here was mainly focused on the pressure loss characteristic for highly viscous fluid across a narrow contraction. Part of this work was theoretical modelling but majority of the work was done by experiment. Theoretical modelling was done both for fully developed velocity profile of a non-Newtonian fluid and for non-dimensional pressure loss across a sudden contraction. Experimental results were also compared with the theoretical modelling for non-dimensional pressure loss to have a better understanding about the pressure loss characteristics in the lower region of Reynolds number across narrow slots.

The experimental work covered the diameter ratios $0.0105 \leq \beta \leq 0.0656$ along with three different slot shapes such as- streamlined, rectangular and circular. Experiments with streamlined slots covered the slot width range of 0.41 mm$\leq b \leq$ 0.58 mm. For the rectangular slot both aspect ratio $\left(AR_j\right)$ and thickness to diameter ratio (TD) were varied. The range of AR_j examined was $1 \leq AR_j \leq 100$ while that of TD was 1.27$\leq TD \leq$ 9.62. Viscosity of the test fluid was also varied within the range of 40 cP$\leq \mu \leq$ 300 cP to observe the effect of viscosity on pressure loss. The experiments were conducted with these parameters in the region of Reynolds number 50$\leq Re$ with some exceptions with circular slots when Reynolds number reached as high as Re = 250.

The theoretical modelling of a non-Newtonian fully developed velocity profile shows the characteristics of the non-Newtonian fluid. This model shows that the behaviour of a non-

Newtonian fluid is generally dominated by power law index (n). The theoretical modelling for non-dimensional pressure loss across sudden contraction gives an overview about the factors which dominate that parameter. From this modelling it is observed that pressure loss across sudden contraction is dependent on diameter ratio (β) for that geometry. Another observation made from this modelling is that for low Reynolds number (Re) pressure loss decreases with increasing Reynolds number. However, this result is only valid for low range of Reynolds number where viscous energy is comparable with the momentum energy. This result also shows that the viscosity has an effect on the pressure loss across the sudden contraction.

Experimental results from different shapes of slots show that the pressure loss is higher for the rectangular and the streamlined slot rather than the circular slot due to decreased diameter ratio (β). From the experiments with the streamlined slots, it is observed that with decreasing slot width non-dimensional pressure loss increases. Comparison of theoretical model with experimental data also shows that pressure loss characteristic follows the same trend for both cases with different slots.

Experimental results from the rectangular slots show that increasing aspect ratio (AR_j) increases non-dimensional pressure loss. While increasing aspect ratio (AR_j) for rectangular slot keeping the same cross sectional area, slot width decreases and that is the main factor for increasing non-dimensional pressure loss. Increasing thickness to diameter ratio (TD) shows that the pressure loss decreases for this scenario.

6.2 Future recommendations

Although this work varied all the dimensions of a slot to understand the effect of slot geometry and viscosity was also changed to see the effects of fluid's property, there are still some modifications needed to get the overall result about the characteristics of pressure loss across sudden contraction. These future recommendations are listed below.

- The theoretical modelling of non-dimensional pressure loss includes one empirical factor (ϕ). Although this model could predict the trend of pressure loss with change in Reynolds number, actual value was not possible to calculate because of that empirical factor (ϕ). This work shows that this empirical factor ϕ is in relation with diameter ratio (β). A direct relation between these two parameters would complete this theoretical modelling.
- This work incorporated diameter ratio (β) within the range of 0.0130 - 0.0656. Increasing the range of this diameter ratio (β) would make a strong support to the result presented in this work, because diameter ratio (β) is one of the major parameters to dominate the pressure loss across sudden contraction. Theoretical model could also be validated with this wide range of diameter ratio (β).
- Experiment with wider range of slot thickness (l) would also give a better understanding about its effect on pressure loss. The range needs to be widened in resemblance with practical applications point of view, so that if there is any deviation in the trend it could be observed.

- With respect to experimental procedure, the setup can be configured so that the flow rate can be controlled and the pressure loss can be measured. This configuration would give better control over the experiment and measurement of the data.
- A better temperature control of the test fluid over the whole test setup would give better understanding about the pressure loss characteristics. Viscous dissipation due to heat transfer across the slot was ignored for this work. This parameter can be included by having a better control over the temperature.

Though these modifications would give a better understanding about the pressure loss characteristics and fluid flow phenomena across the slot, the scope of this work did not suite all the changes.

References:

[1] R. M. Butler, G. S. Mcnab, and H. Y. Lo, “Theoretical studies on the gravity drainage of heavy oil during in-situ steam heating,” *The Canadian Journal of Chemical Engineering*, vol. 59, no. 4, pp. 455–460, Aug. 1981.

[2] Alberta Energy “Talk about SAGD,” factsheet, 2013. http://www.energy.alberta.ca/OilSands/pdfs/FS_SAGD.pdf

[3] H. Mochinaga, S. Onozuka, F. Kono, T. Ogawa, A. Takahashi, and T. Torigoe, “Properties of Oil sands and Bitumen in Athabasca,” *The Canadian Society of Exploration Geologists CSPG–CSEG–CWLS Convention*. pp. 39–44, 2006.

[4] O. Mohammadzadeh, N. Rezaei, and I. Chatzis, “Pore-level investigation of heavy oil and bitumen recovery using solvent aided steam assisted gravity drainage (SA-SAGD) process,” *Energy and Fuels*, vol. 24, no. 12, pp. 6327–6345, 2010.

[5] D. Matanovic, M. Cikes, and B. Moslavac, *Sand Control in Well Construction and Operation*. Berlin, Heidelberg: Springer Berlin Heidelberg, 2012.

[6] J. Carlson, D. Gurley, C. Price-smith, and F. Waters, “Sand Control : Why and How ?,” *Oilfield Review*, vol. 4, no. 4, pp. 41–53, 1992.

[7] J. Xie, S. W. Jones, C. M. Matthews, B. T. Wagg, P. Parker, and R. Ducharme, “Slotted liner design for SAGD wells,” *World Oil*, vol. 228, no. 6, pp. 67–75, 2007.

[8] T. Hasegawa, M. Suganuma, and H. Watanabe, “Anomaly of excess pressure drops of the

flow through very small orifices," *Physics of Fluids*, vol. 9, no. 1, p. 1, 1997.

[9] B. Sahin and H. Ceyhan, "Numerical and experimental analysis of laminar flow through square-edged orifice with variable thickness," *Transactions of the Institute of Measurement and Control*, vol. 18, no. 4, pp. 166–174, Jan. 1996.

[10] P. R. Bullen, D. J. Cheeseman, L. A. Hussain, and A. E. Ruffellt, "The determination of pipe contraction pressure loss coefficients for incompressible turbulent flow," *International Journal of Heat and Fluid Flow*, vol. 8, no. 2, pp. 111–118, Jun. 1987.

[11] F. M. White, *Fluid Mechanics*. McGraw-Hill, 2003.

[12] B. S. Massey and J. Ward-Smith, *Mechanics of Fluids*, 7th ed. CRC Press, 1998.

[13] C. F. Colebrook, "Turbulent flow in pipes, with particular reference to the transition region between the smooth and rough pipe laws," *Journal of the ICE*, vol. 11, no. 4, pp. 133–156, 1939.

[14] L. Choplin and P. J. Carreau, "Excess pressure losses in a slit," *Journal of Non-Newtonian Fluid Mechanics*, vol. 9, no. 1–2, pp. 119–146, 1981.

[15] F. C. Johansen, "Flow through Pipe Orifices at Low Reynolds Numbers," in *Proceedings of the Royal Society A: Mathematical, Physical and Engineering Sciences*, 1930, vol. 126, no. 801, pp. 231–245.

[16] L. K. Bhora, "Flow and pressure drop of highly viscous fluids in small aperture orifices," M.S. Thesis, Georgia Institute of Technology, 2004.

[17] S. Alvi, K. Sridharan, and N. Rao, “Loss characteristics of orifices and nozzles,” *Journal of Fluids Engineering*, vol. 100, no. 3, pp. 299–307, 1978.

[18] Z. Dagan, S. Weinbaum, and R. Pfeffer, “An infinite series solution for the creeping motion through an orifice of finite length,” *Journal of Fluid Mechanics*, vol. 115, no. FEB, pp. 505–523, 1982.

[19] R. A. Sampson, “On Stokes’s current function,” *Philosophical Transactions of the Royal Society A: Mathematical, Physical and Engineering Sciences*, vol. 182, pp. 449–518, Jan. 1891.

[20] R. D. Grose, “Orifice flow at low Reynolds Number,” *Journal of Pipeline*, vol. 3, pp. 207–214, 1983.

[21] Z. Zhang and J. Cai, “Compromise Orifice Geometry to Minimize Pressure Drop,” *Journal of Hydraulic Engineering*, vol. 125, no. 11, pp. 1150–1153, Nov. 1999.

[22] G. K. Morris and S. V. Garimella, “Orifice and impingement flow fields in confined jet impingement,” *Journal of Electronic Packaging*, vol. 120, no. 1, pp. 68–72, Mar. 1998.

[23] A. Ward-Smith, “A Unified Treatment of the Flow and Pressure Drop Characteristics of Constrictions Having Orifices With Square Edges,” in *Pressure Losses in Ducted Flows*, Butterworth, 1971.

[24] G. Gan and S. B. Riffat, “Pressure loss characteristics of orifice and perforated plates,” *Experimental Thermal and Fluid Science*, vol. 14, no. 2, pp. 160–165, Feb. 1997.

[25] D. S. Miller, *Internal Flow Systems*. BHRA, 1990.

[26] G. Astarita and G. Greco, "Excess pressure drop in laminar flow through sudden contraction. Newtonian Liquids," *Industrial & Engineering Chemistry Fundamentals*, vol. 7, no. 1, pp. 27–31, Feb. 1968.

[27] B. Finlayson and P. Drapala, "Micro-component flow characterization," in *Micro Instrumentation: For High Throughput Experimentation and Process Intensification - a Tool for PAT*, M. V. Koch, K. M. VandenBussche, and R. W. Chrisman, Eds. John Wiley & Sons, 2007.

[28] R. Jain, T. A. Long, J. Dickson, S. V. Brown, and E. Shtepani, "Experimental investigation of pressure drop/flowrate relationship for small aperture holes for high viscosity fluids," *SPE Production & Operations*, vol. 29, no. 02, pp. 114–121, May 2014.

[29] R. C. Deo, J. Mi, and G. J. Nathan, "The influence of nozzle aspect ratio on plane jets," *Experimental Thermal and Fluid Science*, vol. 31, no. 8, pp. 825–838, Aug. 2007.

[30] G. Marsters and J. Fotheringham, "The influence of aspect ratio on incompressible, turbulent flows from rectangular slots," *Aeronautical Quarterly*, vol. 31, no. Nov, pp. 285–305, 1980.

[31] W. R. Quinn, "Turbulent free jet flows issuing from sharp-edged rectangular slots: The influence of slot aspect ratio," *Experimental Thermal and Fluid Science*, vol. 5, no. 2, pp. 203–215, Mar. 1992.

[32] N. Chen and H. Yu, "Mechanism of axis switching in low aspect-ratio rectangular jets,"

Computers & Mathematics with Applications, vol. 67, no. 2, pp. 437–444, Feb. 2014.

[33] E. J. Gutmark and F. F. Grinstein, “Flow control with noncircular jets,” *Annual Review of Fluid Mechanics*, vol. 31, no. 1, pp. 239–272, Jan. 1999.

[34] H. Yu and S. S. Girimaji, “Lattice Boltzmann equation simulation of rectangular jet instability and axis-switching,” *Physica A: Statistical Mechanics and its Applications*, vol. 362, no. 1, pp. 151–157, Mar. 2006.

[35] H. Sato and F. Sakao, “An experimental investigation of the instability of a two-dimensional jet at low Reynolds numbers,” *Journal of Fluid Mechanics*, vol. 20, no. 02, p. 337, Mar. 2006.

[36] P. K. Kundu, I. M. Cohen, and D. R. Dowling, *Fluid Mechanics*, 5th ed. Elsevier, 2012.

[37] R. W. Johnson, *The Handbook of Fluid Dynamics*. Springer Science & Business Media, 1998.

[38] R. P. Chhabra and J. F. Richardson, *Non-Newtonian Flow and Applied Rheology*. Butterworth-Heinemann, 2008.

[39] J. Málek and K. R. Rajagopal, “Mathematical issues concerning the Navier-Stokes equations and some of its generalizations,” *Handbook of Differential Equations: Evolutionary Equations*, vol. 2, pp. 371–459, 2006.

[40] B. Taylor, *Guidelines for Evaluating and Expressing the Uncertainty of NIST Measurement Results (rev*. DIANE Publishing, 2009.

Appendix:

Appendix A

Calculation for uncertainty-

Uncertainty for slot inlet velocity. Slot inlet velocity was calculated as:

$$u = \frac{Q}{\rho A \times 60} = \frac{Q}{\rho ab \times 60} \qquad \text{A.1}$$

Differentiating velocity (u) with each term as:

$$\frac{\partial u}{\partial Q} = \frac{1}{60 \times \rho ab} \qquad \text{A.2}$$

$$\frac{\partial u}{\partial a} = \frac{-Q}{60 \times \rho a^2 b} \qquad \text{A.3}$$

$$\frac{\partial u}{\partial b} = \frac{-Q}{60 \times \rho ab^2} \qquad \text{A.4}$$

$$\frac{\partial u}{\partial \rho} = \frac{-Q}{60 \times \rho^2 ab} \qquad \text{A.5}$$

For a= 47.5 mm, b= 0.53 mm uncertainty is U_a=U_b=$\pm$0.0025 mm. For flow rate Q= 0.57192 kg/min uncertainty is U_Q= $\pm$10 % $\times Q$= $\pm 0.57 \times 10^{-3}$ kg/min = $\pm$9.5$\times 10^{-6}$ kg/s. For ρ= 852.48 kg/m^3 uncertainty is U_ρ= $\pm$0.5 kg/m^3. From equation A.2, A.3, A.4 and A.5 values are calculated as:

$$\frac{\partial u}{\partial Q} = \frac{1}{60 \times 852.48\ \mathrm{kg/m^3}\ \times 47.53 \times 10^{-3}\ \mathrm{m} \times 0.53 \times 10^{-3}\ \mathrm{m}}$$

$$= 0.776\ \mathrm{m/kg} \qquad \text{A.6}$$

$$\frac{\partial u}{\partial \rho} = \frac{-0.57192\ \mathrm{kg/s}}{60 \times (852.48\ \mathrm{kg/m^3})^2\ \times 47.53 \times 10^{-3}\ \mathrm{m} \times 0.53 \times 10^{-3}\ \mathrm{m}}$$

$$= -0.52 \times 10^{-3}\mathrm{m^4/kg.s} \qquad \text{A.7}$$

$$\frac{\partial u}{\partial a} = \frac{-0.57192\ \mathrm{kg/s}}{60 \times (47.53 \times 10^{-3}\ \mathrm{m})^2\ \times 852.48\ \mathrm{kg/m^3} \times 0.53 \times 10^{-3}\ \mathrm{m}}$$

$$= -9.35\ 1/\mathrm{s} \qquad \text{A.8}$$

$$\frac{\partial u}{\partial a} = \frac{-0.57192\ \mathrm{kg/s}}{60 \times (0.53 \times 10^{-3}\ \mathrm{m})^2\ \times 852.48\ \mathrm{kg/m^3} \times 47.53 \times 10^{-3}\ \mathrm{m}}$$

$$= -838.02\ \frac{1}{\mathrm{s}} \qquad \text{A.9}$$

Using consecutive error propagation approach [40] uncertainty for slot inlet velocity (U_u) is calculated as:

$$U_u = \sqrt{\left(\frac{\partial u}{\partial Q}U_Q\right)^2 + \left(\frac{\partial u}{\partial \rho}U_\rho\right)^2 + \left(\frac{\partial u}{\partial a}U_a\right)^2 + \left(\frac{\partial u}{\partial b}U_b\right)^2}$$

$$= \sqrt{\begin{array}{l}\left(0.776\ \mathrm{m/kg}\ \times (\pm 9.5 \times 10^{-6}\ \mathrm{kg/s})\right)^2 + \left(-0.52 \times 10^{-3}\mathrm{m^4/kg\text{-}s}\ \times (\pm 0.5\mathrm{kg/m^3})\right) \\ \quad + \left(-9.35\ \frac{1}{s} \times (\pm 0.0025 \times 10^{-3})\ \mathrm{m}\right)^2 + \left(-838.02\ \frac{1}{s}\ \times (\pm 0.0025 \times 10^{-3})\ \mathrm{m}\right)\end{array}}$$

$$= \pm 4.45\ \times 10^{-6}\ \mathrm{m/s} \qquad \text{A.10}$$

Uncertainty for Hydraulic diameter. Hydraulic diameter was calculated as:

$$D_h = \frac{4ab}{2(a+b)} = \frac{2ab}{(a+b)} \qquad \text{A.11}$$

For a = 47.5 mm, b = 0.53 mm uncertainty of D_h can be calculated by differentiating D_h with each term as:

$$\begin{aligned} \frac{\partial D_h}{\partial a} &= \frac{2b^2}{(a+b)^2} \\ &= \frac{2 \times (0.53 \times 10^{-3}\mathrm{m})^2}{(47.5 \times 10^{-3}\mathrm{m} + 0.53 \times 10^{-3}\mathrm{m})^2} \\ &= 0.243 \times 10^{-3} \end{aligned} \qquad \text{A.12}$$

and

$$\begin{aligned} \frac{\partial D_h}{\partial b} &= \frac{2a^2}{(a+b)^2} \\ &= \frac{2 \times (47.5 \times 10^{-3}\mathrm{m})^2}{(47.5 \times 10^{-3}\mathrm{m} + 0.53 \times 10^{-3}\mathrm{m})^2} \\ &= 1.956 \end{aligned} \qquad \text{A.13}$$

so uncertainty of hydraulic diameter can be calculated using consecutive error propagation approach [40] as:

$$\begin{aligned} U_{D_h} &= \sqrt{\left(\frac{\partial D_h}{\partial a} U_a\right)^2 + \left(\frac{\partial D_h}{\partial b} U_b\right)^2} \\ &= \sqrt{\begin{array}{c}\left(0.243 \times 10^{-3} \times (\pm 0.0025 \times 10^{-3}\ \mathrm{m})\right)^2 + \\ \left(1.956 \times (\pm 0.0025 \times 10^{-3}\ \mathrm{m})\right)^2\end{array}} \\ &= \pm 4.92 \times 10^{-6}\ \mathrm{m} \end{aligned} \qquad \text{A.14}$$

Uncertainty for Reynolds number. Reynolds number for this work was calculated as:

$$Re = \frac{\rho u D_h}{\mu} \qquad \text{A.15}$$

For variables u=0.44 m/s (equation A.1), D_h=0.001048 m (equation A.11) and for viscosity, μ= 30 cP= 0.03 Pa.s with uncertainty for viscosity U_μ=$\pm$0.3$\times$ 10^{-3} Pa.s uncertainty of Reynolds number (U_{Re}) was calculated. Differentiating with respect to density (μ) as:

$$\begin{aligned} \frac{\partial Re}{\partial \rho} &= \frac{u D_h}{\mu} \\ &= \frac{0.44\ \mathrm{m/s} \times 0.001048\ \mathrm{m}}{0.03\ \mathrm{Pa.s}} \\ &= 0.0154\ \mathrm{m^3/kg} \end{aligned} \qquad \text{A.16}$$

Differentiating with respect to velocity (u) as:

$$\begin{aligned}\frac{\partial Re}{\partial u} &= \frac{\rho D_h}{\mu} \\ &= \frac{852.4\ \mathrm{kg/m^3} \times 0.001048\ \mathrm{m}}{0.03\ \mathrm{Pa.s}} \\ &= 29.78\ \mathrm{s/m}\end{aligned} \tag{A.17}$$

Differentiating with respect to hydraulic diameter (D_h) as:

$$\begin{aligned}\frac{\partial Re}{\partial D_h} &= \frac{\rho u}{\mu} \\ &= \frac{852.4\ \mathrm{kg/m^3} \times 0.44\ \mathrm{m/s}}{0.03\ \mathrm{Pa.s}} \\ &= 12501.87\ \frac{1}{\mathrm{m}}\end{aligned} \tag{A.18}$$

and differentiating with respect to viscosity (μ) as:

$$\begin{aligned}\frac{\partial Re}{\partial \mu} &= \frac{-\rho u D_h}{\mu} \\ &= \frac{-852.4\ \mathrm{kg/m^3} \times 0.44\ \mathrm{m/s} \times 0.001048\ \mathrm{m}}{0.03\ \mathrm{Pa.s}} \\ &= -436.77\ \frac{1}{\mathrm{Pa.s}}\end{aligned} \tag{A.19}$$

Using equation A.16—A.19 uncertainty of Reynolds number (U_{Re}) is calculated as:

$$
\begin{aligned}
U_{Re} &= \sqrt{\left(\frac{\partial Re}{\partial \mu} U_{\mu}\right)^2 + \left(\frac{\partial Re}{\partial D_h} U_{D_h}\right)^2 + \left(\frac{\partial Re}{\partial \rho} U_{\rho}\right)^2 + \left(\frac{\partial Re}{\partial u} U_{u}\right)^2} \\
&= \sqrt{\begin{matrix} \left(-436.77\ \dfrac{1}{\mathrm{Pa.s}} \times (\pm 0.3 \times 10^{-3}\ \mathrm{Pa.s})\right)^2 + \\ \left(12501.87\ \dfrac{1}{\mathrm{m}} \times (\pm 4.92 \times 10^{-6}\ \mathrm{m})\right)^2 + \\ \left(0.0154\ \mathrm{m^3/kg} \times (\pm 0.5\mathrm{kg/m^3})\right)^2 + \\ \left(29.78\ \mathrm{s/m} \times (\pm 4.45\ \times 10^{-6}\ \mathrm{m/s})\right)^2 \end{matrix}} \\
&= \pm 0.145
\end{aligned}
\tag{A.20}
$$

For Reynolds number, $Re = 10.07$ (from equation A.15) uncertainty can be represented as:

$$
\begin{aligned}
U_{Re} &= \pm \frac{100 \times 0.145}{10.07} \\
&= \pm 1.44\ \%
\end{aligned}
\tag{A.21}
$$

Uncertainty for P^*. Non-dimensional pressure loss (P^*) was calculated as:

$$
P^* = \frac{\Delta P}{\frac{1}{2}\rho u^2}
\tag{A.22}
$$

For ΔP= 4 psi=27578 Pa , u=0.44 m/s and ρ= 852.48 kg/m^3 non-dimensional pressure loss was calculated as P^*=327.59.

For calculating uncertainty for non-dimensional pressure loss (U_{P^*}), differentiating equation A.22 with ΔP as:

$$\begin{aligned}\frac{\partial P^*}{\partial(\Delta P)} &= \frac{1}{\frac{1}{2}\rho u^2}\\ &= \frac{1}{0.5 \times 852.48\ \mathrm{kg/m^3} \times (0.44\ \mathrm{m/s})^2}\\ &= 0.0053\ \frac{1}{\mathrm{Pa}}\end{aligned} \quad \text{A.23}$$

Differentiating with respect to velocity (u) as:

$$\begin{aligned}\frac{\partial P^*}{\partial u} &= \frac{-2\Delta P}{\frac{1}{2}\rho u^3}\\ &= \frac{-2 \times 27578}{0.5 \times 852.48\ \mathrm{kg/m^3} \times (0.44\ \mathrm{m/s})^3}\\ &= -1519.07\ \mathrm{s/m}\end{aligned} \quad \text{A.24}$$

Differentiating with respect to density (ρ) as:

$$\begin{aligned}\frac{\partial P^*}{\partial \rho} &= \frac{-\Delta P}{\frac{1}{2}\rho^2 u^2}\\ &= \frac{-27578}{0.5 \times (852.48\ \mathrm{kg/m^3})^2 \times (0.44\ \mathrm{m/s})^2}\\ &= -0.392\ \mathrm{m^3/kg}\end{aligned} \quad \text{A.25}$$

So for $U_{\Delta P}$= $\pm$68.94 Pa, uncertainty of the non-dimensional pressure loss (U_{P^*}) is calculated as:

$$\begin{aligned} U_{P^*} &= \sqrt{\left(\frac{\partial P^*}{\partial(\Delta P)}U_{\Delta P}\right)^2 + \left(\frac{\partial P^*}{\partial \rho}U_{\rho}\right)^2 + \left(\frac{\partial P^*}{\partial u}U_{u}\right)^2} \\ &= \sqrt{\begin{array}{c}\left(0.0053\ \frac{1}{\mathrm{Pa}} \times (\pm 68.94\ \mathrm{Pa})\right)^2 + \left(-0.392\ \mathrm{m^3/kg} \times (\pm 0.5 \mathrm{kg/m^3})\right)^2 \\ + \left(-1519.07\ \mathrm{s/m} \times (\pm 4.45\ \times 10^{-6}\ \mathrm{m/s})\right)^2\end{array}} \\ &= 0.414 \end{aligned} \quad \text{A.26}$$

For P^*=327.59 this uncertainty can be represented as:

$$\begin{aligned} U_{P^*} &= \pm\frac{100 \times 0.414}{327.59} \\ &= \pm 0.126\ \% \end{aligned} \quad \text{A.27}$$

Appendix B

Table B.1 Raw sample data from experiment for rectangular slot (a = 50 mm, b = 0.5 mm)

Time (sec)	Reservoir Temperature (° C)	Pre-coupon Temperature (° C)	Post-coupon Temperature (° C)	Pre-coupon Pressure (psi)	Post-coupon Pressure (psi)	Top Block Temperature (° C)	Flow rate Q(Kg/min)	Density ρ (Kg/m^3)	Pressure difference ΔP (psi)	Viscosity μ (cP)
0	47.65	40.12	38.80	9.37449	0.49428	42.51	0.33623	871.19	8.8802	191.786
0.02	47.65	40.10	38.62	9.37116	0.49088	42.51	0.33608	871.19	8.88028	193.349
0.04	47.65	39.93	38.86	9.36855	0.48907	42.51	0.33617	871.29	8.87949	191.200
0.06	47.65	40.15	38.92	9.36672	0.4858	42.51	0.3362	871.4	8.88092	193.968
0.08	47.65	39.86	38.78	9.36318	0.48353	42.51	0.33681	871.26	8.87965	190.718
0.1	47.65	40.17	38.71	9.36394	0.48159	42.51	0.3361	871.22	8.88235	194.262
0.12	47.65	40.07	38.74	9.35669	0.47916	42.51	0.33664	871.37	8.87753	190.368
0.14	47.65	40.03	38.86	9.35721	0.47977	42.51	0.33641	871.22	8.87744	194.016
0.16	47.65	40.20	38.71	9.35241	0.47779	42.51	0.3366	871.23	8.87461	190.145
0.18	47.65	40.01	38.57	9.34953	0.47346	42.51	0.33674	871.13	8.87607	193.719
0.2	47.65	40.19	38.70	9.34914	0.47263	42.51	0.33675	871.29	8.87651	190.388
0.22	47.65	40.06	38.94	9.3464	0.46909	42.51	0.33688	871.28	8.87731	193.372
0.24	47.65	40.08	38.89	9.34502	0.46766	42.51	0.33624	871.23	8.87735	190.741
0.26	47.65	40.02	38.73	9.34131	0.46873	42.51	0.33605	871.21	8.87257	192.695
0.28	47.65	40.01	38.73	9.33637	0.46357	42.51	0.33651	871.41	8.8728	191.723
0.3	47.65	40.24	38.75	9.336	0.45946	42.51	0.33537	871.19	8.87654	192.081
0.32	47.65	40.01	38.74	9.3335	0.4593	42.51	0.33525	871.14	8.8742	192.861
0.34	47.65	39.93	38.69	9.33258	0.4588	42.51	0.33464	871.31	8.87378	191.443
0.36	47.65	40.20	38.76	9.3284	0.45664	42.51	0.33411	871.32	8.87176	193.773
0.38	47.65	40.02	38.77	9.3234	0.45488	42.51	0.33359	871.28	8.86851	190.829
0.4	47.65	40.12	38.71	9.32526	0.4494	42.51	0.33264	871.18	8.87586	194.264

Appendix C

Appendix C.1

Experimentally measured data for streamlined slot.

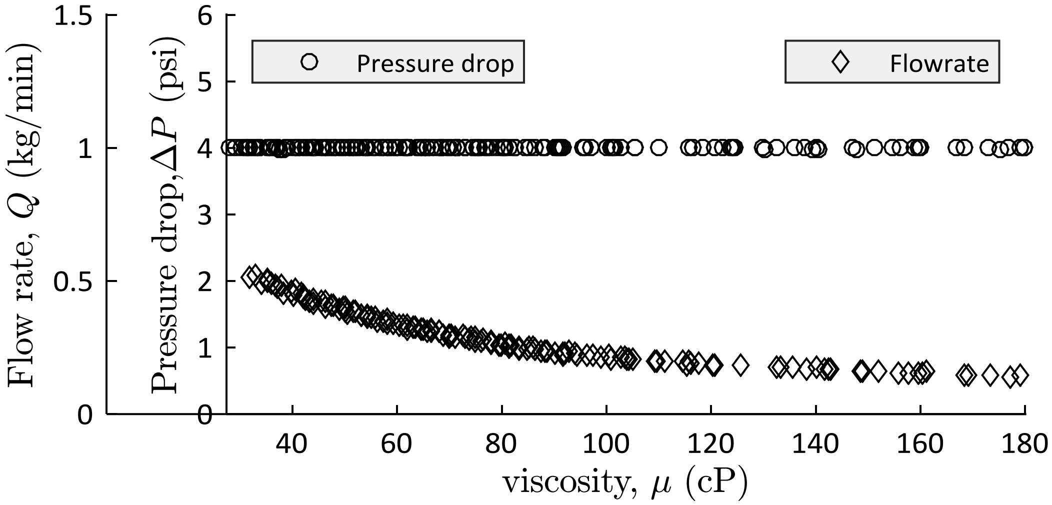

Figure C.1 Experimentally measured data for a streamlined slot (*a*=25.4 mm, *b*=0.41 mm)

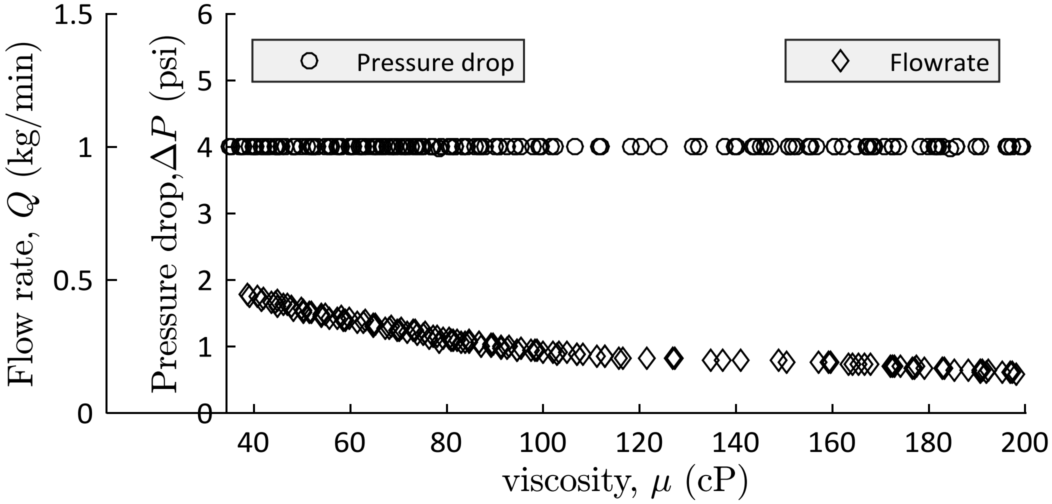

Figure C.2 Experimentally measured data for a streamlined slot (*a*=25.4 mm, *b*=0.43 mm)

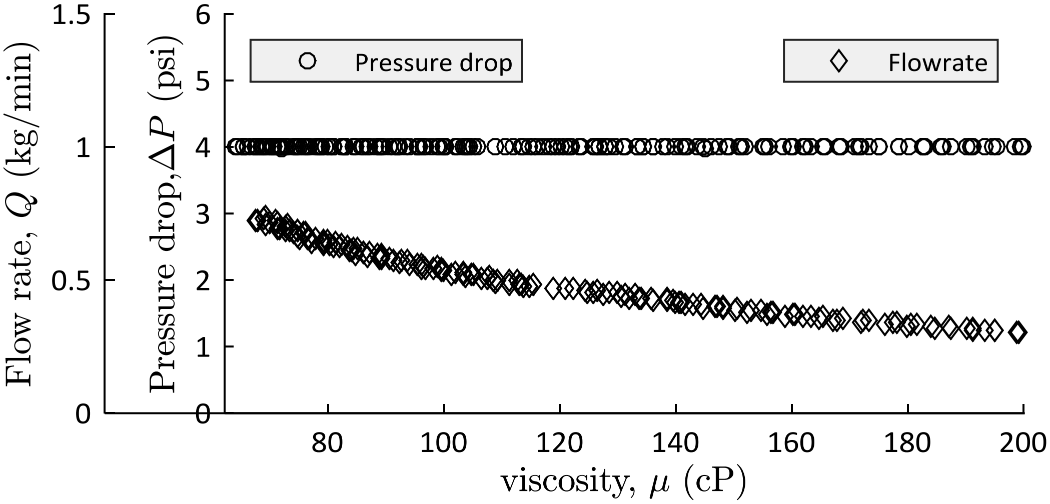

Figure C.3 Experimentally measured data for a streamlined slot (a=25.4 mm, b=0.53 mm)

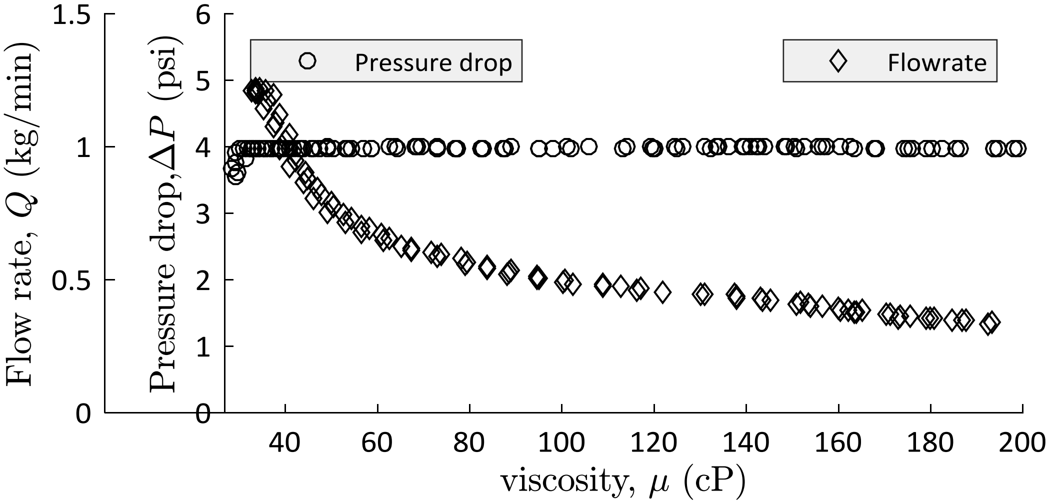

Figure C.4 Experimentally measured data for a streamlined slot (a=25.4 mm, b=0.58 mm)

Appendix C.2

Experimental data for different configurations of rectangular slot with slot thickness l=9.525 mm.

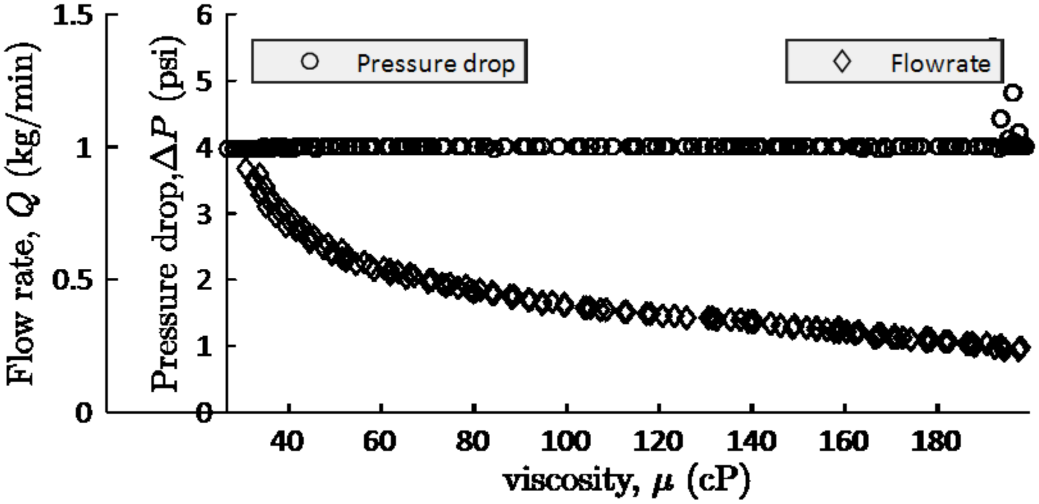

Figure C.5 Experimentally measured data for a rectangular slot (a=25.4 mm, b=0.58 mm, l=9.525 mm)

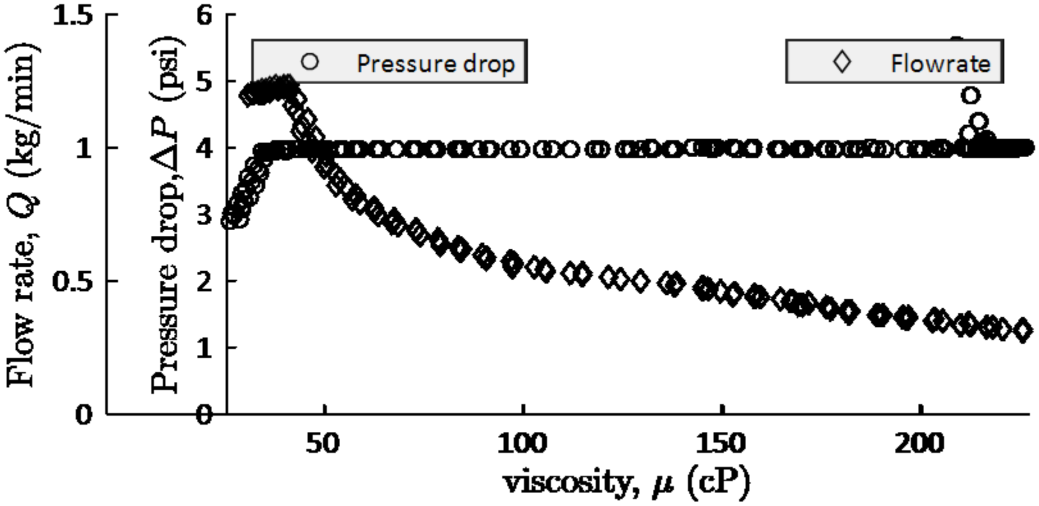

Figure C.6 Experimentally measured data for a rectangular slot (a=47.5 mm, b=0.53 mm, l=9.525 mm)

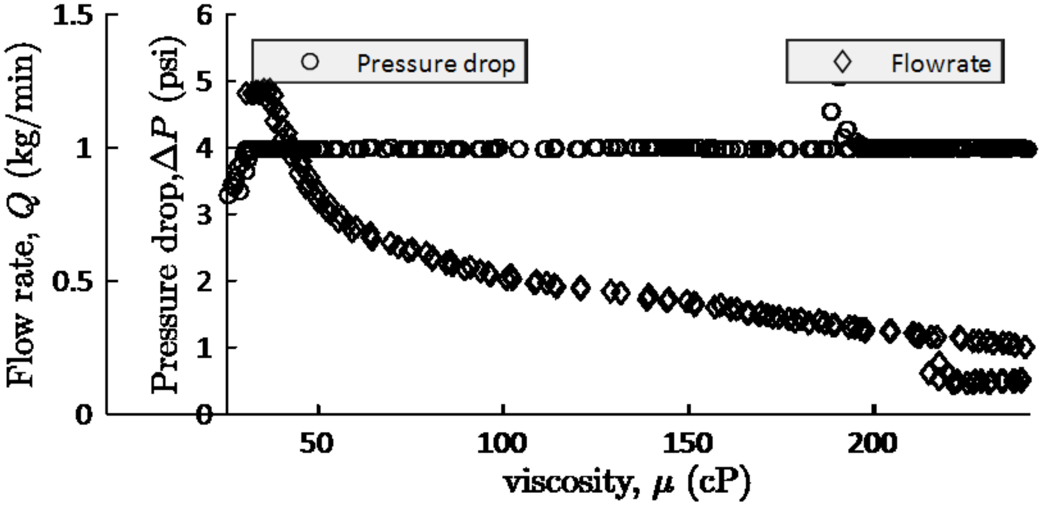

Figure C.7 Experimentally measured data for a rectangular slot (a=44.5 mm, b=0.56 mm, l=9.525 mm)

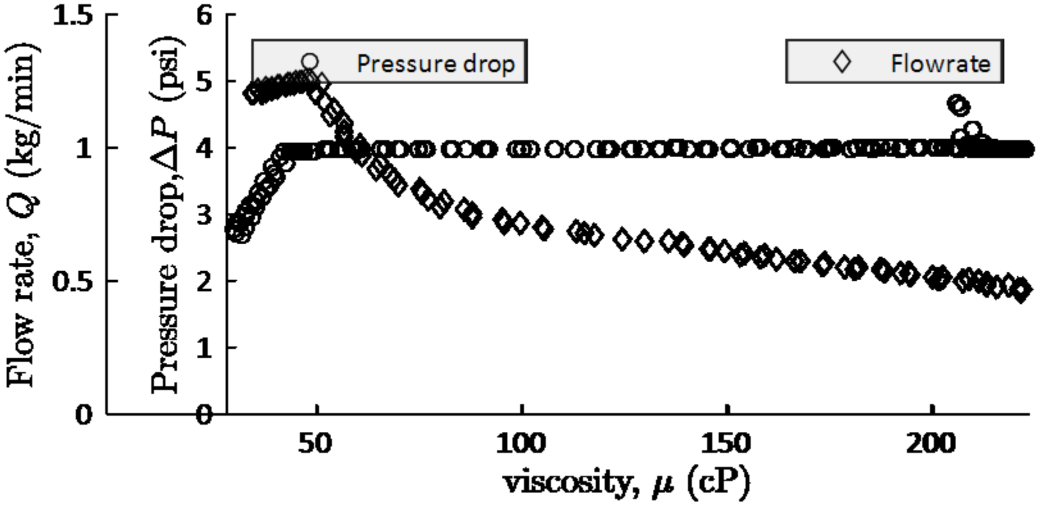

Figure C.8 Experimentally measured data for a rectangular slot (a=43.5 mm, b=0.57 mm, l=9.525 mm)

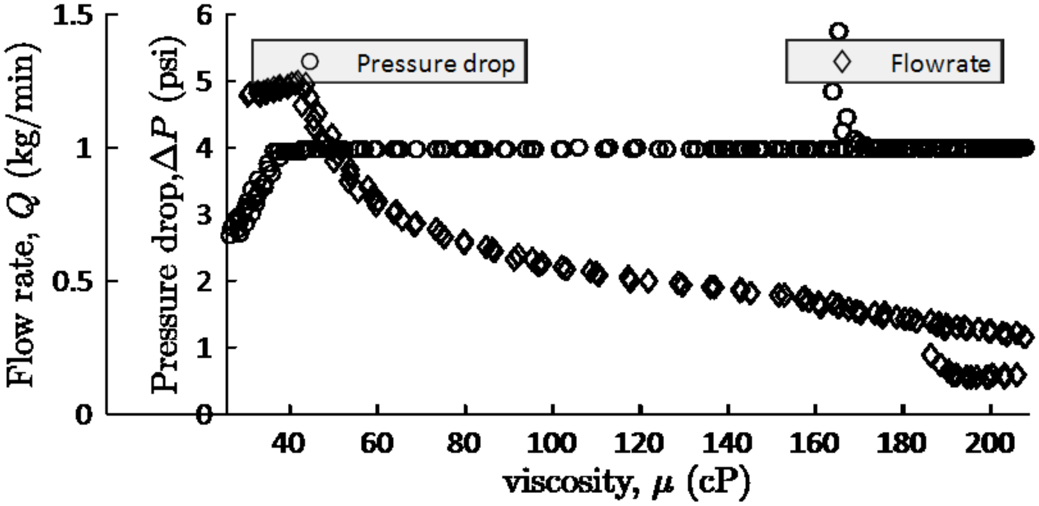

Figure C.9 Experimentally measured data for a rectangular slot (a=41.9 mm, b=0.60 mm, l=9.525 mm)

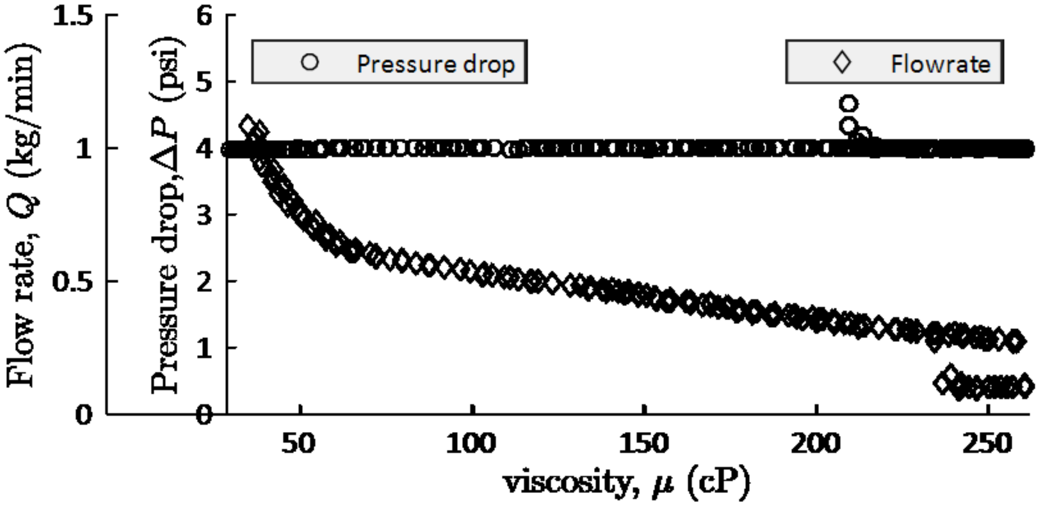

Figure C.10 Experimentally measured data for a rectangular slot (a=38.8 mm, b=0.64 mm, l=9.525 mm)

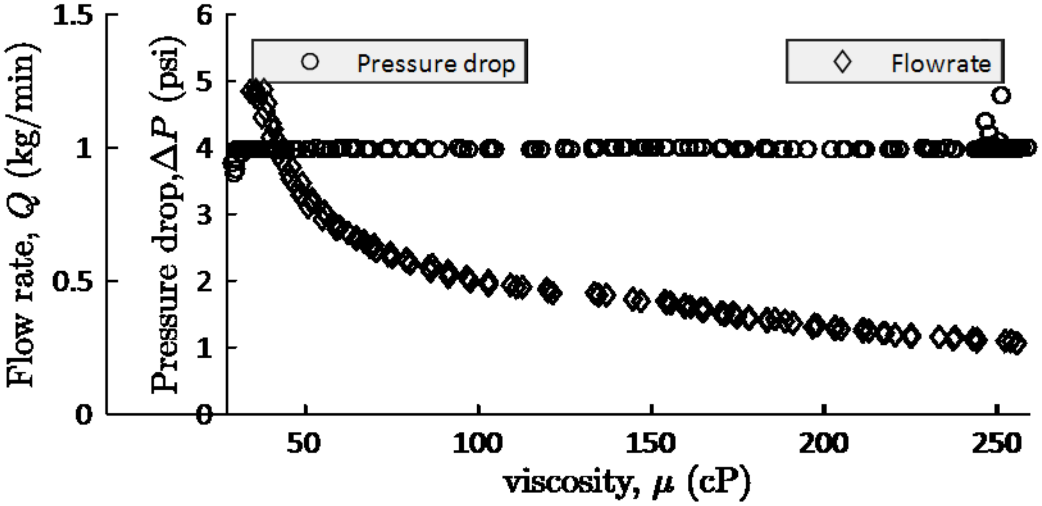

Figure C.11 Experimentally measured data for a rectangular slot (a=33.6 mm, b=0.74 mm, l=9.525 mm)

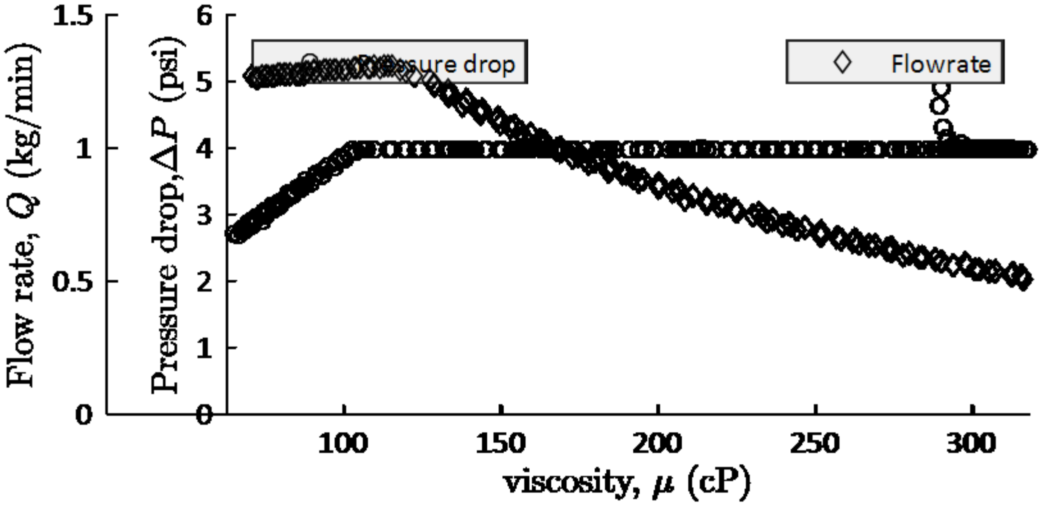

Figure C.12 Experimentally measured data for a rectangular slot (a=27.4 mm, b=0.91 mm, l=9.525 mm)

Appendix C.3

Experimental data for different configurations of rectangular slot with slot thickness l = 6.35 mm.

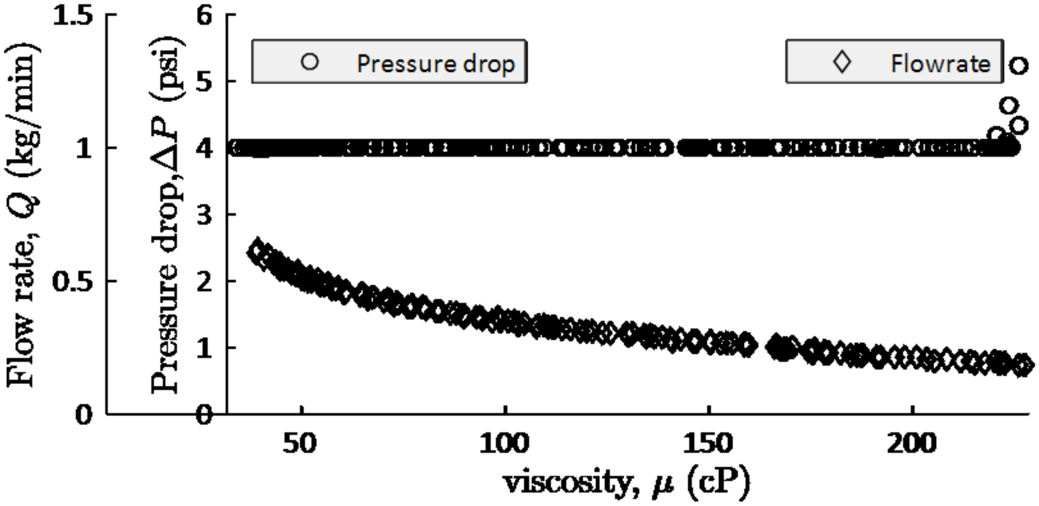

Figure C.13 Experimentally measured data for a rectangular slot (a=47.5 mm, b=0.53 mm, l=6.35 mm)

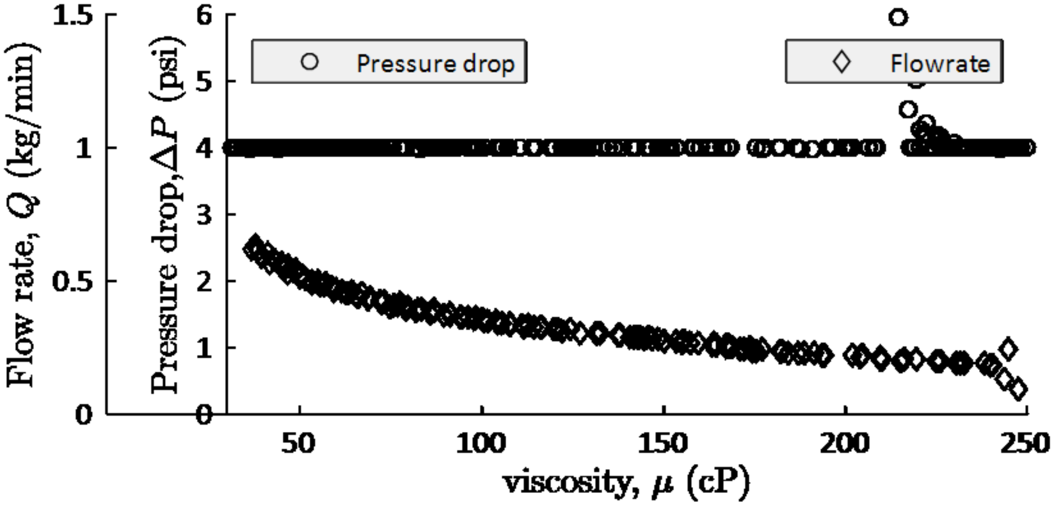

Figure C.14 Experimentally measured data for a rectangular slot (a=44.8 mm, b=0.56 mm, l=6.35 mm)

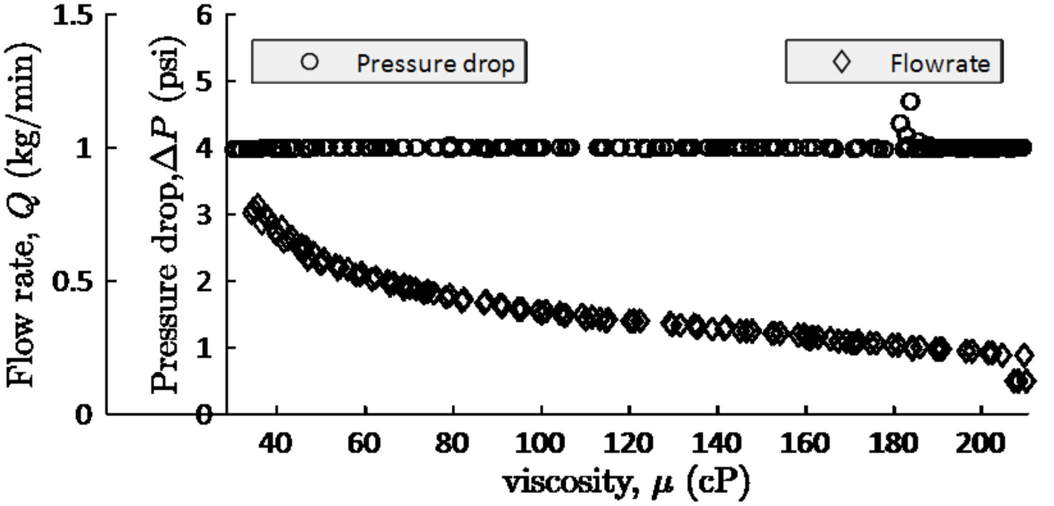

Figure C.15 Experimentally measured data for a rectangular slot (a=43.5 mm, b=0.57 mm, l=6.35 mm)

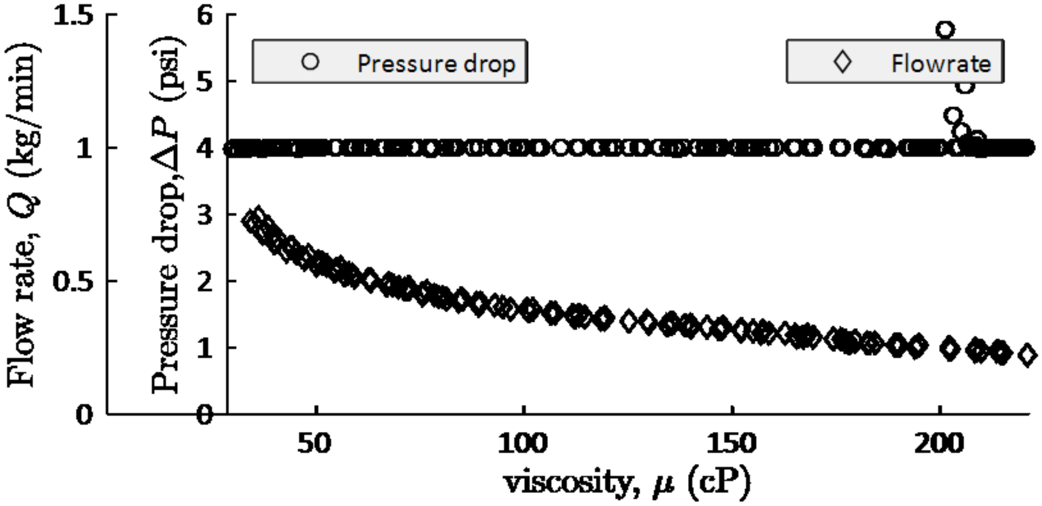

Figure C.16 Experimentally measured data for a rectangular slot (a=38.75 mm, b=0.6 mm, l=6.35 mm)

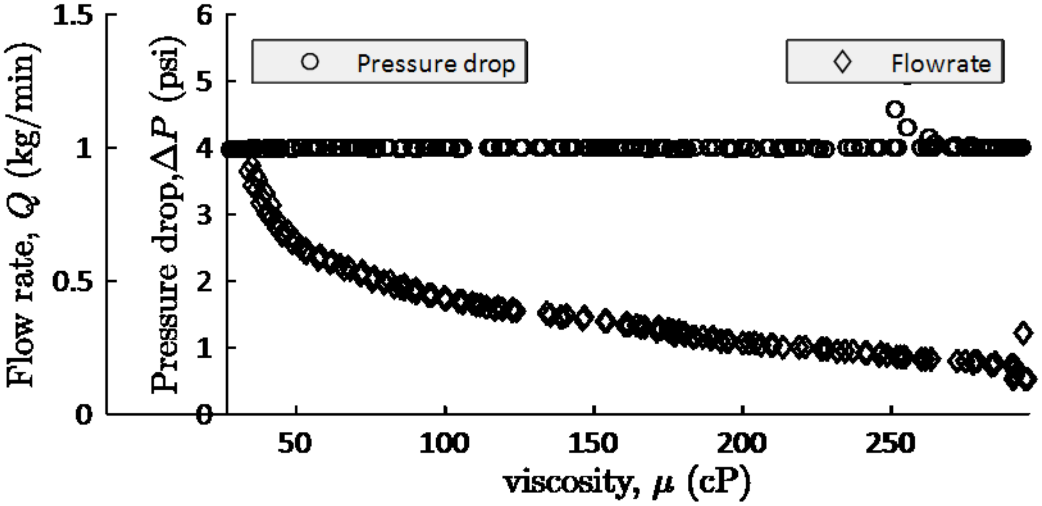

Figure C.17 Experimentally measured data for a rectangular slot (a=33.6 mm, b=0.74 mm, l=6.35 mm)

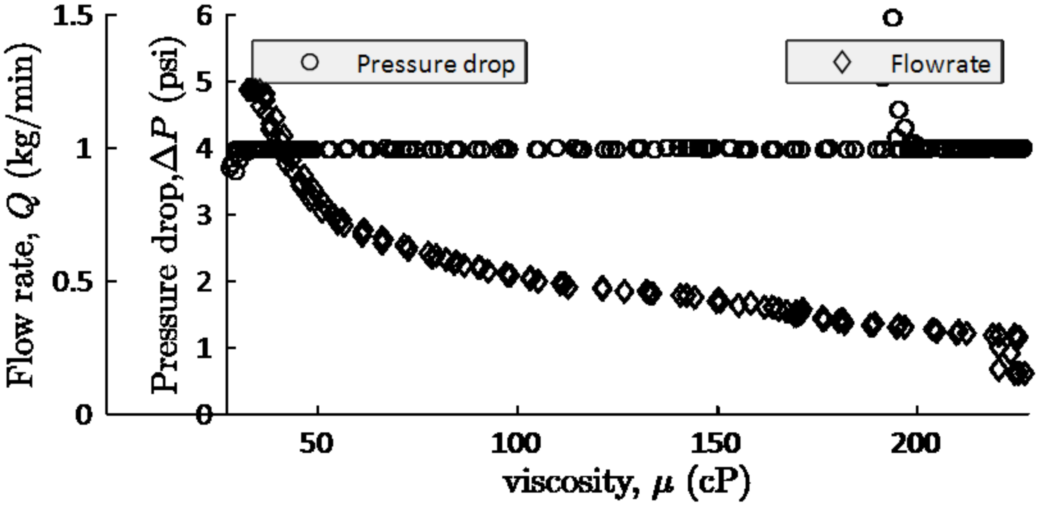

Figure C.18 Experimentally measured data for a rectangular slot (a=27.5 mm, b=0.9 mm, l=6.35 mm)